UNIVERSITAT POLITÈCNICA DE CATALUNYA BARCELONATECH

Power calculation algorithm under nonlinear loads and Hopf oscillator-based synchronization controller for grid-forming inverters in a microgrid

Mingshen Li

UNIVERSITAT POLITÈCNICA
DE CATALUNYA
BARCELONATECH

PhD program in ELECTRICAL ENGINEERING

Power Calculation Algorithm under Nonlinear Loads and Hopf Oscillator-based Synchronization Controller for Grid-forming Inverters in a Microgrid

Author
Mingshen Li

Supervisor
Dr. Prof. José Matas Alcalá
Co-supervisor
Dr. Prof. Josep M. Guerrero

ELECTRICAL ENGINEERING DEPARTMENT
ESCOLA D'ENGINYERIA De BARCELONA EST
(EEBE)

Barcelona, September 2022

Series of dissertations submitted to the
PhD program in ELECTRICAL ENGINEERING
No. 1234

ISSN 1234-5678

Print production: UPC Escuela de Doctorado

Freedom Through Truth For Service.
Libertad a través de la verdad para el servicio.
—John Leighton Stuart

Preface

This PhD program is supported by the Electric Engineering Department, Polytechnic University of Catalonia (EEBE-UPC).

In conducting the research over two years, I went through some rough stuff, also achieved some small steps. In this period, I not only obtained academic knowledge and practical experience but also understood the cooperation with a team is an important road to success. I'm further driven by the unshakable faith of "Freedom Through Truth for Service."

I couldn't finish the PhD project without many people's help. First, my supervisor, Prof. Jose Matas deserves a special thanks for his supervision and care. During the two years, he helped me in many ways: by helping me determine the research target, by discussing with patience, by revising papers carefully, and by providing help in life. He is so knowledgeable and humble, and the period working with him in Barcelona is so memorable.

I'm also grateful to Prof. Josep M. Guerrero, who is my external supervisor, for his willingness to supervise me in deriving equations, building models and checking the results.

I would also like to thank Dr. Yuan Yao, Dr. Jorge El Mariachet and Carlos Gustavo C. Branco for their advice, support, and help to revise the papers. They offered me much help, not merely on the proposal but also in life. One more respectable name that ought to be mentioned is Prof. Remus Teodorescu and Prof. Juan C. Vasquez for their academic support in understanding the research topics.

Lastly, I must say thanks to my family, colleagues at UPC, and friends for their support and encouragement.

Mingshen Li
Barcelona, September 2022

Abstract

Since the penetration of renewable energy sources such as photovoltaics, wind and fuel-cells has became increasingly an indispensable part of the new generation of the power grid network, the inverters as power interfaces are expected to play critical roles in a highly distributed AC power systems. The grid-forming control of the primary level in AC microgrids has been developed for two decades, but the droop control, as a widely used method, has some peculiarities as slow dynamic, highly coupling of active/reactive power and inaccuracy on power sharing. In the droop control, the bandwidth of the measured power has a direct impact on the controller performance, and so the calculation of the active and reactive powers is a crucial issue for the droop-controlled inverters. This dissertation firstly focuses on the design of advanced filters to improve the dynamic response for droop-based inverters when supplying linear and nonlinear loads.

In nature, the synchronization phenomena of oscillators has been encountered in several fields of science, engineering and social behavior. Regarding to the grid-forming control, this thesis is motivated by the nonlinear oscillators synchronization properties, aiming to design a simple high-performance controller for both single/three-phase inverters in stationary reference frame with faster dynamic responses to compare with the conventional primary controller.

First, a fast and accurate power calculation technique for a three-phase system by combined Second Order Generalized Integrators (SOGI) is proposed considering the utilization of linear and nonlinear loads. A two-stage combined SOGI filters are designed to obtain the active and reactive powers, which are operated in droop-based inverters. In this two-stage, the first SOGI serves as a band-pass filter (BPF) for filtering and retrieving the fundamental current of nonlinear loads. The second SOGI is used as a low-pass filter (LPF) to extract the DC component, which corresponds to the average power. In order to determine the dynamic response of the system and contrast it with the conventional LPF-droop approach, a small-signal model of a paralleled inverters system is developed. By changing the bandwidth gains, the power calculation system is designed to obtain the ripple amplitude of the average power that are equivalent to that generated from the LPF-droop.

Next, as for the islanded mode operation, a novel synchronization method based on Andronov-Hopf oscillators is proposed for paralleled single/three-phase voltage source inverters (VSI). In this case, each inverter is able to mimic the dynamics of the Hopf-oscillator. In a comparison with the nonlinear Van der Pol oscillator that is commonly used in virtual oscillator control (VOC), the Hopf oscillator shows to have lower harmonics, faster dynamic responses and higher synchronization speed. The coupling strength between Hopf oscillators relies on the local feedback of the output current, which is able to synchronize with the

rest of parallel inverters, without using communication between inverters. The Hopf-oscillator equations considering the current feedback generate the voltage reference for the power inverters, and this dual-loop is designed afterwards in a static reference frame. In order to remove a large power overshoot that is produced when an additional inverter is connected, a pre-synchronization controller is proposed. In addition, a small-signal state-space model for two parallel VSI is built, and when compared to the traditional droop controller, the root locus exhibits a larger stability margin and lower parameter sensitivity.

Besides, in order to complete the operational control of a microgrid, a grid-forming controller based on the Hopf oscillator is proposed to realize the adaptive synchronization with external periodic signals, and achieve accurate power tracking of the references. Inspired by the property of synchronization of forced oscillators, the proposed controller offers a sinusoidal ac limit cycle with improved performance and an adaptive synchronization of the frequency and phase. Meanwhile, the phase-locking region of the system is derived with respect to the current gain by using the Arnold tongue method, and the stability of the system is analyzed by using the Floquet theory. Then, considering the reactive power regulation, a PI controller is introduced to regulate the amplitude voltage based on the $Q - V$ relationship.

Furthermore, Matlab/PLECS simulation studies and experiments on a single-phase and three-phase inverters platform are conducted in a microgrid laboratory to verify the proposed control strategies. The simulations of the proposed power calculation method presents a faster and more accurate performance when sharing nonlinear loads compared with the LPF-droop. In the case of the Hopf oscillator controller, the simulation and experimental results demonstrate a faster transient response and better robustness compared with the standard droop controller, and a wider operating range compared with the Van der Pol controller. The experimental results for grid-connected operation verified the merits of the proposed controller in aspects of fast response and robustness for power and frequency tracking. So to summarize, this PhD program offers a novel and simple way to design the primary control in the operation of a microgrid.

Contents

List of Figures

List of Tables

Chapter 1

Introduction

In this chapter, the background and motivation of this PhD project are presented. Furthermore, the state of the art, research objectives and methodology are introduced, and the contribution and limitation of this research are also explained. For understanding the report clearly, the thesis outline with the selected papers is given at the end.

1.1 Background and motivation

Due to the fossil energy depletion and environmental pollution, the world is trying to switch from fossil-fuel sources to renewable energy sources such as sun, wind and biomass, which mark the development of clean energy as an inevitable trend. As an environmentally friendly and flexible power generation form, the distributed generation (DG) has been developed for decades, which plays a sustainable and effective role in coordinating different renewable sources into a new generation grid [1, 2]. Compared with the traditional distribution system, DG manifested more difficulty to analyze, lower stability in steady and transient state and unpredictable and uncontrollable operation with high penetration of renewable sources [3, 4].

To solve the problems of clean energy large-scale access to DG, and coordinated control of the distributed sources and grid, the microgrid concept appeared as a solution and has been the subject of a wide-researching during decades. Microgrid is a smaller portion of a macrogrid, which integrates multiple distributed energy sources, various loads, energy storage systems and advanced management [5, 6]. A typical microgrid structure is shown in Fig. 1.1(a). A microgrid is able to connect to the utility grid with renewable sources, and also operate off the grid to supply local loads. Therefore, grid-connected mode and islanded mode are two operating modes for a microgrid [7, 8]. As an effective way to build the future smart grid, microgrid technology has made substantial progress in recent years. The global microgrid market size and its prediction from 2022 to 2027 is illustrated in Fig. 1.1(b), and the capacity is anticipated to grow at over 20.1% from 2020 to 2027 [9, 10].

Power converters, which serve as the interfaces between distributed generation sources and the utility grid, are crucial components of the microgrid architectures as they convert power, stabilize the output current or voltage, enhance power quality, and optimise power operation. It is obvious that the control of power converters is necessary for realizing these functions. Generally, a microgrid hierarchical control comprises three levels: primary control, secondary control and tertiary control [11, 12].

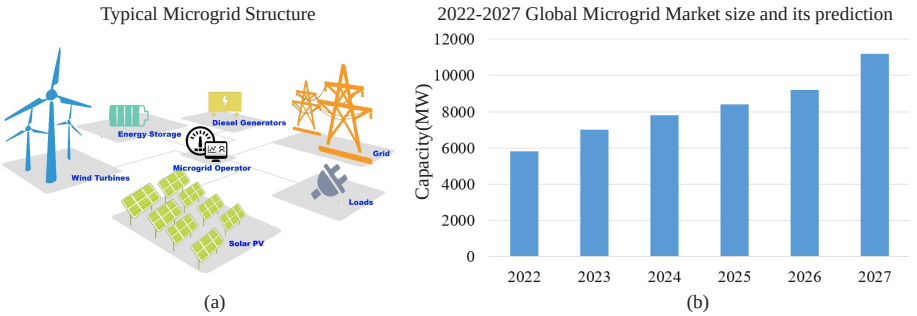

Fig. 1.1. (a) A typical configuration of a microgrid. (b) Global microgrid market size and its prediction from 2020 to 2027.

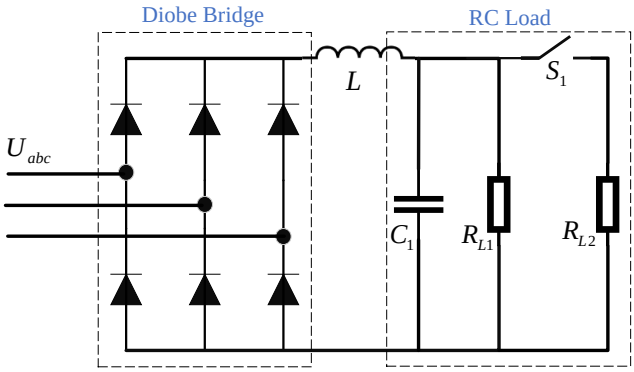

Fig. 1.2. Three-phase Diode-bridge rectifier nonlinear load.

In details, as an inner type control, the primary control is intended for the power sharing, stabilizing voltage or current output and improving dynamic response. The secondary control should reduce the derivation of frequency and voltage, and the tertiary control is responsible for power management optimization between the microgrid and the utility grid. The microgrid hierarchical control typically uses the droop control method [13–15].

Regarding the power quality, the connection of power electronic devices and nonlinear loads causes voltage and current distortions due to the limited capacity and dispersed distribution of DG, as well as inadequate power harmonic sharing within the microgrid. Nonlinear loads will inject large amounts of harmonic currents into the grid, causing voltage distortions at the common bus, that leads to current distortions and deterioration of power quality [16, 17]. Figure 1.2 illustrates the circuit of a nonlinear load where a three-phase diode-bridge rectifier is connected to a RC load. When a nonlinear load is connected to a microgrid it introduces distortions in the current and voltage that require the use of a LPF in the active and reactive power calculations. The LPF is traditionally used in the droop controllers for filtering these distortions and

achieve the averaged powers. The cut-off frequency of these LPFs are designed to be really small, which give to the droop method a slow transient response to changes in the loads. Additionally, in order to ensure appropriate functioning and reduce the total harmonic distortion (THD) of the inverter output voltage, the cut-off frequency of this LPF should be considerably smaller than the pass-band of the inverter's voltage control [18]. And, this fact slows down the system dynamics. Thus, it is a challenge to improve the power quality and provide a fast response regarding the standard droop-based decentralized controller.

As the power fluctuation from the PV and wind farms leads to microgrid instability, it is essential to develop technologies to compensate for lacking of inertia and the stabilization of the power supplies. The grid forming inverter, as a new type of interface, is an integrated technology that dispatches the desired power, and provides synthetic inertia to maintain the grid frequency to form and maintain a healthy grid [19]. In addition, a grid forming inverter should react fast when the renewable energy output has rapid fluctuations and the system operates in islanded mode and has to provide resiliency in face of some extreme events [20]. The control objectives of grid forming inverters can be summarized as: synchronization with stiff grids, sharing power under parallel operation, detecting islanded and grid-connected modes, remaining connected during transient events, and fault ride-through voltage recovery [19, 21]. For this new type of inverter, unlike the rotating mechanical dynamics of traditional generators, stabilizing voltage and frequency for both modes, realizing black-start of multiple inverters are the major challenges in the microgrids.

In nature, synchronization is an interesting phenomenon that indicates the rhythm of the oscillations of two or more systems that are coupled by interactions. For example, the spontaneous synchronization of metronomes, of the heart cells, of the fireflies etc. An oscillator is a nonlinear system which produces the repetitive variation of steady state energy. In physics it's usually a form of the circuit with a inductor and a capacitor in parallel connection. Oscillators are generally divided into two categories: harmonic oscillators and relaxation oscillators. A simple harmonic oscillator case in physics is shown in Fig. 1.3, where the motion is linked with the vertical position of the circle radius. There is an interaction in weakly coupled oscillators system, in which the coupling relationship can only have a slight impact on the oscillator dynamics, which leads to a final synchronization on the system [22]. From a theoretical point of view, the synchronization are generally researched on the coupled oscillators [23]. Through some forms of interaction, coupled oscillators can achieve an identical final stated of frequency and phase locking. For the last 30 years, oscillators have found a wide range of important applications in physics, engineering, biology, and image processing with the automatic and effective control mechanisms [24–26]. The nonlinear dynamics analysis of oscillators is different from the Laplace frequency analysis in electrical field, and it makes the system to follow certain trajectories in the state space.

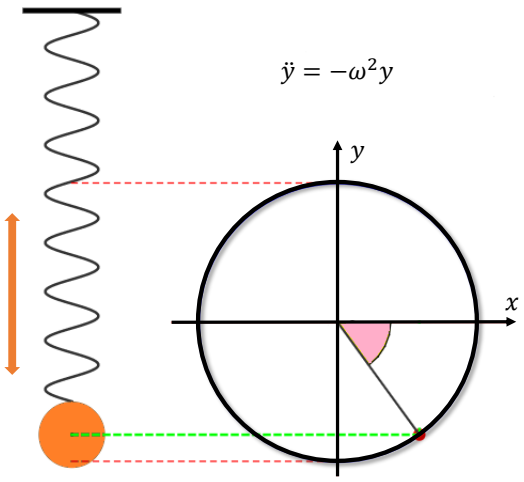

Fig. 1.3. The spring motion corresponding to a simple harmonic oscillator case.

In order to improve the stability, power quality and dynamics response of inverters in a microgrid system, the PhD work introduces a fast and simple power calculation method for nonlinear loads and a series of oscillator-based control methods to mimic the coupled oscillators synchronization phenomenon. A small signal and nonlinear dynamics analysis are employed in the investigation of the physical performance of these systems.

1.2 State of the art

As the interfaces between DG and grid, the parallel converters decide the intrinsic quality of a microgrid, where power sharing, synchronization and set-point following have emerged as the main objectives for the microgrid operation. Droop control has been widely applied to the regulation of power inverters that needs no communication, which is motivated by the synchronous generators from the traditional grids. In detail, this controller exhibits a droop characteristic between the frequency and voltage amplitude and the active and reactive output powers, respectively [27–30]. However, droop control reveals certain flaws, including inaccurate power sharing and delayed transient response caused by the LPFs, and heavily influenced by the line impedance. A series of improved droop techniques mainly come down to the decoupled power control [31–33], virtual impedance method [27, 34], re-constructed and compensated methods [35–38] to overcome these disadvantages.

Regarding supplying the nonlinear loads, a multi-functional controller that used a second order LPF to filter the harmonics was suggested in [39]. A harmonic powers' quantitative analysis was presented in [40], in which a LPF corresponding to the harmonic power calculation was introduced to the droop control scheme. However, the lower cut-off frequency of the first order LPF slows down the system dynamics and can potentially cause inverter instability.

The cut-off frequency design was investigated by using small signal model in [41], and the article indicated that the LPF has an impact on the dynamic performance, steady-state accuracy and system stability. In order to increase the power sharing accuracy, [42] offered a nonlinear neural network, specifically for the voltage and frequency regulation in a hierarchical control scheme, in which the LPF is still used as main control. In order to improve the transient dynamics and power calculation accuracy, SOGI filter has been researched to estimate the harmonic components in [43, 44]. In addition, the input signal is instantaneously filtered as a band pass filter (BPF) at the center frequency and the SOGI provides a LPF filtering in the quadrature output of the SOGI filter. In order to enhance the transient responses and accuracy of the averaged power calculation for nonlinear loads, [45] and [46] proposed a double structure SOGI filter used in the current and power calculations for a single-phase inverter, respectively.

These varied strategies mostly follow the regulation of the droop feature in essence. The voltage-current droop techniques are another approach to decentralised control. In [47], to overcome the issues related above, a virtual impedance loop-based controller was developed according to the synchronous-reference frame. However, the control bandwidth would be limited by the PLL used and the virtual impedance is difficult to build.

In order to improve the stability of current and power control, the virtual synchronous generator (VSG) was developed to make inverter's output characteristic to mimic the synchronous generator, which reduces the impacts from the large scale of renewable generation connection. In [48], smooth switching control strategies were proposed to track grid voltage by simulating self-synchronization property of VSG. In [49], an enhanced virtual synchronous generator control was proposed for reactive power sharing. However, the coupling power will affect the control system. To solve the coupling power issues, the decoupling power in active and reactive power loops method was investigated in [50], where a small-signal model of VSG was built. Nevertheless, the effects of the high frequency dynamics couldn't be represented. To sum up, There are synchronous frequency resonance problems which are pending. Another new control method called machine matching control [51, 52] tries to couple $P - \omega$ balancing by attaining a critical coupling between the DC-side voltage and the AC-side frequency. This technique allows additional inertia and damping by absorbing energy from DC-side converters.

Recently, the researches which were motivated by the oscillator synchronization characteristic have been carried out for parallel inverters in [53–56], and this theme named VOC is a type of decentralized controller. The motivation of VOC is inspired by the weakly coupling dynamics of nonlinear oscillators based on the Liénard's Theorem. In contrast with the conventional droop control, VOC exhibits competitive advantages as faster transient response, independency to loads and without secondary control. In [53–55], a virtual current source was designed as a dead-zone oscillator within the VOC circuit, then the Van der Pol oscillator was added to the micro-controller to enhance dynamics and optimize the piece-wise function of the dead-zone in [56–58]. These works illustrated the

connection between reactive power and frequency as well as between active power and terminal voltage. In addition, the small-signal stability of VOC-controlled inverters was investigated in [59] to compare with the traditional droop control. The key weakness of dead-zone and Van der Pol oscillator controller are summarized up below:

1) The entrainment basin should be constrained by a rigid adequate requirement for synchronization. The oscillations synchronise in a small entrainment basin for certain weakly coupled oscillators, which allows phase-locking dependent on a larger coupling strength [60];

2) In accordance with Liénard's Theorem, an additional limitation on limit cycles is required to achieve sinusoidal oscillations, because dead-zone and Van der Pol oscillators are typical harmonic oscillators. In order to get an optimal sinusoidal oscillation, certain conditions must be satisfied by the control parameters. The references are often chosen as an approximate limit circle in phase, which undoubtedly affects the accuracy of the references tracking performance. Consequently, the controller produces extra harmonics (such as 3^{rd} harmonics)[61];

3) The stability and the converging speed of the system are both affected by the initial states and the damping coefficient [62].

In contrast, Poincaré-Bendixson (PB) and Hopf oscillators are examples of nonlinear oscillators that are able to create perfect limit cycles which are resistant to the impacts of starting states and quickly recover from external disturbance [63]. In [64], it is suggested that converters using an adaptive frequency synchronization technique based on the PB oscillator, gives an excellent resilience against grid disturbances. In [65, 66], a dispatchable virtual oscillator control (dVOC) was presented to simulate a coupled Hopf oscillators system and implement a grid-forming application by dispatching power set-points. Like most other types of oscillators, the previous studies have not overcome the global asymptotic synchronization in theory for both internal and external cases. In addition, such expositions are unsatisfactory as the reactive power can not track the references precisely with a strong nonlinear $Q - V$ characteristic.

Taken together, the strength and weakness of the parallel inverters control strategies mentioned above can be concluded in Table 1.1.

Synchronization structures like PLL have been broadly used in grid-connected inverters. However, it limits the bandwidth of system, and the power quality is deteriorated when grid is unbalanced or distorted [67–69]. If a DC-offset is introduced to the input of PLL, it leads to oscillations in the estimated measurement signals. In addition, the inverter that employs the PLL is heavily reliant on the islanding detection, which reduces the flexibility of operation. Even though many improved filter blocks are introduced, PLL still presents an extra control part to increase the complexity of system design. However, the droop control and direct power control methods can measure the injected power to tune the inverter frequency adapted to grid [70–72]. However, these methods have clearly applied the limitation on the low-inertia system and narrow region of attraction [52].

Table 1.1: Overview for different decentralized control methods

Decentralized control method	Concept	Advantages	Drawbacks
Convectional droop control	Droop characteristics of active power and frequency, reactive power and voltage.	Non-communication; High flexibility, expandability, and reliability.	Slow dynamics due to the LPF; Poor voltage-frequency regulation; Inaccurate power sharing.
Synchronous-Reference-Frame virtual impedance loop.	Virtual impedance loop and synchronous transformation with PLL	Effective operation with different line impedance; Fast dynamics; Power sharing precision.	PLL will limit the controller bandwidth; The physical parameters should be known.
Virtual synchronous generator.	The emulation of inertial characteristics of synchronous generator.	Inertia support; Accurate active power sharing. Transient frequency stability.	Power oscillation; Errors in reactive power sharing.
Machine Matching Control	Based on Synchronous machine, frequency is driven by the DC-side voltage measurement.	Simple design; High robustness; Provide additional inertia and damping.	Strict incremental passivity; Rely on the DC-side converters; Sensitive to line impedance.
Virtual oscillator control Deadzone, Van der Pol.	Inner loop with coupled oscillator. equation	Fast dynamics; Independence to loads; No need for secondary control.	Difficult to design parameters; Initial conditions affects dynamics. Synchronization and limit cycle constraints are strict; Measurement of feedback signal is incomplete.

1.3 Objectives and Methodology

1.3.1 Objectives

The main objectives of this PhD thesis are to investigate and design an effective power calculation method and a new oscillator-based control methods of grid forming inverters in a microgrid to improve the system dynamics, study synchronization performance and analyze the stability. The research hypothesis refers to the power calculations for droop-controlled inverters under nonlinear loads, and Hopf oscillator-controlled inverters are able to synchronize adaptively for both internal inverters and external grid.

- Study and propose a fast and accurate filter based power calculation algorithm in stationary coordinates for a three-phase droop-controlled system, and analyze the stability of this system.
- Investigate and compare the system performance with different types of oscillators, such as Van der Pol oscillator and Hopf oscillator.
- Develop the control strategy to ensure making the inverter terminal voltages oscillate in unison frequency, and guarantee the stability of coupled oscillators system.
- Propose a simple oscillator control method for both single-phase and three-phase inverters in islanded microgrid system. Design the controller of time domain to make controller achieve the fast dynamics, improved power quality, independence to loads and robustness. Overcome the undesired current overshoot when inverters connect.
- Model and analyze the stability of parallel system, and investigate the parameters stability region.
- Propose an accurate power tracking method of three-phase grid forming inverters based on oscillator controller. Explore the phase-locking entrainment basin and frequency synchronization performance for the forced oscillator, and improve the controller synchronization ability for tracking frequency and locking phase without PLL.
- Verify the proposed control strategies using the simulation and experimental setups.

1.3.2 Methodology

To design and analyze the control strategies in this thesis, a series of approaches have been adopted as below:

- The Fourier series and frequency spectrum analysis are employed for harmonics components decomposition, and the bode plot and root locus are used to investigate the performance of the proposed filters.

- In order to analyze the oscillator's dynamics, the bifurcation theory is employed to observe the qualitative variations of the oscillator and equilibrium points stability when the parameter varies.

- The large-signal averaged model is used for deriving the nonlinear droop characteristics. The Jacobian evaluation of system at the equilibrium point can be applied to obtain the characteristic polynomial.

- The global asymptotic synchronization of coupled Hopf oscillator is proved by Lyapunov approach and Lasalle's invariance principle.

- The inverter model stability analysis is conducted by small-signal model in state-space.

- For synchronizing analysis between oscillator and external periodic input, the Arnold tongue method is used for searching synchronization region and the Floquet theory is applied to proof the system stability.

- The model implementation simulation has been implemented using Matlab/PLECS, and in real conditions, the controllers were implemented on dSPACE 1006 Control Desk and two Danfoss 2.2kW inverters were used with independent control loops.

1.4 Contributions and Limitations

1.4.1 Contributions

To cope with the issues of the state of the arts that are highlighted above, a fast and accurate power computation technique based on a combined SOGI filter approach has been developed, and a series of reliable and simple controllers are proposed to mimic the coupled Andronov-Hopf oscillators systems for grid forming inverters. The following list summarises this work's major contributions:

- Considering the nonlinear load supply, a two-stage combined SOGI filter is proposed for obtaining the active and reactive powers required to perform a droop-based inverter operation. This algorithm achieves a faster and accurate performance motivated by the synchronization and signal extraction accuracy of the SOGI filters.

- Provides a theoretical comparison between the proposed and Van der Pol oscillator in terms of limit cycles, responses for the perturbation, and synchronization performance.

- Gives an application of the Hopf oscillator dynamics to a parallel system of single-phase and three-phase inverters with output current feedback. The suggested controller does not include active and reactive power calculations, LPF, and PLL, in contrast to the droop controller. In comparison to VOC, the suggested controller offers better power quality and more simple parameter designing since it does not need to take into account limit cycle limitation and the strict sufficient synchronization condition. To analyze the nonlinear droop characteristics, the averaged model is derived. Global asymptotic synchronization of system is proved by Lyapunov approach, and the accurate transient stability model of proposed controller is also presented in details to analyze parameters sensitivity. The AC bus voltage is used for external synchronization to eliminate the undesired overshoot when inverters are connected.
- In view of the aforementioned issues regarding the slow transient response and parameter sensitivity controller, a novel power tracking Hopf oscillator control strategy for grid connected inverters is also proposed in this thesis. Theoretically, the phase-locking and frequency synchronization of oscillators under external periodic input are analyzed by phase dynamics and Arnold tongue methods. Meanwhile, to find out the stability region, the dynamical system stability is also analyzed by the Floquet theory. The obtained findings exhibit a quick and accurate synchronization as well as reliable performance without the need for LPF and PLL.
- Provide a new control scheme for the primary control layer of microgrid instead of the traditional droop control. Offer a innovation possibility of controller for smart grid development in both theory and experiment.

1.4.2 Limitations

- This method is based on the assumption that using a centralised controller or having properly phase-shifted carrier waveforms at the outset are possible. A communication link or other control method that produces interleaved carrier waveforms is required.
- The Hopf oscillator modeling for analysis and validation is based on same frequency references. Influence of the different frequency operation is not taken into consideration.
- The investigated experiment in the project are based on low voltage microgrid applications. The medium voltage level are not tested due to the limitations of lab setups. For medium voltage case, the results might be different, in particular the unbalanced grid or weak grid control strategies validation.
- The experiment are performed by the same clocks of inverters. The different clock will affect the integrator of each controller, which might lead to desynchrony of output signals in practice.

1.5 Thesis Outline and List of Disseminations

The outcome of this project is documented by a PhD thesis, which includes two parts: a report and related publications.

The first part is Chapter 1. Introduction, which is the preamble of the report.

Chapter 2. Proposes the combined SOGI power calculation method for three-phase droop-controlled inverter considering the nonlinear loads.

Chapter 3. Proposes the power sharing controller for parallel single and three-phase inverters in islanded mode.

Chapter 4. Proposes the power tracking controller for the grid-connected inverters.

Last chapter of the report is Chapter 5. Summary and future works.

The second part includes the selected publications that are related to this thesis (P1, J1, J2, J3). The patent and publications are listed below:

Patent

P1. Shousong O U, **Mingshen Li**, Guerrero J M, et al. Hopf oscillator based device comprising inverters: U.S. Patent Application 17/513,376[P]. 2022-2-17.

Journal Papers

J1. **Mingshen Li**, Jose Matas, Jorge EI Mariachet, Carlos Gustavo C. Branco and Josep M.Guerrero "A Fast Power Calculation Algorithm for Three-phase Droop-Controlled-Inverters Using SOGI Filters and Considering Nonlinear Loads" *Energies*, 2022, 15(19), 7360.

J2. **Mingshen Li**, Jose Matas, Carlos Gustavo C. Branco and Josep M.Guerrero "Investigation of the Hopf Oscillator Controller Algorithm Considering Grid-synchronization Capabilities for Grid-forming Inverters" *International Journal of Electrical Power & Energy Systems*, draft finished, 2022.

J3. **Mingshen Li**, Jose Matas, Shousong O, Carlos Gustavo C. Branco and Josep M.Guerrero "The Adaptive Synchronization of Parallel Inverters for an Islanded microgrid based on Coupled Hopf Oscillator" *IEEE Trans. Power Electron.*, draft finished, 2022.

Chapter 2

Power Calculation Method Based on the Combined SOGI Filters

The objective of this chapter is to improve the dynamic behavior of power calculation for the three-phase droop-controlled inverters considering nonlinear loads. The combined SOGI channels are intended to acquire the averaged power. The fundamental frequency component of load current is extracted by the SOGI-BPF. After the immediate power estimation in $\alpha - \beta$ frame, the power are filtered by utilizing the second stage SOGI-LPF to acquire the averaged PQ powers [73]. The small-signal model of two-parallel inverters system is built to proof the dynamic performance. The analysis and simulation are conducted by compared with the conventional LPF-droop method.

2.1 Combined SOGI Power Calculation Design

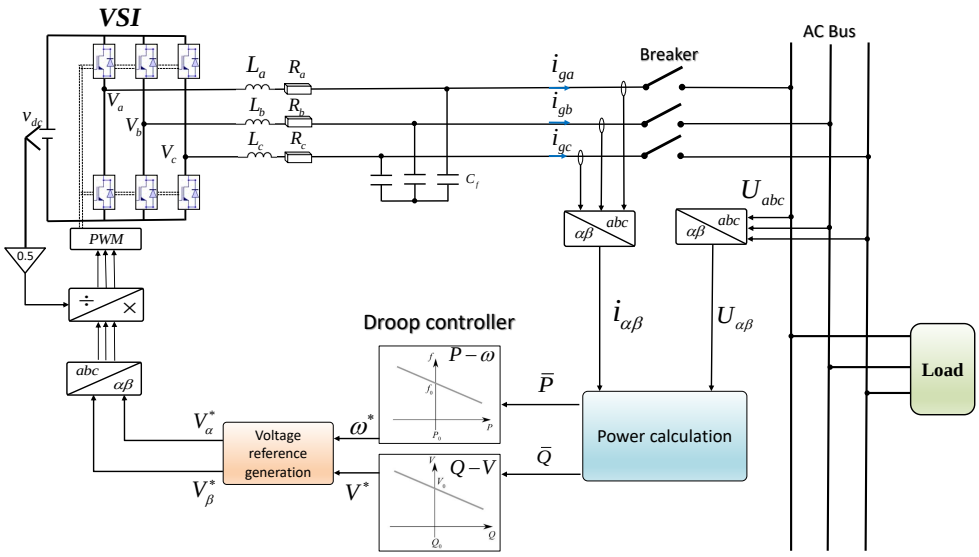

Fig. 2.1. The control scheme for the three-phase inverter in islanded mode.

Figure 2.1 indicates the scheme of the VSI controlled by the droop method when sharing a linear or nonlinear load. In general, the droop controller includes the power calculation block, the $\overline{P} - \omega$ and $\overline{Q} - V$ droop block, the voltage reference

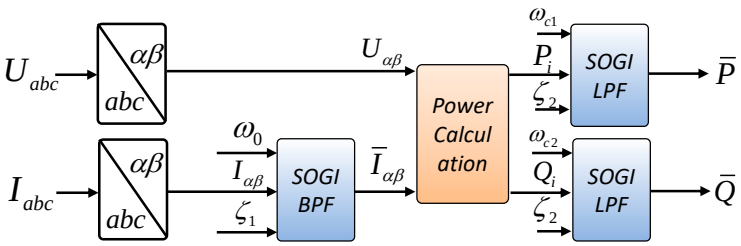

Fig. 2.2. Block diagram of the combined SOGI power calculation.

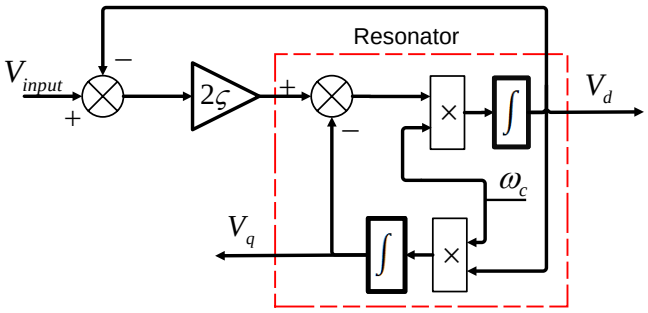

Fig. 2.3. Block diagram of the SOGI filters.

generation and PWM block. According to the droop characteristics, the load can be shared among inverters.

Figure 2.2 shows the block diagram scheme of the proposed combined SOGI method. There are two stages for SOGI filters: the first SOGI is chosen as a BPF for the obtaining fundamental current component, and the second SOGI is used as a LPF for extracting DC-component of powers.

Assuming that the system has a balanced and sinusoidal AC bus voltage. Considering that the load is nonlinear, the Fourier series decomposition can be used to analyze the distorted load currents. As an illustration, the load current for phase A can be written as:

$$i_a = \frac{2\sqrt{3}}{\pi} I_d \sin \omega t + \sum_{n=6k\pm1} (-1)^k \sqrt{2} I_n \sin n\omega t \tag{2.1}$$

where I_d and n are the rectifier DC-side current and harmonic order, respectively. Thus, the load current i_{abc} can be decomposed into a fundamental component and n-order harmonic components by using the Clarke transformation.

Figure 2.3 illustrates the SOGI filter block diagram, where V_d and V_q is the in-phase and quadrature-phase output, respectively. The characteristics of filters behave as a BPF and LPF with the following transfer functions:

$$G_{BPF}(s) = \frac{2\zeta\omega_c s}{s^2 + 2\zeta\omega_c s + \omega_c^2} \tag{2.2}$$

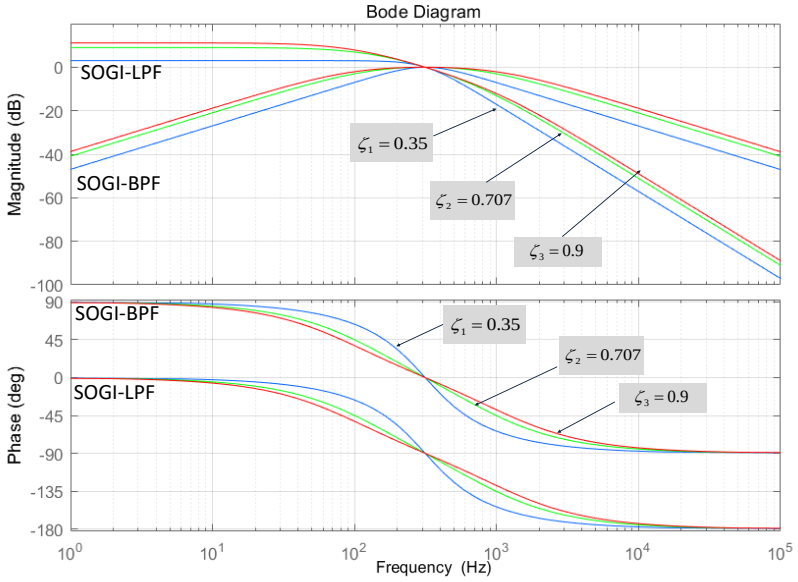

Fig. 2.4. Bode plot of the SOGI filters when damping factor changes.

$$G_{LPF}(s) = \frac{2\zeta\omega_c^2}{s^2 + 2\zeta\omega_c s + \omega_c^2} \tag{2.3}$$

where ζ is the damping factor and ω_c is the tuning center frequency. Fig. 2.4 shows the Bode plot of SOGI-LPF and SOGI-BPF when ζ changes from 0 to 1. It can be observed that ζ affects the system gain and bandwidth. Considering the phase plot, the phase lag of SOGI-LPF is 90° in contrast to the SOGI-BPF, and there is almost no phase shift for the lower frequency values for both filters, i.e.<8Hz.

Since there is no phase shift for SOGI-BPF at the center frequency as shown in Fig. 2.4, the output signal of the current SOGI filter is synchronized with the input, which allows a BPF to extract the fundamental frequency components of the inverter current. Given that there is no dc-offset for the current, the fundamental current may be written as:

$$\begin{aligned} i_{\alpha 0}(t) &= I_{\alpha 0} \sin(\omega t + \varphi_0) \\ i_{\beta 0}(t) &= I_{\beta 0} \cos(\omega t + \varphi_0) \end{aligned} \tag{2.4}$$

where $I_{\alpha\beta 0}$ are the filtered current amplitudes, which correspond with the amplitude of the fundamental components in $\alpha - \beta$ frame, and φ_0 is the phase of the fundamental component.

Thus, according to instantaneous power theory, the instantaneous active and

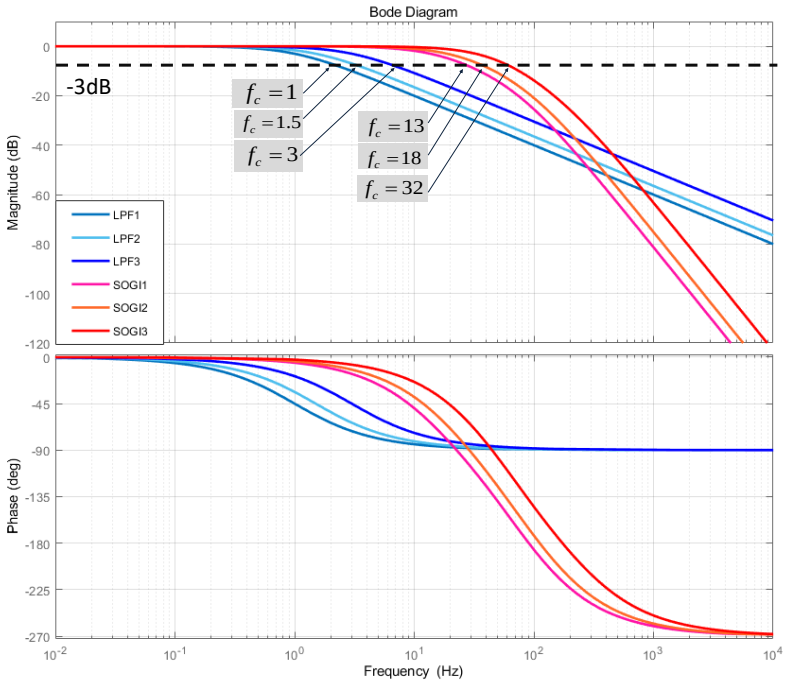

Fig. 2.5. Bode plot of the LPF-droop method and the suggested approach with various cut-off frequencies

reactive powers can be formulated as:

$$\begin{aligned} P &= v_\alpha i_{\alpha 0} + v_\beta i_{\beta 0} = 3VI\cos(\omega t) - 3VI\cos(2\omega t - \varphi_0) + 3VI\cos(n\omega t - \varphi_n) \\ Q &= v_\beta i_{\alpha 0} - v_\alpha i_{\beta 0} = 3VI\sin(\omega t) - 3VI\sin(2\omega t - \varphi_0) + 3VI\cos(n\omega t - \varphi_n) \end{aligned} \tag{2.5}$$

where V and I are the voltage and current amplitudes in $\alpha\beta$ frame, respectively, n is the harmonic components order and φ_n refers to the harmonics phase.

Consequently, the instantaneous powers are expressed as the sum of three components based on (2.5), corresponds to the averaged powers, double frequency ripples and the high order frequency components:

$$\begin{aligned} P(t) &= \overline{P} + \tilde{P} + P_n \\ Q(t) &= \overline{Q} + \tilde{Q} + Q_n \end{aligned} \tag{2.6}$$

where the superscripts " $-$ " and " $\sim$ " refer to the average and the second order frequency oscillating powers, PQ_n are the high order components.

The SOGI-LPF is used to remove the double frequency and high-order harmonic components with a cut-off frequency that is determined by the damping coefficient ζ_2. To sum up, the operating frequency delivered by the droop-method

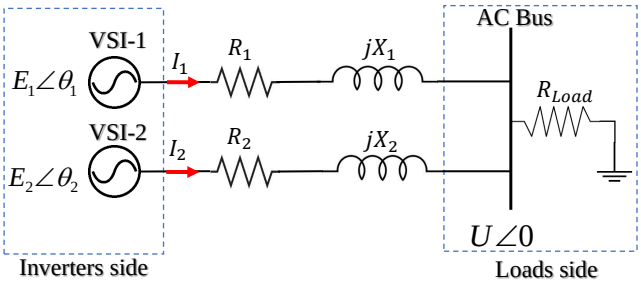

Fig. 2.6. The equivalent circuit of two parallel inverters in islanding operation.

will be the combination of the SOGI-LPF transfer function with the effect of the SOGI-BPF on the extracted fundamental component. In this case the SOGI-BPF has an effect on the envelope of the fundamental component that corresponds to a first order transfer function with constant time equal to $\frac{1}{\zeta_1\omega_n}$:

$$\begin{aligned}\frac{\bar{P}(s)}{P(s)} &= \frac{2\zeta_1\zeta_2\omega_n\omega_{c2}^2}{(s+\zeta_1\omega_n)(s^2+2\zeta_2\omega_{c1}s+\omega_{c1}^2)}\\ \frac{\bar{Q}(s)}{Q(s)} &= \frac{2\zeta_1\zeta_2\omega_n\omega_{c2}^2}{(s+\zeta_1\omega_n)(s^2+2\zeta_2\omega_{c2}s+\omega_{c2}^2)}\end{aligned} \tag{2.7}$$

In order to compare the transient response between the combined SOGI proposal and the single-LPF corresponding to the standard droop-method, the bode plot of the two power calculation methods are shown in Fig. 2.5. When their output averaged power is the same, it can be observed that the combined SOGI technique behaves like an LPF as well, and its cut-off frequency (intersect with -3dB) is a little higher than LPF-droop method. Due to the fact that (2.7) is a third-order system, the combined SOGI filter's steady-state phase shit at high frequencies is $-270°$. The combined SOGI approach exhibits phase delays at $-3dB$ that are comparable to those of the LPF-droop method. Therefore, the second and high-frequency components may be suppressed with a faster transient response using the combined SOGI approach.

2.2 Small Signal Analysis

This section's goal is to examine how the cut-off frequency of the combined SOGI filters and the traditional LPF-droop approach affect the stability and efficiency of the system. Fig. 2.6 shows the average interface circuit for a typical parallel inverters system sharing loads through an RL impedance. The voltage at the inverter sides is $E\angle\theta$, which refers to the voltage on the AC bus $U\angle 0$. Considering an inductive impedance line, PQ from inverters to the AC bus can

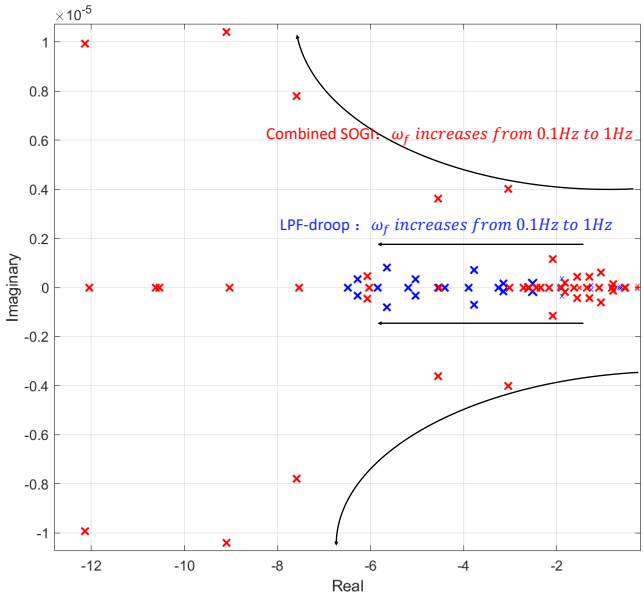

Fig. 2.7. The root locus of the LPF-droop method and the proposed combined SOGI method when ω_f varies from 0.1Hz to 1Hz.

be given as:

$$\begin{aligned} P &= \tfrac{1}{R^2+X^2}(RU^2 - REU\cos\theta + XEU\sin\theta) \\ Q &= \tfrac{1}{R^2+X^2}(XU^2 - XEU\cos\theta - REU\sin\theta) \end{aligned} \tag{2.8}$$

The disturbance errors of the powers may be stated as: for the minor disturbances, (2.8) can be linearized at an equilibrium point at steady state as:

$$\begin{aligned} \Delta P &= k_{PE}\Delta E + k_{P\theta}\Delta\theta \\ \Delta Q &= k_{QE}\Delta E + k_{Q\theta}\Delta\theta \end{aligned} \tag{2.9}$$

where Δ denotes small disturbances at the equilibrium point, and the expansion form of the parameters k are:

$$\begin{aligned} k_{PE} &= \tfrac{1}{R^2+X^2}(2RE - RU\cos\theta + XU\sin\theta) \\ k_{P\theta} &= \tfrac{1}{R^2+X^2}(REU\sin\theta + XEU\cos\theta) \\ k_{QE} &= \tfrac{1}{R^2+X^2}(2XE - XU\cos\theta - RU\sin\theta) \\ k_{Q\theta} &= \tfrac{1}{R^2+X^2}(XEU\sin\theta - REU\cos\theta) \end{aligned} \tag{2.10}$$

The minor disturbance of frequency and voltage may therefore be expressed as follows in the frequency domain:

$$\begin{aligned} \Delta\omega(s) &= -m\Delta P = G_f(s)(k_{PE}\Delta E(s) + k_{P\theta}\Delta\theta(s)) \\ \Delta E(s) &= -n\Delta Q = G_f(s)(k_{QE}\Delta E(s) + k_{Q\theta}\Delta\theta(s)) \end{aligned} \tag{2.11}$$

where m and n are the droop coefficient of the active and reactive powers, respectively, and $G_f(s)$ is the transfer function of the LPF filter used in the power calculation.

Substituting $\Delta\omega(s) = s\Delta\theta(s)$ into (2.9) and (2.11), the characteristic equation of the system considering the active power loop can be derived as:

$$(nG_f k_{QE} + 1)s\Delta\theta(s) + mnG_f^2\Delta\theta(s)(k_{P\theta}k_{QE} - k_{PE}k_{Q\theta}) + mk_{P\theta}G_f\Delta\theta(s) = 0 \tag{2.12}$$

In order to analyze the effects of ω_f of two methods, the dynamic response of the system can be determined based on the various power calculation techniques if the transfer function of the LPF-droop-based and the suggested method (2.5) are substituted into the reference equation (2.12).

The root locus for both approaches is illustrated in Fig. 2.7 when ω_f ranges from 0.1Hz to 1Hz. When ω_f grows, the pair of dominating poles for the traditional droop approach migrate down the negative real axis and towards infinite negative, implying that the system dynamic response becomes faster and the system exhibits an overdamped characteristics. In contrast, when $\omega_f = 0.1 \sim 1Hz$, the system reveals an underdamped characteristic and the prominent poles of the combined SOGI approach are likewise placed further away from the imaginary axis.

In light of the identical cut-off frequency scenario, it can be stated that the combined SOGI approach is faster than the LPF-droop method. Additionally, the combined SOGI approach has a substantially wider stability margin.

In conclusion, from the perspective of the power calculations, the cut-off frequency will have an impact on the system's stability and dynamic response, and a larger ω_f results in a faster system. The proposed solution shows a faster dynamic reaction and a wider stability margin when compared to the traditional droop controller under the same circumstances.

2.3 Simulation Results

The simulation model of the two parallel inverters with different types of loads has been built in the Matlab/PLECS environment in order to evaluate the performance of the proposed combined SOGI approach and contrast it with the traditional LPF-droop control. The characteristics of the system are shown in Table 3.1, and each inverter implements the $P-\omega$ and $Q-V$ droop characteristics with the identical slope coefficients.

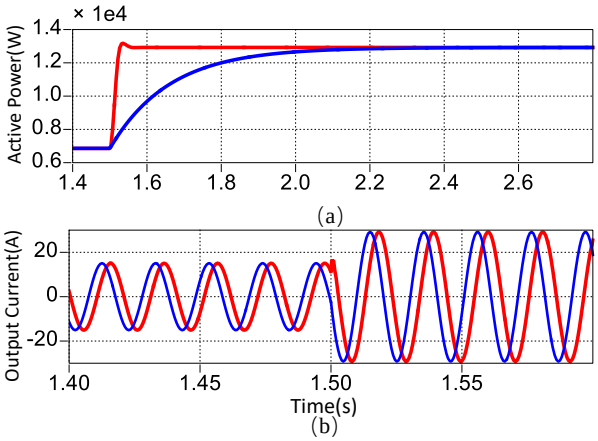

Fig. 2.8. Simulation results for a step change in the shared linear load: (a) Active powers (b) Output currents.

Table 2.1: System parameters for simulation.

Parameters	Value
Nominal output voltage	220V
Nominal frequency	50Hz
L-type filter	0.1Ω+2mH
Transmission line	0.01Ω+0.32mH
Active power droop coefficient m	0.001
Reactive power droop coefficient n	0.0001

2.3.1 Case I: A Step Change in a Linear Loads

Figure 2.8 illustrates the dynamical performance of two techniques under a resistive load step change. The LPF-droop controller is built with a 1Hz cut-off frequency. To achieve the same average power with the LPF-droop approach, the damping factors for the SOGI-BPF and SOGI-LPF are set to 0.707, and the cut-off frequencies are set to $f_{c1} = 50$Hz and $f_{c2} = 15$Hz, respectively. The transient response to a step change in output current from 15A to 30A supplying a linear load is shown in Fig. 2.8(b). From Fig. 2.8(a), the combined SOGI approach shows to be significantly faster than the LPF-droop method, with transient times recorded as 0.05sec and 0.65sec, respectively. The damping factor is responsible for the little overshoot that can be seen in the proposed method.

2.3.2 Case II: ω_f Variation Considering a Nonlinear Load

The ω_f frequency will have an impact on the settling time of the transient response and power ripples based on the root locus analysis depicted above.

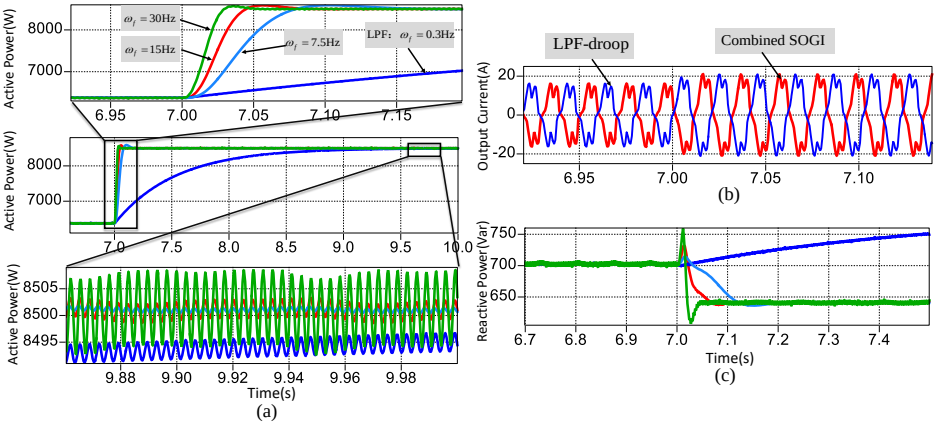

Fig. 2.9. Simulation results for RC load when ω_f varies: (a) Active powers (b) Output currents (c) Reactive powers.

Additionally, the simulation is conducted to confirm the behavior under a nonlinear diode bridge rectifier load with a THD of 28%. The combined SOGI proposal's ω_f in the SOGI-LPF ranges from 7.5Hz to 30Hz, and ω_f for the LPF-droop approach is meant to be 0.3Hz. Fig. 2.9(a) shows the dynamical response of the active power during an output current perturbation step from 15A to 20A. The proposed coupled SOGI method exhibits a faster dynamical performance in comparison to the LPF-droop approach. While the speed and ripple both increase as ω_f rises, and decrease as ω_f falls, which suggests that the theoretical analysis and the simulation findings are consistent.

It is worth noting that the power ripple of both approaches should be matched similarly in order to compare the transient response in the same conditions. As shown in Fig. 2.9(a) scaled P, the peak-to-peak value is approximately equal to 3.5W where SOGI's ω_f is 15Hz and LPF's is 0.3Hz. It can be concluded that the combined SOGI approach has a dynamic response that is substantially faster than LPF-droop method. Due to the absence of inductive loads in Fig. 2.9(c), the reactive power dynamical responses of the two techniques are also different.

Furthermore, the dynamic response of the reactive power with a variation of less than 600 Var is shown in Fig. 2.10 when the inductive loads are taken into account. The power factor has changed from 1 to 0.99746 since 2.5s. The combined SOGI approach is significantly faster than the LPF-droop method, just like the active power. Additionally, the transient is slower and the steady-state ripple is smoother when ω_f is lower.

2.3.3 Case III: ζ_1 Variation Considering a Nonlinear Load.

In this instance, the RL nonlinear loads are taken into account while changing the SOGI-BPF's damping ratio from 0.56 to 0.9. For the combined SOGI and LPF-droop approaches, the cut-off frequency is set as 15Hz and 0.3Hz,

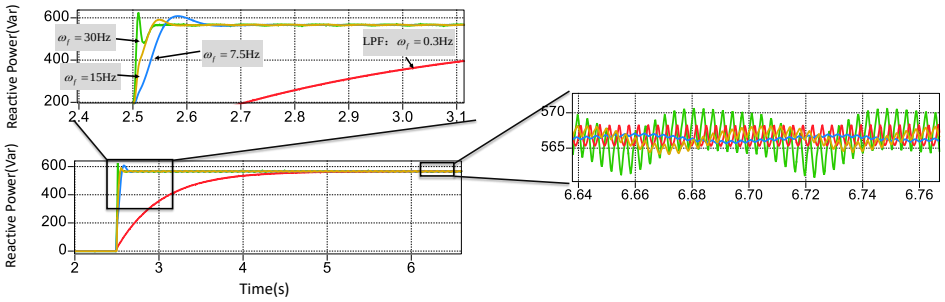

Fig. 2.10. Simulation results for a RL load when ω_f varies.

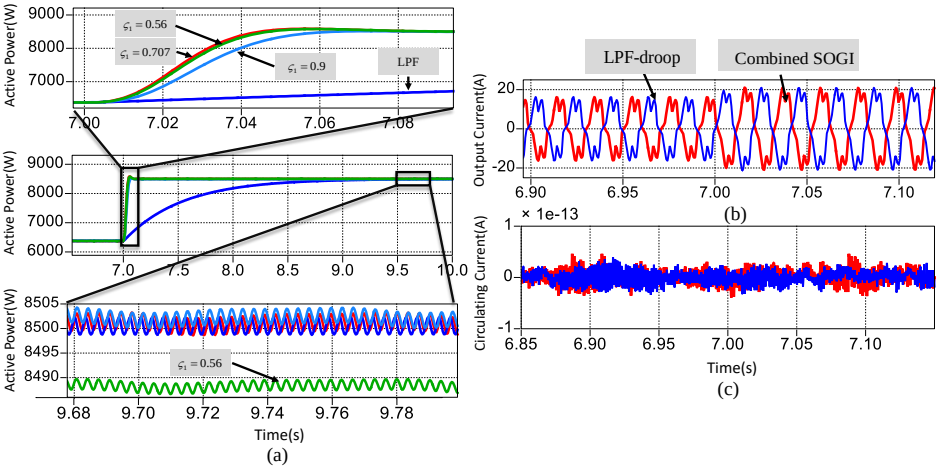

Fig. 2.11. Simulation results when ζ_1 varies: (a) Active powers (b) Output current (c) Circulating currents

respectively, to produce the same power ripple. A nonlinear load current step perturbation occurs from 15A to 20A in Fig. 2.11(b). When ζ_1 is increased, the active power's transient response in Fig. 2.11(a) slows down, but it still exhibits faster dynamics than the LPF-droop. Furthermore, as the amplitude of the current reduces through the smaller damping ratio of the SOGI filter, the RMS value of the active power has been reduced in the case of $\zeta_1 = 0.56$.

According to Fig. 2.11(c), the circulating current between the inverters is practically negligible for both techniques. ζ_1 is often selected to be 0.707 as a known ideal trade-off for the sake of the conventional design.

Chapter 3

Hopf Oscillator Control for islanded Inverters in a Microgrid

This chapter introduces the design and analysis of Hopf oscillator control method for parallel inverters for both single-phase and three-phase systems. In the islanded mode, each inverter is controlled to emulate the weakly coupled nonlinear oscillator system synchronization performance. The comparison between Hopf and Van der Pol oscillators in terms of physical property are conducted under the same situations. Particularly, the Hopf oscillator controller implementation are presented. In addition, a global asymptotic synchronization of coupled Hopf oscillators is proved, and the stability of Hopf oscillator controlled inverter is analyzed. At last, the simulation and experiment results validate the effectiveness of proposed controller [74, 75].

3.1 Hopf and Van der Pol Oscillator Dynamics and Their Comparison

The following second-order differential equations can be used to describe the Hopf oscillator's normal dynamics [76]:

$$\begin{cases} \dot{x} = \mu(r^2 - x^2 - y^2)x + \omega y \\ \dot{y} = \mu(r^2 - x^2 - y^2)y - \omega x \end{cases} \tag{3.1}$$

where x and y are in-quadrature states, μ controls the oscillator's damping speed, r denotes the output amplitude in steady state, and ω determines the oscillation frequency.

The Van der Pol oscillator, on the other hand, is a classical relaxation harmonic oscillator that is popular in VOC [53, 55]. A second-order differential equations of the Van der Pol oscillator may be stated as follows:

$$\begin{cases} \dot{x} = y \\ \dot{y} = \mu(1 - x^2)y - \omega^2 x \end{cases} \tag{3.2}$$

where x and y are in-quadrature states as well, ω affects the frequency of the oscillations and μ is the damping coefficient that dictates the system's degree of relaxation.

Considering the second-order differential equations, the steady-state periodic solutions of Hopf oscillator can be obtained as:

$$x = rsin(\omega t + \theta_0), y = rcos(\omega t + \theta_0) \tag{3.3}$$

where the starting state determines θ_0.

The vector field and series of trajectories in the phase plane from the initial condition $(0, 0)$ are represented in Fig. 3.1, which visualizes the flow's direction and intensity. Besides, a narrow orbit circle is produced when the solutions are orthogonal signals in steady-state. When the damping parameter r is modified from an unit to a non-null value, the 3-D bifurcations diagram is shown in Fig. 3.2 [77–79]. the performance of Hopf oscillator is consistent with increasing amplitude. In order to better visualize the bifurcations, the level sets of approach times with the periodic orbit are able to presented in isochron corrdinates as shown in Fig. 3.3, and the isochron coordinate field spirals away from the original state corresponding to the phase dynamics $\omega + \theta_0$.

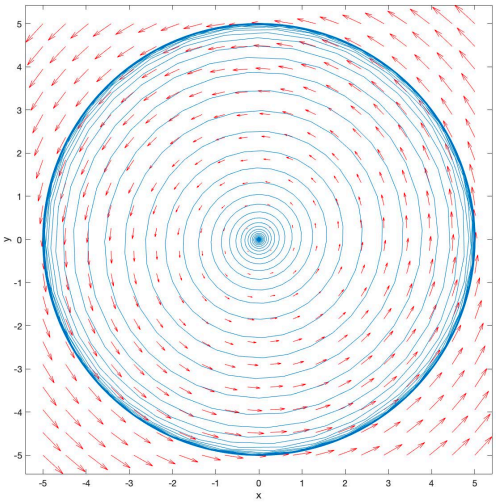

Fig. 3.1. Vector field of the Hopf oscillator in phase plane

The characteristics of the two types of oscillators are presented below in terms of limit cycle, robustness, and synchronization capabilities in order to compare with Hopf oscillator.

1) **Limit cycle property**. The limit cycle comparison for various damping coefficients are shown in Fig. 3.4. In Fig. 3.4(a), the limit cycle evolution of the Van der Pol oscillator becomes sharper with increasing μ, while the amplitude of the states remains constant. Thus, a Van der Pol oscillator belongs to a harmonic oscillator. In contrast, the limit cycles in Fig. 3.4(b) maintain an ideal circle regardless of changes in μ, and μ will affect the damping speed for the Hopf. As a result, the Van der Pol oscillator must adhere to severe parameters constraints in order to be a perfect circle, whereas the damping coefficient for the Hopf oscillator phase portrait is unrestricted.

In order to proof the harmonics characteristics of the two oscillators, the harmonic analysis of the unforced Hopf and Van der Pol oscillator dynamics is investigated. The Poincaré-Lindstedt approach [80, 81] is employed to estimate the limit cycle while obtaining the harmonic solutions for a nonlinear system.

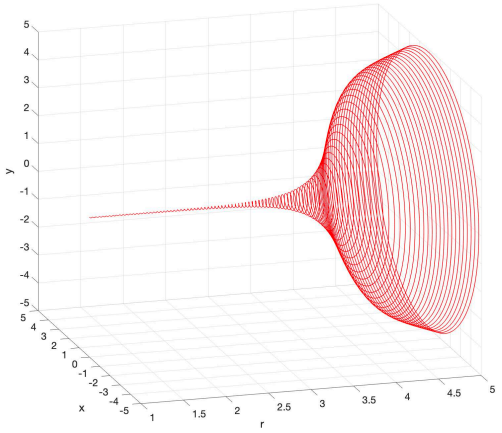

Fig. 3.2. Hopf oscillator bifurcations with r changing.

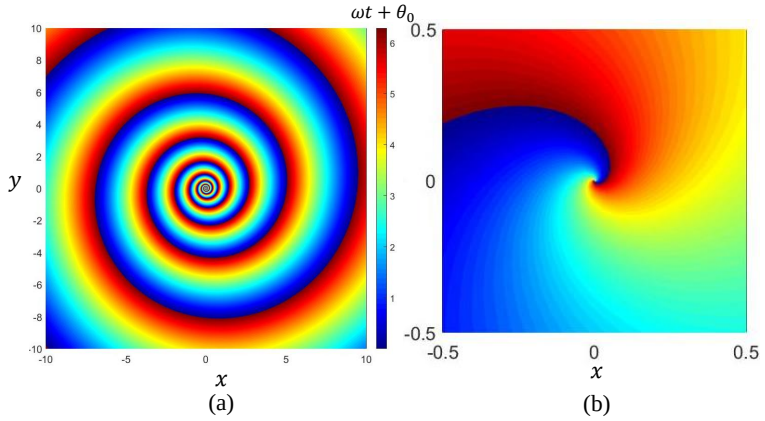

Fig. 3.3. The isochron coordinate fields of the Hopf bifurcation:(a) $\omega = 100\pi$ and $r = 10$. (b) Amplified field within 0.5.

The second order equation of the Hopf oscillator with a new time variable $\tau = \omega_t$ could be generated by taking into account of the input current $i = 0$ for simplifying the systems:

$$\omega^2 x'' + x = \varepsilon\mu\omega(r^2 - x^2 - x'^2)x' = \varepsilon f(x) \tag{3.4}$$

where a minor parameter is properly denoted by ε.

The oscillations' natural time scale can be expressed as:

$$\begin{aligned} x_\varepsilon(\tau) &= x_0(\tau) + \varepsilon x_1(\tau) + \dots \\ \omega_\varepsilon &= \omega_0 + \varepsilon\omega_1 + \dots \\ f(x,\varepsilon) &= f_1(x) + \varepsilon f_2(x) + \dots \end{aligned} \tag{3.5}$$

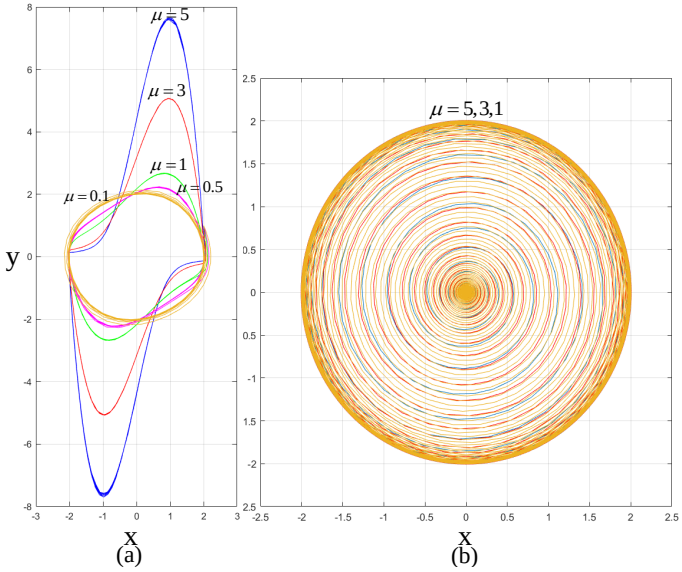

Fig. 3.4. Limit cycles evolution with varying μ in the phase plane: (a)Van der Pol oscillator. (b) Hopf oscillator.

The equations up to second order in terms of ε can be expressed by replacing (3.5) for (3.4):

$$\begin{aligned} x_0'' + x_0 &= 0 \\ x_1'' + x_1 &= f_1(x_0) - 2\omega_1 x_0'' \\ x_2'' + x_2 &= f_2(x_0) + \frac{\partial f_1(x_0)}{\partial x_0} x_1 - 2\omega_1 x_1'' - (\omega_1^2 + 2\omega_2) x_0'' \end{aligned} \tag{3.6}$$

Assume that $x_0(0) = a$ for the starting state and the zero order is a simple oscillation with the solution $x_0(\tau) = acos\tau$. The zero order solution is substituted for the first order and second order equations, and the first order equation can be obtained as:

$$x_1'' + x_1 = a\mu(a^2 - r^2)sin\tau + 2\omega_1 acos\tau \tag{3.7}$$

Choose $a = r, \omega_1 = 0$ to avoid the secular term, the the answer is $x_1(\tau) = acos\tau$ as well. The second order equation is expressed as:

$$x_2'' + x_2 = a\varepsilon\mu(a^2 - r^2)sin\tau + a\mu(a^2 - r^2)cos\tau + 2\omega_1 cos\tau + (\omega_1^2 + 2\omega_2)cos\tau \tag{3.8}$$

Next, choose $a = r, \omega_1 = 0, \omega_2 = 0$ to remove the resonant forces from the right side of the equation. $x_2(\tau) = acos\tau$ is the second order equation's

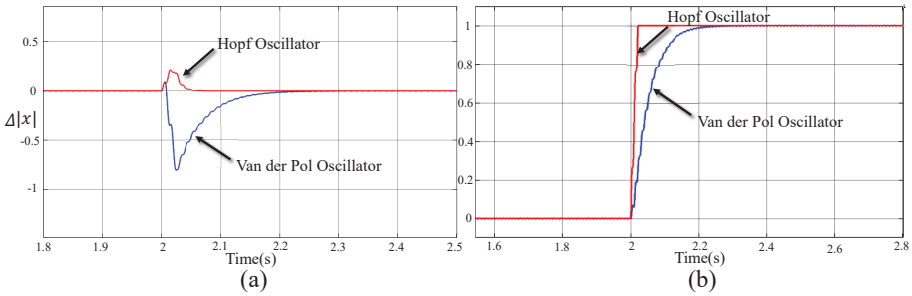

Fig. 3.5. Dynamic response comparison for the state amplitude error: (a) To the unit impulse. (b) To a step change.

solution. As a result, the approximate Hopf oscillator solution oscillates at the fundamental frequency ω_0. Similar to this, the first order expansion for the Van der Pol oscillator $\omega^2 x'' + x = \varepsilon\omega(1 - x^2)x'$ can be obtained by:

$$x_1'' + x_1 = -(x_0^2 - 1)x_0' - 2\omega_1 x_0'' = 2a\omega_1 cos\tau + a(0.25a^2 - 1)sin\tau + 0.25a^3 sin3\tau \tag{3.9}$$

Choose $\omega_1 = 0, a = 2$ for the elimination of the resonant forces, and the first order solution is $x_1(\tau) = sin^3\tau$. When $a \to 0$, the right side is close to zero and the oscillator's solution is $x_1(\tau) \approx acos\tau$. Taking into account the second order case, the equation is expressed as:

$$x_2'' + x_2 = (4\omega_2 + 11)cos\tau - 31cos^3\tau + 20cos^5\tau \tag{3.10}$$

With $\omega = 1 - 0.0625\varepsilon^2 + \ldots$, the approximate solution is $x_2(\tau) = 2cos\tau + \varepsilon sin^3\tau + \ldots$. As a result, the harmonics in the Van der Pol's solution have amplitudes that are inversely proportional to ε. In conclusion, the three order harmonics are included in the approximate solution expansion of the harmonic oscillator known as the Van der Pol oscillator. The hopf oscillator, in contrast, has a solution that is orbitally exponentially stable at the fundamental frequency.

2) **Robustness**. In Fig. 3.5, the robust characteristics of the two oscillators in transient dynamics considering the impulse and step inputs is shown . The parameters situation for the Hopf and Van der Pol oscillators are $\mu = 0.1$, $r = 1$, and $\omega = 20\pi$. The Hopf oscillator shows a noticeably quick recovery in Fig. 3.5(a), but the Van der Pol oscillator removes the error slowly for the unit impulse of amplitude. On the other side, the step response of the Hopf oscillator is faster than that of the Van der Pol, as seen in Fig. 3.5(b).

3) **Synchronization**. A performance comparison of the two types oscillators for coupled synchronization is presented in Fig. 3.6. The Kuramoto model is satisfied by the coupled Van der Pol and Hopf oscillators, which all belong to

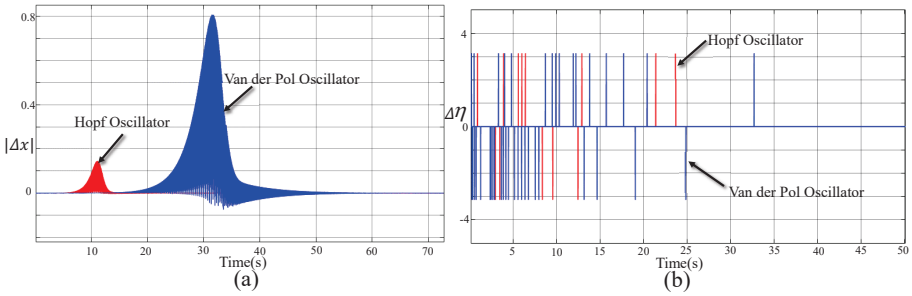

Fig. 3.6. Dynamic comparison for assessing the synchronization performance: (a) The amplitude error. (b) The phase error.

the weakly coupled oscillator. Owing to the weak interaction, they are able to adjust their rhythms of oscillation with initial frequency. Identical values for the parameters of two oscillators are chosen for fair comparison: $\mu = 0.1$, $r = 1$ and $\omega = 20\pi$. The coupling strength is defined as $= 0.25$. As a result, the definition of the amplitude and phase coupling error in steady state can be given by:

$$\begin{aligned} |\Delta x| &= \gamma(|x_1| - |x_2|) \\ \Delta\eta &= \gamma(\eta_1 - \eta_2) \end{aligned} \tag{3.11}$$

where $|x_1|$, $|x_2|$, η_1 and η_2 are the amplitude and phase of two connected oscillators in steady state, respectively.

Fig. 3.6(a)(b) show the synchronization patterns of the amplitude and phase errors for the Van der Pol and the Hopf oscillators. The mechanisms for each of them begin with the starting circumstances and reach a final synchronization. When compared to a Van der Pol oscillator, a Hopf oscillator exhibits a faster transient on both amplitude and phase, as well as the less amplitude overshoot.

In conclusion, the Hopf oscillator clearly outperforms the Van der Pol oscillator in terms of less harmonics, better robustness and faster synchronization. Thus, the thesis employs the Hopf oscillator as the controller in the following contents.

3.2 Control Implementation and Parameter Design

3.2.1 Single-phase Controller Design

The Hopf oscillator is applied to a single-phase inverter using a simplified equation for the reference generation that also incorporates the Hopf oscillator's characteristic. The following differential equations can be used to explain the dynamics of the modified Hopf oscillator controller based on (3.1) in continuous domain:

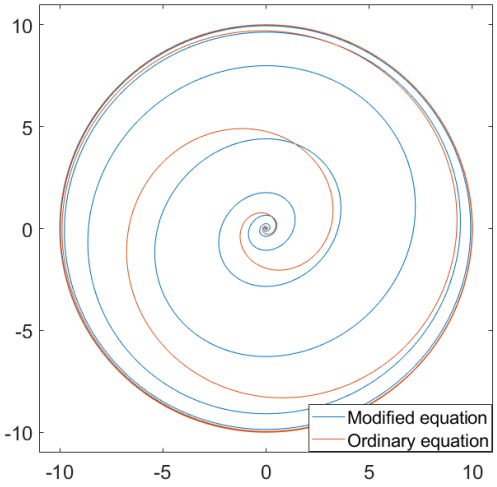

Fig. 3.7. Limit cycle comparison of the modified and ordinary Hopf with $r = 10$, $\omega = 100\pi$.

$$\begin{cases} \dot{V}_\alpha = \mu(V^{*2} - V_\alpha^2 - V_\beta^2)V_\alpha - \omega V_\beta - ki \\ \dot{V}_\beta = \omega V_\alpha \end{cases} \tag{3.12}$$

where V_α,V_β are the two states of the oscillator, i refers to the output current as an external periodic perturbation, k is the current gain and V^* determines the steady-state amplitude of the oscillation ($V_{\alpha\infty}^2 + V_{\beta\infty}^2 = V^{*2}$).

Figure 3.7 illustrates the trajectories of the modified Hopf oscillators and the ordinary from (3.12), and their orbits converge to the same limit cycle with the fixed amplitude and frequency. It indicates that the modified equation have the same steady-state solutions as the ordinary Hopf.

Figure 3.8 shows the Hopf oscillator controller implementation for the single-phase inverters. The system contains the DC source, a full-bridge inverter, and a LC filter. The time-domain controller is a simple voltage loop with the current feedback. The equations (3.12) generate the orthogonal state signals V_α and V_β, and one state V_{alpha} is chosen as the voltage reference based on the amplitude reference V^* and frequency reference ω^*. The PWM input is the voltage reference divided by the dc-link voltage in order to decouple the dc-link dynamics. In light of this, the proposed controller is an inner loop controller, which only requires the monitoring of the output current and dc-link voltage without power calculation and PLL.

It is challenging to monitor the behavior of the nonlinear differential equation on a time scale, the averaged model is used to generate approximations of the periodic solutions by substituting an average vector field.

The system is represented as polar coordinates in the phase dynamics. The phase dynamics of the Hopf oscillator based on (3.12) are derived by

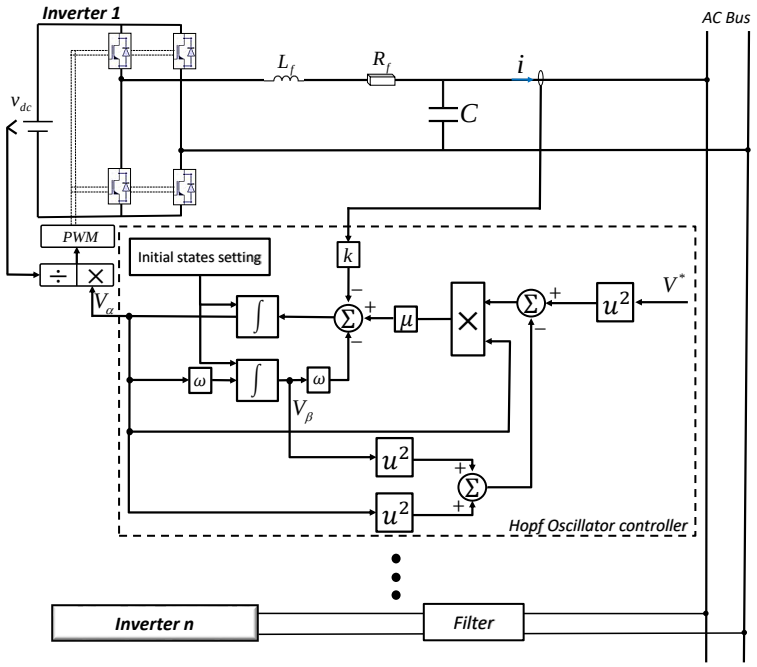

Fig. 3.8. The proposed control structure for the single-phase inverters.

differentiating $V_\alpha = Vsin(\theta)$ and $V_\beta = Vcos(\theta)$ in time domain:

$$\begin{cases} \dot{V} = \mu(V^{*2}V - V^3)cos^2(\theta) - kicos(\theta) \\ \dot{\theta} = \omega - \mu(V^{*2} - V^2)sin(\theta)cos(\theta) + \dfrac{ki}{V}sin(\theta). \end{cases} \tag{3.13}$$

where θ is the instantaneous phase angle. The average value of a periodic signal $V(t)$ throughout a period T is therefore shown by:

$$\bar{V} = \frac{1}{T}\int_0^T V(t)dt \tag{3.14}$$

The dynamics of the inverter terminal voltage are specified as follows to help streamline the averaged model [56]:

$$\frac{d\theta}{dt} = \omega + \frac{d\varphi}{dt} = \omega^* + \frac{d\varphi^*}{dt} \tag{3.15}$$

where the nominal frequency of the inverter outputs is ω and the steady-state frequency is $\omega*$. The phase offset with regard to ω and $\omega*$ is shown by the angles φ and $\varphi*$, respectively. The Hopf oscillator dynamical system with a 2π-periodic

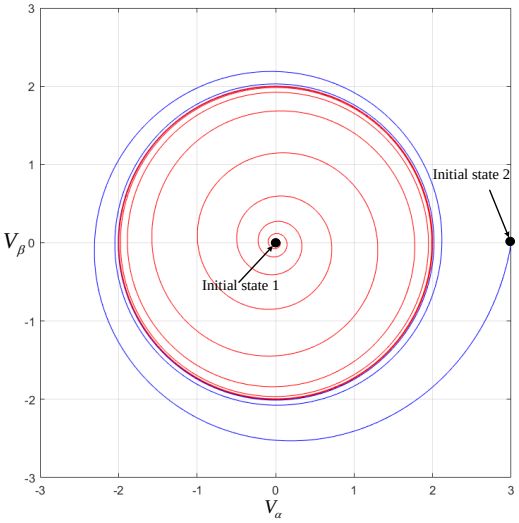

Fig. 3.9. The convergent trajectories for the Hopf oscillators with the different initial states.

function is therefore given in the averaged model as follows:

$$\begin{cases} \dot{\bar{V}} = \frac{\omega^*}{2\pi}\int_0^{\frac{2\pi}{\omega^*}} \mu(V^{*2}V - V^3)cos(\omega^* t + \varphi^*)^2 dt \\ -\frac{\omega^* k}{2\pi}\int_0^{\frac{2\pi}{\omega^*}} icos(\omega^* t + \varphi^*)dt \\ \dot{\bar{\varphi}}^* = -\frac{\omega^*}{2\pi}\int_0^{\frac{2\pi}{\omega^*}} \mu(V^{*2} - V^2)sin(\omega^* t + \varphi^*) \\ cos(\omega^* t + \varphi^*)dt + \frac{\omega^* k}{2\pi \bar{V}}\int_0^{\frac{2\pi}{\omega^*}} isin(\omega^* t + \varphi^*)dt. \end{cases} \tag{3.16}$$

The averaged dynamics of the amplitude and phase are stated as follows:

$$\begin{cases} \dot{\bar{V}} = \frac{V^{*2}\mu}{2}\bar{V} - \frac{\mu}{2}\bar{V}^3 - \frac{k}{\bar{V}}\bar{P} \\ \dot{\bar{\theta}} = \omega^* - \omega + \frac{k}{\bar{V}^2}\bar{Q}. \end{cases} \tag{3.17}$$

where P and Q are the instantaneous inverter output active and reactive powers, respectively.

The initial states of the oscillator, the damping coefficient μ, and the current gain k are the components of the proposed controller's parameters, which are used to complete the design process as follows:

1) **Initial states**: The coupled Hopf oscillators always reach a limit cycle regardless of where the initial states are located as shown in Fig. 3.9. The trajectory of two coupled Hopf oscillators with various initial states and their orbits toward a limit cycle with a constant amplitude and frequency. But, the starting state is set to ($0.5V_{rate}$,0) where V_{rate} is the rated voltage of the inverter due to the convergence speed and safe startup in reality.

Next, the sufficient synchronization conditions theorem is constructed based on (3.12) in order to demonstrate the asymptotic synchronization performance of the connected oscillators. The Lyapunov technique is used to obtain the precise requirements for weakly coupled oscillators [82–84]. The differential equations for Hopf oscillators with N coupling are written as:

$$\begin{cases} \dot{x_i} = \mu({r_i}^2 - x_i^2 - y_i^2)x_i - \omega y_i + k \sum_{p=1}^{N} (x_p - x_i) \\ \dot{y_i} = \omega x_i \end{cases} \forall i = 1, ...N. \tag{3.18}$$

For each oscillator, the synchronization in steady state can be defined as follows:

$$\lim_{t\to\infty} (x_j - x_i) = 0, \lim_{t\to\infty} (y_j - y_i) = 0, \quad \forall j, i = 1, ...N. \tag{3.19}$$

Thus, according to (3.18) (3.19) , the formula for the synchronization's derivative is:

$$\begin{cases} \dot{x_j} - \dot{x_i} = \mu({r_j}^2 - x_j^2 - y_j^2)x_j - \mu({r_i}^2 - x_i^2 - y_i^2)x_i \\ -\omega(y_j - y_i) + kN(x_j - x_i) \\ \dot{y_j} - \dot{y_i} = \omega(x_j - x_i) \end{cases} \tag{3.20}$$

As explained in 3.1, in contrast to the Van der Pol, the closed orbit of the Hopf oscillator is stable, and it exhibits a good robustness performance. Assume that $x_{i\infty}^2 + y_{i\infty}^2 = {r_i}^2$ with feedback components k_i, and each oscillator has the same frequency. *Theorem I* is suggested to create sufficient synchronization with regards to $k > 0$.

Theorem I: Consider the dynamics in (3.18) of a coupled oscillator system, for variables $x_i,\ x_j,\ y_i,\ y_j \in \mathbf{R}, \forall j, i = 1, ...N.$, as $t \to \infty$, the coupled Hopf oscillators synchronize asymptotically, if parameters $k > 0$.

Proof: Define the Lyapunov function S_{ij} function as:

$$S_{ij} = \frac{1}{2}(x_j - x_i)^2 + \frac{1}{2}(y_j - y_i)^2 \tag{3.21}$$

By differentiating (3.21), the Lyapunov function can be expressed as:

$$\begin{aligned} \dot{S_{ij}} = &- kN(x_j - x_i)^2 + x_j(x_j - x_i)({r_j}^2 - x_j^2 - y_j^2) \\ &- x_i(x_j - x_i)({r_i}^2 - x_i^2 - y_i^2)x_i \\ &- \omega(x_j - x_i)(y_j - y_i) + \omega(x_j - x_i)(y_j - y_i) \end{aligned} \tag{3.22}$$

Note that $x_{i\infty}^2 + y_{i\infty}^2 = {r_i}^2, x_{j\infty}^2 + y_{j\infty}^2 = {r_j}^2$ in early, and simplify (3.22):

$$\dot{S_{ij}} = -kN(x_j - x_i)^2 \tag{3.23}$$

As stated by (3.23), $\dot{S_{ij}}$ is negative if $k > 0$. Assume that A is the largest invariant aggregate for $\dot{S_{ij}} = 0$ where it exists $x_j(t) - x_i(t) = 0$, $y_j(t) - y_i(t) = 0$, $\dot{x}_j(t) - \dot{x}_i(t) = 0$ and $\dot{y}_j(t) - \dot{y}_i(t) = 0$ of each oscillator.

All trajectories $\dot{x}_j(t) - \dot{x}_i(t)$ and $\dot{y}_j(t) - \dot{y}_i(t)$ are capable of converging to A when $t \to \infty$. This is based on the Lasalle's in-variance principle [85]. The connected oscillators synchronise asymptotically as a result.

2) **Damping Coefficient**: The oscillator's evolution time refers to t_{rise} when the unloaded inverter reaches its reference voltage. Assume that the voltage increases between $0.1V$ and $0.9V$ while the controller is operating in open circuit at $P = 0$. By multiplying the amplitude equation (3.17) by V in open loop, the following results are obtained:

$$\dot{V}V = \frac{V^{*2}\mu}{2}V^2 - \frac{\mu}{2}V^4 \tag{3.24}$$

In order to simplify (3.24), define $W = V^2$ and $W_{ref} = V^{*2}$, t_{rise} is from $0.1V^*$ to $0.9V^*$, and then there is:

$$dt = \frac{1}{\mu W(W_{ref} - W)}dW \tag{3.25}$$

By integrating (3.25) from $0.01W_{ref}$ to $0.81W_{ref}$, it yields:

$$t_{rise} = \frac{1}{\mu}\int_{0.01W_{ref}}^{0.81W_{ref}} \frac{1}{WW_{ref} - W^2}dW = \frac{6.045}{\mu W_{ref}} \tag{3.26}$$

As a result, the rising time for μ is written as:

$$t_{rise} = \frac{6.045}{\mu V^{*2}} \tag{3.27}$$

Note that the evolution time has an inverse relationship with the μ and V^*. Thus, the designer may achieve the required transitory time by choosing the proper damping coefficient and voltage reference.

3) **Current Coefficient** k: In order to identify the crucial conditions when k is changed from zero to a non-null value, Fig. 3.10 presents its bifurcation. It refers to the question that whether adjusting k will result in a dampening of the oscillation amplitude for the Hopf oscillator controller. As can be observed in Fig. 3.10, the limit cycle exhibits a sustained closed orbit across a wide range of k altering. When k changes from 0 to 7000 (the voltage reference is $325V$), the oscillator remains stable while maintaining the oscillations.

Therefore, the voltage equilibrium point of the system can be solved according to (3.17):

$$V^{*2}\mu V_e^2 - \mu V_e^4 - kP_e = 0 \tag{3.28}$$

where V_e and P_e stand for the steady-state equilibrium for the voltage amplitude and average active power, respectively. As a result, the positive roots of (3.29) can be written as follows:

$$\bar{V_e} = \sqrt{0.5\mu V^{*2} \pm 0.5\sqrt{\mu^2 V^4 - 8\mu k\overline{P_e}}} \tag{3.29}$$

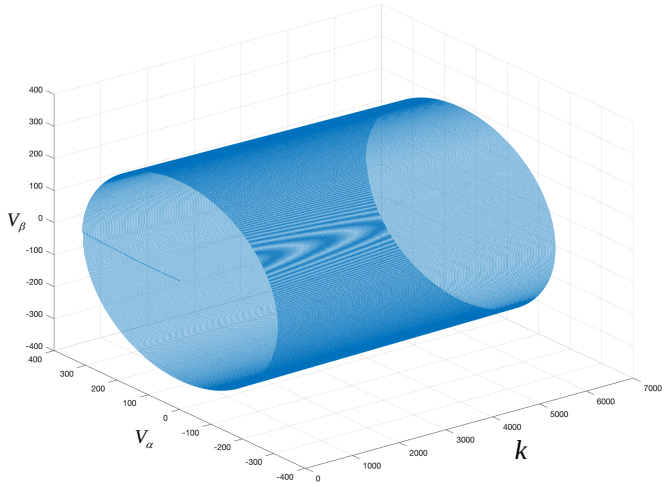

Fig. 3.10. Bifurcation diagram under k variation.

To obtain analytically the critical value of k_c, the two roots become real if the k satisfies:

$$0 < k \leq k_c = \frac{\mu V^{*4}}{8P_e} \tag{3.30}$$

According to (3.30), the critical value for k is inversely proportional to the equilibrium averaged real power and proportional to V^{*4}. As the rated power of the inverter, P_{rated}, is defined as the equilibrium active power for the purpose of parameter design, the critical value of k is provided by:

$$k_c = \frac{\mu V^{*4}}{8P_{rated}} \tag{3.31}$$

Additionally, assume that each inverter's filter impedance is the same in this situation, the synchronization of the inverters may be described as $v_i = v_j$ in steady state given the i and j index of the inverters. The ratio relationship between the power rating and k is given as follows by (3.17):

$$\frac{P_i}{P_j} = \frac{k_j}{k_i} \tag{3.32}$$

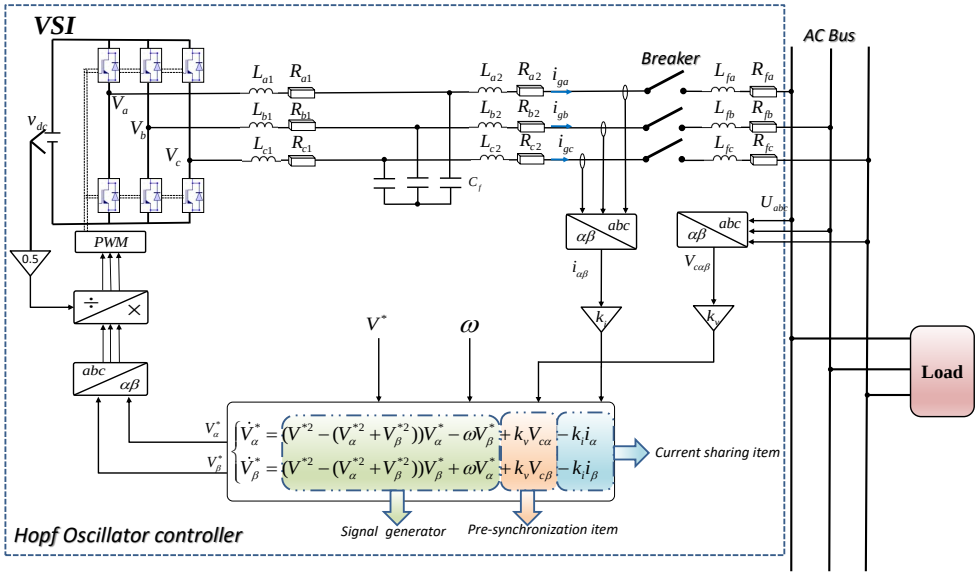

Fig. 3.11. Block diagram for the three-phase islanded VSIs.

3.2.2 Three-phase Controller Design

3.2.2.1 Control Implementation for the Three-phase Controller

As previously indicated, the Hopf oscillator has better dynamics than the Van der Pol oscillator and produces a circular limit cycle. Given that the voltage and current are three-phase, the controller should be created in a stationary reference frame to take use of the Hopf oscillator's inherent orthogonal output. As a result, the following equations are designed for three-phase system as:

$$\begin{cases} \dot{V_\alpha}^* = \mu(V^{*2} - V_\alpha^{*2} - V_\beta^{*2})V_\alpha^* - \omega {V_\beta}^* + k_v V_{c\alpha} - k_i i_\alpha \\ \dot{V_\beta}^* = \mu(V^{*2} - V_\alpha^{*2} - V_\beta^{*2})V_\beta^* + \omega {V_\alpha}^* + k_v V_{c\beta} - k_i i_\beta \end{cases} \tag{3.33}$$

where $i_{\alpha\beta}$ is the VSI output current in $\alpha\beta$-frame, $V^*_{\alpha\beta}$ is the voltage reference produced by the Hopf oscillator, and $V_{c\alpha\beta}$ is the measurement voltage component of the common bus. The voltage and current gain, respectively, are k_v and k_i. Thus, Fig. 3.11 can be used to illustrate the proposed controller block. The common bus voltage is measured in Fig. 3.11 and then transmitted in $\alpha\beta$-frame, which is employed to create the pre-synchronization components in the Hopf equations. On the other hand, the output current is advanced in the same manner to guarantee the VSIs' internal synchronization. The modulation signals are then obtained by scaling the voltage references produced by the Hopf equations by the DC-link voltage and transforming them from the $\alpha\beta$-frame to the abc-frame. The three components are described in more detail below:

1) **Hopf oscillator differential equation**: This is a main part for generating sinusoidal signals that will match the voltage and frequency references, which corresponds to the voltage reference blocks in the conventional droop controller. The bifurcations theory should be used to guarantee the orthogonal voltage references.

2) **Current sharing item**: Through this component, the coupled synchronization between oscillators is accomplished. The current sharing item creates the potential of synchronization across oscillator controllers since the current information can flow in both ways. In a nutshell, this component guarantees internal synchronization to enable current sharing, and k_i adjusts the output current to change the proportion of current sharing.

3) **Pre-synchronization item**: The inverter system will exhibit undesired overshoot dynamics when the inverters connect suddenly, which is because the different phase between inverters. So it is important to ensure pre-synchronization by adding the PLL into the droop controller as a conventional way. Additional PLL controllers, however, will reduce the control bandwidth and complicate system design. Through the nonlinear oscillator feature used in the proposed technique, the voltage pre-synchronization item is easily added to Hopf equations. Each VSI can synchronize with the AC bus prior to the breaker operation, which can allow the undesirable addition overshoot with the desired transients. Note that this item does not need to be switched, making it simple to manage in practice.

3.2.2.2 Averaged Model and Parameter Selection

The averaged model is a useful tool for studying the nonlinear system in steady state, as discussed in the single-phase system section. The ideal sinusoidal of an averaged model can approximately depict the real examples [56, 86, 87] since the actual oscillators have harmonic contents. Therefore, the following averaged model will be used to obtain the $P-V$ and $Q-\omega$ characteristics. The system is rebuilt in polar coordinates for the phase dynamics using the equation (3.1). The following results are obtained by varying $V_\alpha = Vsin(\theta)$ and $V_\beta = Vcos(\theta)$ with regard to time:

$$\begin{aligned} \dot{V_\alpha} &= sin(\theta)\dot{V} + Vcos(\theta)\dot{\theta} \\ \dot{V_\beta} &= cos(\theta)\dot{V} - Vsin(\theta)\dot{\theta} \end{aligned} \tag{3.34}$$

where the output of the inverter's instantaneous phase angle is θ. Assume that $V_{c\alpha}$ and $V_{c\beta}$ are approximately equal to V_α and V_β, respectively, when the filter and line impedance are both small. The following are the Hopf oscillator's phase dynamics equations when (4.5) is substituted for (3.33):

$$\begin{cases} \dot{V} = \mu(V^{*2}V - V^3) + k_v V - k_i(i_\alpha cos(\theta) + i_\beta sin(\theta)) \\ \dot{\theta} = \omega + \dfrac{k_i}{V}(i_\alpha sin(\theta) - i_\beta cos(\theta)) \end{cases} \tag{3.35}$$

According to (3.14) and (3.15), the three-phase dynamical system in 2π-periodic function are expressed as:

$$\begin{cases} \dot{\bar{V}} = \frac{\omega^*}{2\pi}\int_0^{\frac{2\pi}{\omega^*}} (\mu(V^{*2}V - V^3) + k_v V)dt \\ -\frac{\omega^* k_i}{2\pi}\int_0^{\frac{2\pi}{\omega^*}} i_\alpha cos(\omega^* t + \varphi^*) + i_\beta sin(\omega^* t + \varphi^*)dt \\ \dot{\bar{\varphi}}^* = \frac{\omega^* k_i}{2\pi \bar{V}}\int_0^{\frac{2\pi}{\omega^*}} i_\alpha(sin(\omega^* t + \varphi^*) - i_\beta cos(\omega^* t + \varphi^*))dt \end{cases} \tag{3.36}$$

The current feedback i_α, i_β is related to the instantaneous power P,Q, respectively. The average equations during2π-period of $\bar{P}$ and $\bar{Q}$ in $\alpha - \beta$ frame are given by:

$$\begin{cases} P(t) = \frac{3}{2}(V_\alpha i_\alpha + V_\beta i_\beta) \\ Q(t) = \frac{3}{2}(V_\beta i_\alpha - V_\alpha i_\beta) \end{cases}, \begin{cases} \bar{P} = \frac{\omega^*}{2\pi}\int_0^{2\pi/\omega^*} P(t)dt \\ \bar{Q} = \frac{\omega^*}{2\pi}\int_0^{2\pi/\omega^*} Q(t)dt \end{cases} \tag{3.37}$$

Substituting (3.37) to (3.36), (3.36) is rewritten as:

$$\begin{bmatrix} \dot{\bar{V}} \\ \dot{\bar{\varphi}}^* \end{bmatrix} = \begin{bmatrix} \mu V^{*2}\bar{V} - \mu\bar{V}^3 + k_v\bar{V} \\ 0 \end{bmatrix} + \frac{k\omega^*}{2\pi}\int_0^{2\pi/\omega^*} \begin{bmatrix} -\frac{2}{3\bar{V}}P \\ \frac{2}{3\bar{V}^2}Q \end{bmatrix} dt \tag{3.38}$$

Considering the averaged power equations (3.37), (3.38) can be simplified as:

$$\begin{bmatrix} \dot{\bar{V}} \\ \dot{\bar{\varphi}}^* \end{bmatrix} = \begin{bmatrix} \mu V^{*2}\bar{V} - \mu\bar{V}^3 + k_v\bar{V} \\ 0 \end{bmatrix} + \begin{bmatrix} -\frac{2k}{3\bar{V}}\bar{P} \\ \frac{2k}{3\bar{V}^2}\bar{Q} \end{bmatrix} \tag{3.39}$$

Finally, the amplitude and phase dynamics of one controller are derived as:

$$\begin{cases} \dot{\bar{V}} = V^{*2}\mu\bar{V} - \bar{V}^3\mu + k_v\bar{V} - \frac{2k_i}{3\bar{V}}\bar{P} \\ \dot{\bar{\theta}} = \omega^* - \omega + \frac{2k_i}{3\bar{V}^2}\bar{Q} \end{cases} \tag{3.40}$$

Therefore, the $P-V$ and $Q-\theta$ relationships are derived, which are similar as the characteristics of the droop controller. As opposed to the linear relationship of the conventional droop approach, the dynamics of amplitude and phase for the Hopf oscillator controller are nonlinear. However, the power measurement and LPF are not necessary for the oscillator controller's implementation. It's intriguing that the LPF for power in droop matches to the averaged model of differential equations.

Next, the design of scaling factor k_v and k_i are discussed based on the characteristic equations of (3.40), which can be rewritten as:

$$\begin{cases} V^{*2}\mu\bar{V}_{eq} - \bar{V}_{eq}^{\ 3}\mu + k_v\bar{V}_{eq} - \frac{2k_i}{3\bar{V}_{eq}}\bar{P}_{eq} = 0 \\ \omega^* + \frac{2k_i}{3\bar{V}_{eq}^2}\bar{Q}_{eq} = \omega_{eq} \end{cases} \tag{3.41}$$

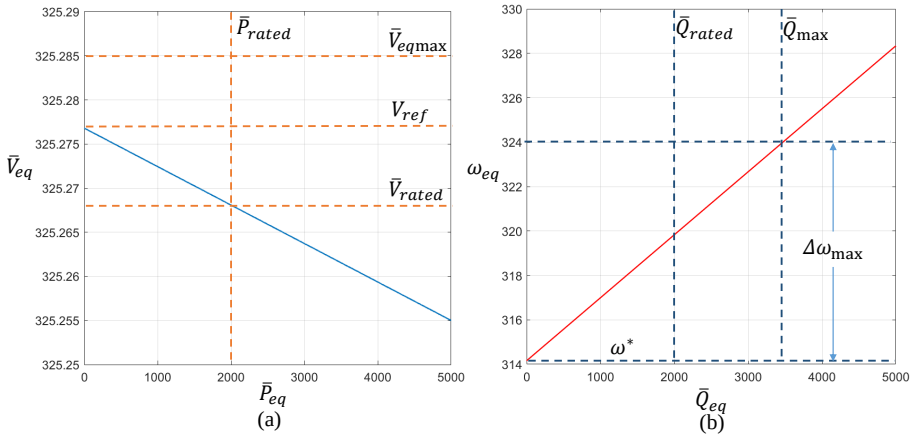

Fig. 3.12. The nonlinear droop characteristics for (a) $\bar{V}_{eq} - \bar{P}_{eq}$ (b) $\bar{\omega}_{eq} - \bar{Q}_{eq}$.

where the steady state equilibrium is denoted by the symbol subscript eq, the amplitude equation's positive roots in (3.41) are solved as follows:

$$\bar{V}_{eq} = \sqrt{0.5\mu(k_v{}^2 \pm \sqrt{(V^{*2}\mu + k_v)^2 - \frac{8}{3}\mu k_i \bar{P}_{eq}} + \mu V^{*2})} \tag{3.42}$$

In the open loop, the corresponding critical values $\bar{V}_{eqmin}$ and $\bar{V}_{eqmax}$ are:

$$\bar{V}_{eqmin} := 0 < \bar{V} < \bar{V}_{eqmax} := \sqrt{V^{*2} + \frac{k_v}{\mu}} \tag{3.43}$$

Subsequently, to make sure the roots of (3.41) are real, the critical value of $\bar{P}_{eqmax}$ satisfies:

$$0 < \bar{P} < \bar{P}_{eqmax} := \frac{3(k_v + \mu V^{*2})^2}{8\mu k_i} \tag{3.44}$$

Assume that $\bar{P}_{eqmax} = \bar{P}_{rated}$, where $\bar{P}_{rated}$ denotes the inverter's rated power. Otherwise, the inputs are provided as $\bar{Q}_{rated}$ and $\bar{V}_{rated}$. Define $\Delta\omega_{max}$ as the maximum frequency deviation, and the k_i operation range is valid in the following inequality:

$$k_i \leq \frac{3\Delta\omega_{max}\bar{V}_{rated}^2}{2\bar{Q}_{rated}} \tag{3.45}$$

Choose the k_i when the output current is 1A in order to standardize the parameters. This will result in a current gain of $\frac{\bar{P}_{rated}}{\bar{V}_{rated}}$. As a result, the maximum of k_v can be written as follows by (3.45) and (3.44):

$$k_v \leq \frac{2\Delta\omega_{max}\bar{V}_{rated}^2\sqrt{\mu\bar{V}_{rated}}}{\bar{Q}_{rated}} - \mu V^{*2} \tag{3.46}$$

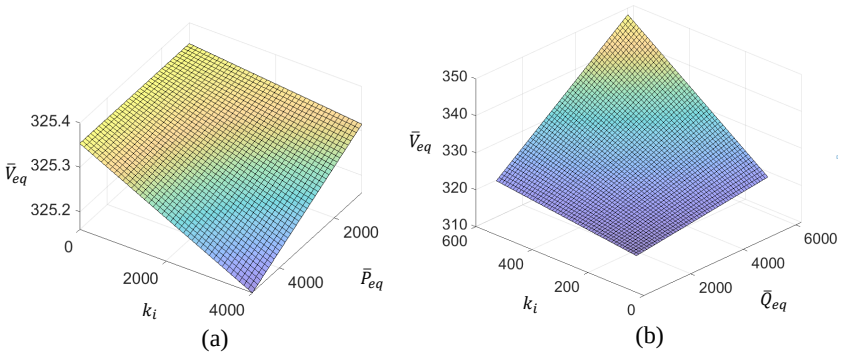

Fig. 3.13. (a) Diagram of k_i, $\bar{V}_{eq}$ and $\bar{P}_{eq}$. (b) Diagram of k_i, $\bar{V}_{eq}$ and $\bar{Q}_{eq}$.

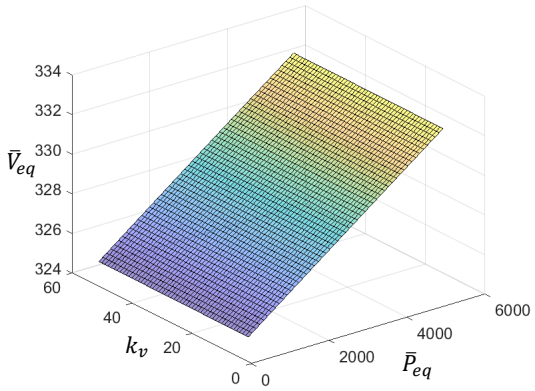

Fig. 3.14. Diagram of k_v, $\bar{V}_{eq}$ and $\bar{P}_{eq}$.

Figure 3.12 presents the droop and ascend characteristics curves according to (3.41) and (3.42), where the operation's parameters are: $k_v = 5$, $\mu = 1$, $k_i = 1000$, and $V^* = 325V$. When the active power varies, a droop law that is similar to typical droop curve between equilibrium voltage and equilibrium active power.

An ascend law govern the connection between the frequency and equilibrium reactive power, which implies that as reactive power rises, the equilibrium frequency in time domain climbs to infinity as shown in Fig. 3.12(b). Therefore, the frequency fluctuation should be controlled by the maximum frequency offset. Furthermore, Fig. 3.13(a)(b) show how the voltage changes depending on the variables k_i and $\bar{P}_{eq}$, k_i and $\bar{Q}_{eq}$. The slopes of the droop and ascend laws for the Hopf-oscillator controller are influenced by k_i. Furthermore, changing k_v only affects the pre-synchronization speed and voltage equilibrium's critical value, instead of the voltage amplitude as shown in Fig. 3.14.

3.3 Stability Analysis Based on Small Signal Model

3.3.1 Single Phase System

In order to analyze the stability of the inverter model, a Hopf oscillator controlled inverter connected to the common bus with L filter is built. To derive the state-space model expediently, the instantaneous output voltage and current of inverter are transferred into v_{od}, v_{oq} and i_{od}, i_{oq}, respectively. Therefore, the instantaneous active and reactive power components are:

$$\begin{aligned} \widetilde{P} &= v_{od} i_{od} + v_{oq} i_{oq} \\ \widetilde{Q} &= v_{od} i_{oq} - v_{oq} i_{od} \end{aligned} \tag{3.47}$$

The instantaneous power with $\phi = \pi/2$ can be simplified as:

$$\begin{aligned} \bar{P} &= V \cdot i_{od} \\ \bar{Q} &= -V \cdot i_{oq} \end{aligned} \tag{3.48}$$

The state equations of system with L filter can be expressed as [18, 88]:

$$\begin{aligned} \frac{di_{od}}{dt} &= \frac{-R_f}{L_f} i_{od} + \omega i_{oq} + \frac{1}{L_f} v_{od} - \frac{1}{L_f} v_{bd} \\ \frac{di_{oq}}{dt} &= \frac{-R_f}{L_f} i_{oq} - \omega i_{od} + \frac{1}{L_f} v_{oq} - \frac{1}{L_f} v_{bq} \end{aligned} \tag{3.49}$$

where v_{bd} and v_{bq} are the d and q components of the common bus voltage, and R_f and L_f are the resistance and inductance of the filter. By using the usual approximations $\sin\theta \approx \theta$, while $\phi = \pi/2$, the variation of amplitude and phase in small signal model can be obtained:

$$\begin{aligned} v_{od} - v_{bd} &= \Delta V \\ v_{oq} - v_{bq} &= V_b \Delta\theta \end{aligned} \tag{3.50}$$

where V_b is the amplitude of the common bus voltage.

In order to build the state-space model, define $\Delta\omega_b$ as an input disturbance due to the frequency variation occurs when there is a load step change or inverters addition and removal. According to (3.17), (3.49) and (3.50), the linearized small-signal state-space model at the given operating point is given by:

$$\begin{bmatrix} \Delta\dot{\theta} \\ \Delta\dot{V} \\ \Delta\dot{i}_d \\ \Delta\dot{i}_q \end{bmatrix} = A \begin{bmatrix} \Delta\theta \\ \Delta V \\ \Delta i_d \\ \Delta i_q \end{bmatrix} + B\Delta\omega_b \tag{3.51}$$

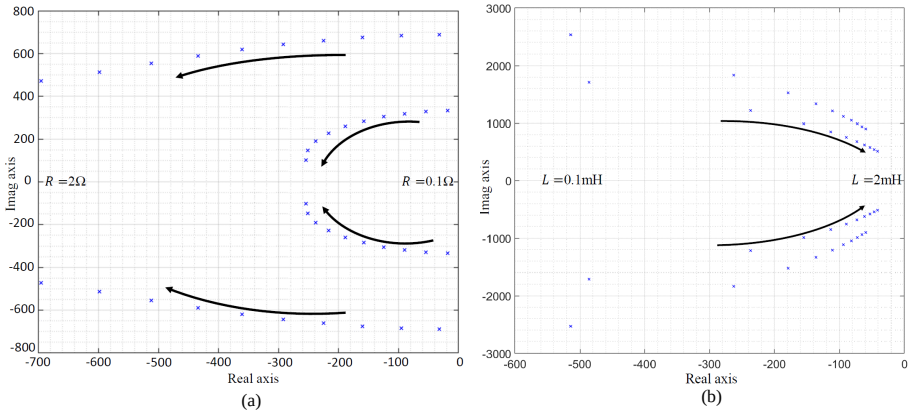

Fig. 3.15. Root locus for (a) $k = 650, L_f = 2mH$ and $R_f = 0.1 \rightarrow 2\Omega$. (b) $R_f = 1\Omega$, $k = 650$ and $L_f = 0.1 \rightarrow 2mH$.

where

$$A = \begin{bmatrix} 0 & 0 & 0 & \frac{k}{2V} \\ 0 & 0.5\mu(r^2 - V^2) & -k & 0 \\ 0 & \frac{1}{L_f} & \frac{-R_f}{L_f} & \omega^* \\ \frac{V_b}{L_f} & 0 & -\omega^* & \frac{-R_f}{L_f} \end{bmatrix}$$

$$B = \begin{bmatrix} -1 & 0 & 0 & 0 \end{bmatrix}^T$$

Note that the state-space model of Hopf oscillator controlled inverter is the forth-order system. Assume that the output voltage of inverter is equal to reference $V \approx r$ at the equilibrium point, the characteristic equation of (3.51) can be derived as [89]:

$$s^4 + as^3 + bs^2 + cs + d = 0 \tag{3.52}$$

where

$$a = \frac{2R_f}{L_f}$$

$$b = \frac{1}{2VL_f^2}(2VR_f^2 + 2VL_f^2\omega^2 + 2kVL_f + kL_fV_b)$$

$$c = \frac{1}{2VL_f^2}(2kVR_f + kV_bR_f)$$

$$d = \frac{k^2V_b}{2VL_f^2}$$

According to Fig. 3.15 (a) , the filter resistance has little impact on dynamic performance as R_f increases, the eigenvalues steadily move away from the real

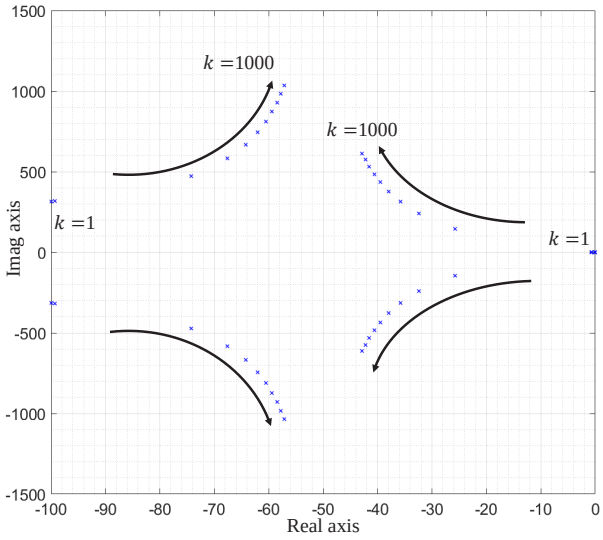

Fig. 3.16. Root locus for $R_f = 1\Omega$, $L_f = 2mH$ and $k = 1 \rightarrow 1000$.

part. According to Fig. 3.15(b), as L_f increases, the poles migrate closer to the real axis more quickly, which makes the system more sensitive.

It is obvious that the dominant eigenvalues of (3.52) reveal the stability of systems. Set $V_b = V = 178V$ and $\omega = 100\pi$ as operating conditions, and observe how parameters k,R_f and L_f affect on stability. Fig. 3.16 depicts the root-locus diagrams for different values of k. It indicates that the system remains stable with large range of k, the eigenvalues converge to negative real part -50 as k increases which makes system more damped, and the two pairs poles converge to real part 0 which is sensitive to the state variables as k decreases. Note that the oscillator controller approximates open loop system when $k \rightarrow 0$ which decreases the damping ratio. Remarkably, the large k gain ensures the fast transient response of controller, whereas the larger k certainly achieve obvious overshoot in dynamics. Therefore, choosing k not only stays farther away from imaginary but also achieves good attenuation.

In conclusion, the desired dynamic response can be obtained by adjusting the parameters k, L_f and R_f. In particular, optimizing k greatly improves the dynamic performance.

3.3.2 Three-Phase System

To achieve a precise time-domain matching between the steady-state model and simulation, a small signal model is built based on Fig. 2.6. Define the VSI's output current and voltage amplitude in the rotating frame as V_{1dq}, i_{1dq}, V_{2dq}, and i_{2dq}. Set the VSI 1 voltage as the reference, resulting in $V_{1d} = V_1$, $V_{1q} = 0$ and $V_2 = \sqrt{{V_{2d}}^2 + {V_{2q}}^2}$. Thus, the VSI #1 and #2 output active and reactive

powers are stated as:

$$\begin{aligned} P_1 &= \frac{3}{2}V_{1d}i_{1d}, P_2 = \frac{3}{2}(V_{2d}i_{2d} + V_{2q}i_{2q}) \\ Q_1 &= -\frac{3}{2}V_{1d}i_{1q}, Q_2 = \frac{3}{2}(V_{2q}i_{2d} - V_{2d}i_{2q}) \end{aligned} \tag{3.53}$$

Rewrite (3.40) in steady state while taking into account the line impedance as follows:

$$\begin{cases} \dot{V_1} = f_1 = V^{*2}\mu V_c - {V_1}^3\mu + k_v V_1 - \dfrac{2k_i}{3V_1}P_1 \\ \dot{V_2} = f_2 = V^{*2}\mu V_c - {V_2}^3\mu + k_v V_2 - \dfrac{2k_i}{3V_2}P_2 \\ \dot{\theta_1} = \omega^* + \dfrac{2k_i}{3{V_1}^2}Q_1 \\ \dot{\theta_2} = \omega^* + \dfrac{2k_i}{3{V_2}^2}Q_2 \end{cases} \tag{3.54}$$

According to (3.49), the equations regarding the line impedance are expressed as:

$$\begin{aligned} \frac{di_{1d}}{dt} &= f_3 = \frac{-R_{l1}}{L_{l1}}i_{1d} + \dot{\theta_1}i_{1q} + \frac{1}{L_{l1}}v_{1d} - \frac{1}{L_{l1}}v_{cd} \\ \frac{di_{2d}}{dt} &= f_4 = \frac{-R_{l2}}{L_{l2}}i_{2d} + \dot{\theta_2}i_{2q} + \frac{1}{L_{l2}}v_{2d} - \frac{1}{L_{l2}}v_{cq} \\ \frac{di_{1q}}{dt} &= f_5 = \frac{-R_{l1}}{L_{l1}}i_{1q} - \dot{\theta_1}i_{1d} + \frac{1}{L_{l1}}v_{1q} - \frac{1}{L_{l1}}v_{cq} \\ \frac{di_{2q}}{dt} &= f_6 = \frac{-R_{l2}}{L_{l2}}i_{2q} - \dot{\theta_2}i_{2d} + \frac{1}{L_{l2}}v_{2q} - \frac{1}{L_{l2}}v_{cq} \end{aligned} \tag{3.55}$$

where v_{cd} and v_{cq} is the d and q voltage component of the AC bus.

As seen in (3.40), the phase rises indefinitely. Hence, the frequency error is defined as:

$$\Delta\dot{\theta} = f_7 = \dot{\theta}_1 - \dot{\theta}_2 = \frac{2k_i}{3}(\frac{Q_1}{{V_1}^2} - \frac{Q_2}{{V_2}^2}) \tag{3.56}$$

Select $\Delta X = [\Delta V_1 \quad \Delta V_2 \quad \Delta\theta \quad \Delta i_{1d} \quad \Delta i_{1q} \quad \Delta i_{2d} \quad \Delta i_{2q}]^T$ as the state vector, and $f = [f_1 \quad f_2 \quad f_3 \quad f_4 \quad f_5 \quad f_6 \quad f_7]^T$. According to (3.54), (3.55) and (3.56), the small-signal model is given by:

$$\dot{\Delta}X = \mathbf{A}\Delta X \tag{3.57}$$

where $\mathbf{A} = \dfrac{\partial f}{\partial x^T}$. It is obvious that A is a square matrix of size 7×7 with time-invariant matrices. Therefore, the state matrix A's eigenvalues [90, 91] are derived by:

$$det(s\mathbf{I} - \mathbf{A}) = 0 \tag{3.58}$$

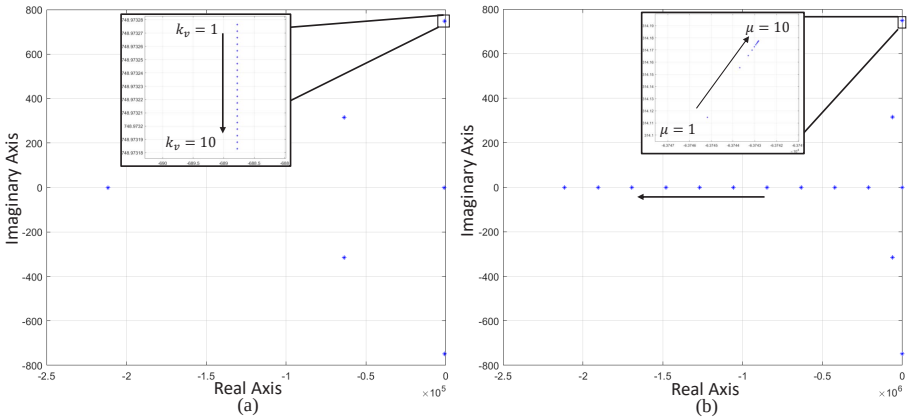

Fig. 3.17. Root locus for (a) $1 \leq k_v \leq 10$ (b) $1 \leq \mu \leq 10$.

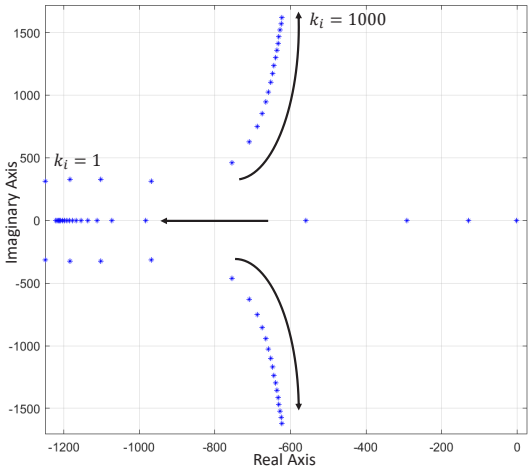

Fig. 3.18. Root locus for $1 \leq k_i \leq 1000$.

Discussions of the effects of the parameters k_v, μ, k_i, and line impedance are as follows. Be aware that the small-signal model provides a global diagram for the eigenvalues responses.

The eigenvalue clusters for both k_v and μ locate at the left-half in the s-plane as seen in Fig. 3.17. The poles move slightly when k_v and μ are raised, indicating that the parameters are unaffected by the stability of system. Fig. 3.18 demonstrates how k_i is sensitive to the stability. The transient response of the VSI is significantly influenced by k_i and as k_i rises, the damping decreases.

In terms of the line impedance parameters, R_l and L_l, the trajectory of the eigenvalues is shown in Fig. 3.19. It is obvious that a family of poles have gathered close to the unstable area. Additionally, when R_l increases, the eigenvalues become more responsive to the controller states. However, when

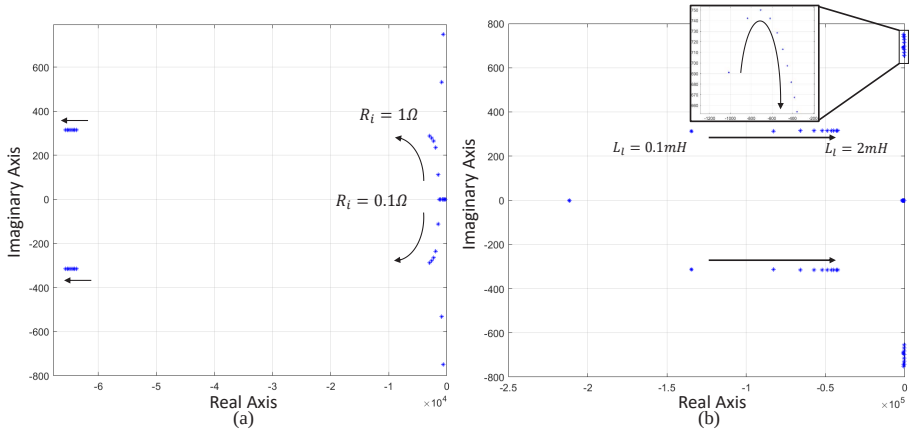

Fig. 3.19. Root locus for (a) $0.1\Omega \leq R_i \leq 1\Omega$ (b) $0.1mH \leq L_l \leq 1mH$.

Table 3.1: System parameters in simulation and experiment.

Parameter	Value	Unit
DC voltage	450	V
Rated Power	2.2	kW
Filter inductance	1.8	mH
Filter capacitance	25	μF
Resistive load	180	Ω
Step-up load	180	Ω
Oscillator initial state	155,0	V,V
Startup k	600	A/A
Damping Coefficient μ	5	$V^{-2}s^{-1}$
Voltage reference	311	V
Frequency reference	50	Hz

L_l increases, the eigenvalues shift toward the unstable area and the system's damping becomes even smaller. Therefore, k_i is the most important parameter that affects the dynamics of the system.

3.4 Simulation and Experiment Results

3.4.1 Single Phase System

3.4.1.1 Simulation Results

The performance of the proposed controller has been validated by comparison with VOC [56]. Two parallel inverters based on two different oscillator types have been simulated. The system parameters are chosen from Table 3.1. Numerous tests have been performed, including the inverter starting, the inverter connection, changing of the current ratio and a significant variation in load power.

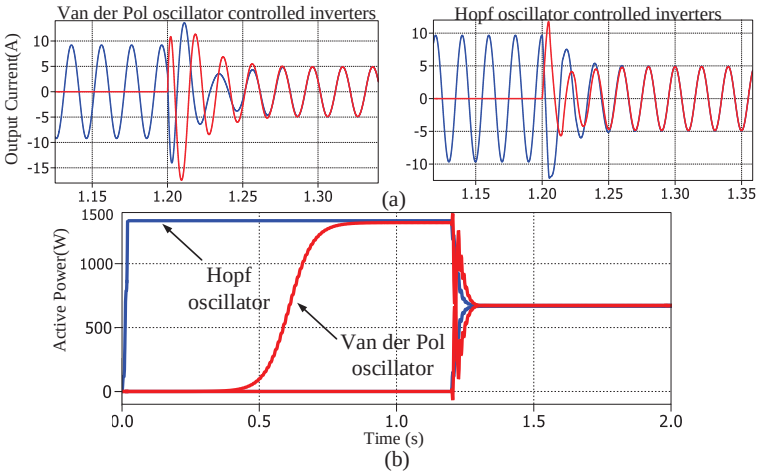

Fig. 3.20. Dynamic response of current and active power under startup and connection.

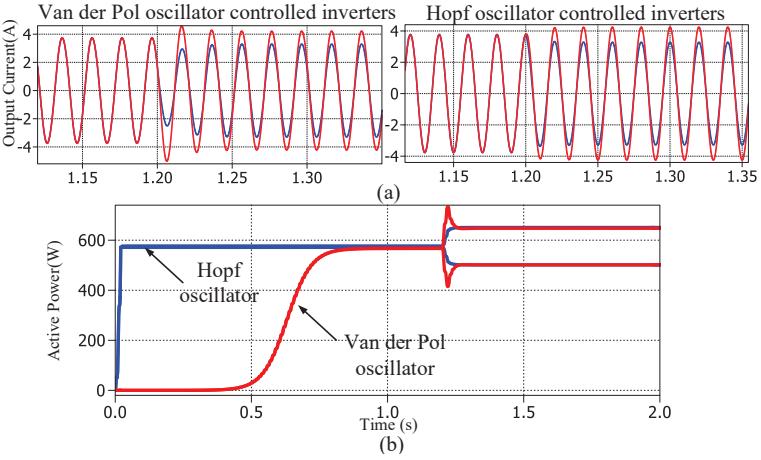

Fig. 3.21. Dynamic response of current and active power when current ratio varies.

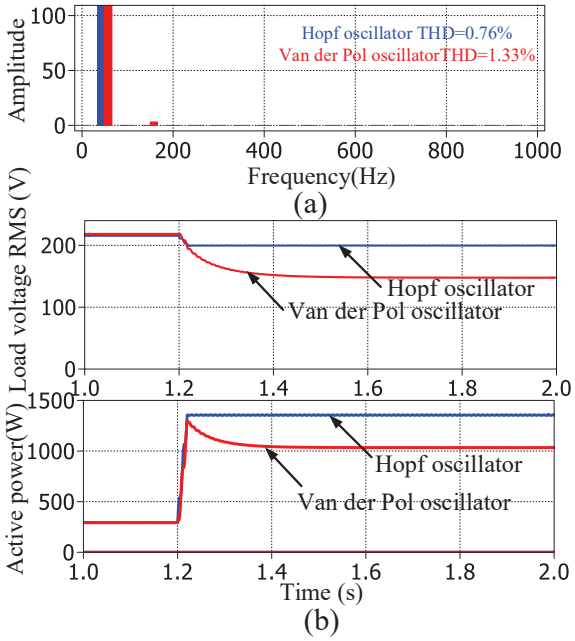

Fig. 3.22. Comparison results of (a) voltage THD of unloaded inverter and (b) the large variation of load power.

1) **Startup and Connection.** As VSI #1 startup and VSI #2 connection to supply a resistive load, Fig. 3.20 illustrates the transient response of output current and active power. The Van der Pol oscillator controller starts up in about 0.8 seconds, then settles down in 0.1 seconds when VSI #2 connects. Notice that $3V$ starting condition for Van der Pol oscillators is chosen with consideration given to the errors produced during the simulation. In contrast, the Hopf oscillator controller starts up at around 0.02s under $3V$ starting conditions. The clear discrepancy is due to the fact that the evolution time of Van der Pol($t_{rise} = \dfrac{6}{\omega^* \varepsilon \sigma}$) is less than the evolution time [56]. The proposed controller can implement power sharing, and the connection settling time is around 0.06s. It is obvious that the Hopf oscillator achieves steady state faster than the Van der Pol during starting and connection.

2)**Ratio Changes.** Fig. 3.21(a) shows the transient response for rapid direct currents ratio changes of parallel VSIs with two control techniques. The current ratio has changed from 1:1 to 1:2 since 1.2s. The current outputs of two control systems are almost instantaneous in Fig. 3.21(b). Note that the Hopf oscillator controller's power transient lasts 0.04s while the Van der Pol lasts 0.045s. However, there is no overshoot in dynamics for Hopf controller.

3) **Unload Voltage THD and Large Load Power Variation.** The output voltage harmonic content of the unload inverter is initially shown in Fig. 3.22(a). Hopf and Van der Pol controllers have THD of 0.76 and 1.33

percent, respectively. The terminal voltage from the Van der Pol controller has a small number of third-order harmonics, which accords with the harmonics analysis in Section 3.2.1. In the load power variation example, the oscillator-controlled inverter first provides a steady-state power of $P_0 = 280W$ to the resistive load before switching to a large load power of $P_1 = 5P_0 = 1.4kW$ at 1.2s. Figure 3.22(b) compares the transients of load voltage RMS and active power. The load voltage of the proposed method decreases by just 9% of the rated voltage compared to a 32% decline for the Van der Pol. According to the large load power variance, the proposed controller performs better.

3.4.1.2 Experimental Results

Three parallel single-phase inverters system are built to validate the effectiveness of the proposed controller. Three Danfoss inverters with LCL filters, two linear loads, a nonlinear load, and a source of DC voltage supply are all included in the prototype. The dSPACE DS1006 real-time platform is used for controller with 0.1ms sampling time [92, 93]. Each inverter runs at a switching frequency of 10kHz.

1) **Inverters Connection.** The three inverters are connected in parallel to share a single resistive load in the first case. In this case the oscillator initial state is set as the same for inverter #2 and #1 with ($0.5V_{rated}$,0), and for inverter #3 is set to ($0.9V_{rated}$,0), in order to observe the connection performance with different initial states. The active and reactive powers, inverter current, and load voltage transient response are shown in Fig. 3.23(a)-(d). In Fig. 3.23(a), the first and second connections' settling times are around 0.6 seconds and 0.65 seconds, respectively. Inverter 3's varied initial state caused a little overshoot in the second connection. Hence, it is best to use the same initial state for all inverters to reduce unnecessary overshoot throughout the controller design process. In addition, the current transient in Fig. 3.23(c) also exhibits the rise-reduce dynamics with various beginning states to influence the connection speed.

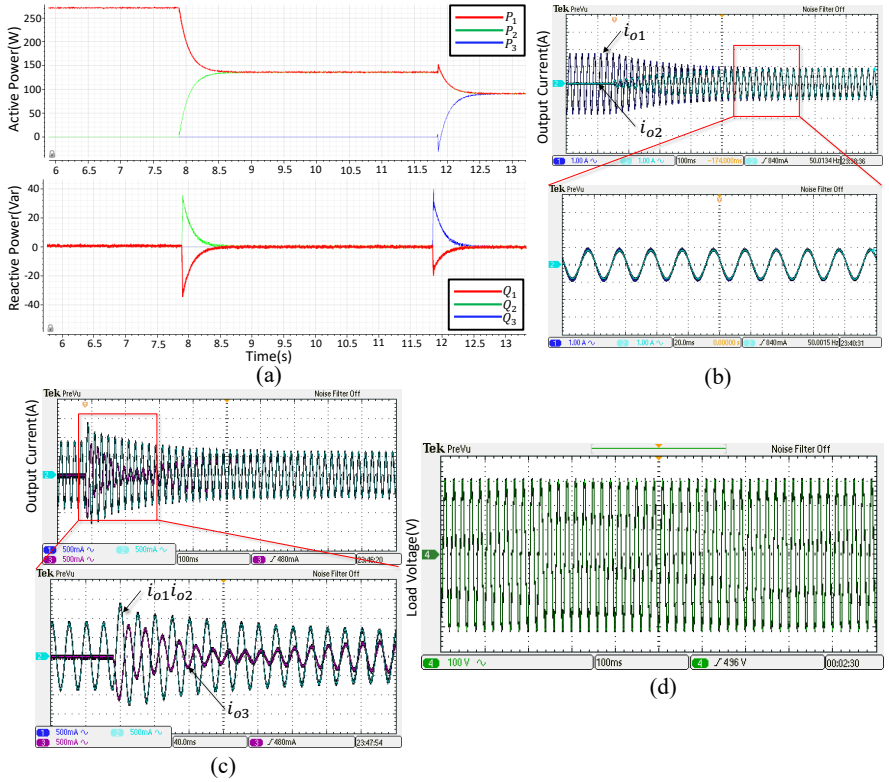

Fig. 3.23. Experimental results of VSIs connection one by one. (a) Active and reactive powers. (b) Output current of VSI #1 and #2. (c) Output current of VSI #1,#2 and #3. (d) Load voltage.

2) **Ratio Changes.** The next scenario is for a sudden change of current ratio that goes 1:1:1 to 1:1:2, as depicted in Fig. 3.24(a)-(c). The PQ dynamics under ratio variations are shown in Fig. 3.24(a). It can be seen that the output power in inverter #3 almost doubles its value while the #1 and #2 inverters decrease the active power injection in proportion to 2 compared to the initial value. Also, a mall transient of reactive power before it returns to 0 and the transient response only lasts 0.18 seconds. As seen in Fig. 3.24(b), the output current of the inverter #3 increases immediately as the sharing ratio k changes, and the load voltage remains constant as the ratio changes in Fig. 3.24(c).

3) **Nonlinear load.** A rectifier nonlinear load (45% of current THD) is supplied and one inverter is removed from the parallel system. The PQ dynamics as the VSI #2 is suddenly removed from the parallel connection as shown in Fig. 3.25(a). Due to a sudden removal, it appears an undershoot of reactive power. The VSI #2 current abruptly decreases while the VSI #1 and #3 currents grow to supply the load steadily, as seen in Fig. 3.25(b). The waveforms of the load voltage remain constant with a little amount of distortion as illustrated in

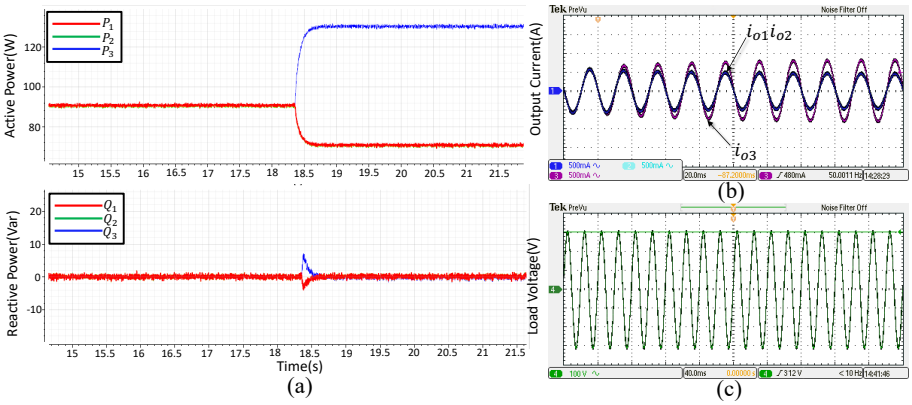

Fig. 3.24. Experimental results of ratio changes from 1:1:1 to 1:1:2. (a) Active and reactive powers. (b) Output current of VSI #1, #2 and #3. (c) Load voltage.

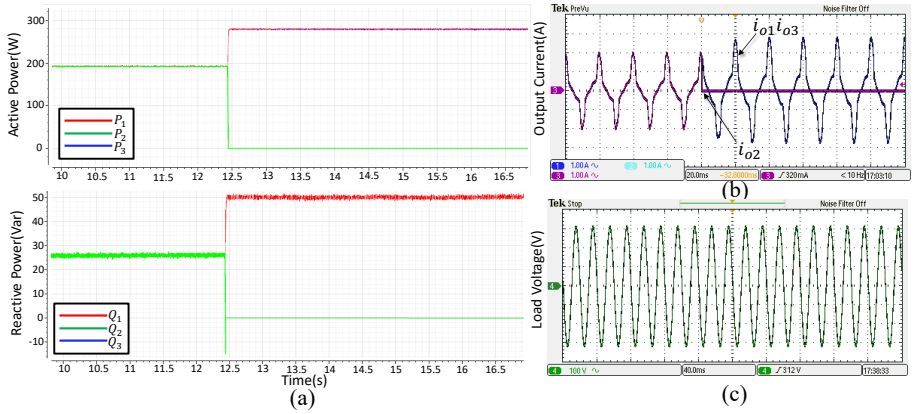

Fig. 3.25. Experimental results of VSI removal with supplying nonlinear load. (a) Active and reactive powers. (b) Output current of VSI #1, #2 and #3. (c) Load voltage.

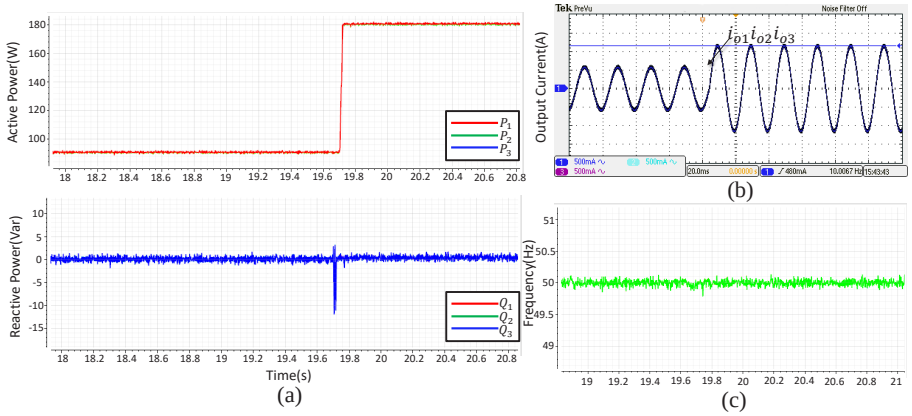

Fig. 3.26. Experimental results of the resistive load step. (a) Active and reactive powers. (b) Output current of VSI #1, #2 and #3. (c) Load voltage frequency.

Fig. 3.25(c).

4) **Load step.** In Fig. 3.26(a)-(c), an additional 180Ω resistive load is connected into the common bus after the three inverters that are set to run with the same current ratio. As illustrated in Fig. 3.26(b), it is clear that the current increases promptly to be able to supply the common loads, and suitable supply to the common and verified transient is negligible. The frequency response to a load step is shown in Fig. 3.26(c), which demonstrates that the frequency variations are minimal and remains within the allowable range, e.g. ±0.5Hz.

As conclusion, accordingly to the experimental results the proposed controller can implement proper synchronization in parallel inverters applications. The proposed approach responds quickly to changes in the sharing ratio disregarding if there is a resistive load, or a nonlinear load, as well as when one of the three inverters is connected and removed.

3.4.2 Three Phase System

3.4.2.1 Simulation Results

In order to compare with the droop and VOC methods, the performance of the proposed technique is first validated using simulation. The system parameters are listed in Table 3.2. For comparison, the droop coefficients are set to $m = 0.00001, n = 0.0002$, and the settings for VOC are taken from [55]. It can be seen that some simulation cases were done, such as the inverter starting, the connection, the current ratio changes and the nonlinear loads.

Table 3.2: Three-phase inverter parameters used in simulation and experimental.

Parameter	Value	Unit
DC voltage	500	V
Rated Power	2.2	kW
Filter inductance	1.8	mH
Filter capacitance	25	μF
Resistive load	100	Ω
Step-up load	100	Ω
Oscillator initial state	155,0	V,V
Startup k_i	300	A/A
Startup k_v	10	V/V
Damping Coefficient μ	1	$V^{-2}s^{-1}$
Voltage reference	325	V
Frequency reference	50	Hz

1) **Connection and removal of a VSI.** When VSI #1 starts and VSI #2 is connected and unplugged when a resistive load of 100Ω is present, the output current and active power's transient reaction is seen in Fig. 3.27. As observed in Fig. 3.27(a), the Van der Pol controller has a starting time of around 0.5s and a settling time of 0.18s when the VSI #2 connects. Notice that a $3V$ initial condition for the Van der Pol oscillators has been chosen with consideration due to the simulating errors. However, the settling time at 0.75s is substantially longer than VOC. In Fig. 3.27(c), take note of how the frequency deviation is substantially higher with an error of 0.06Hz. As shown in Fig. 3.27(b), the Hopf oscillator controller starts up in around 0.02s at $(0V, 0V)$ starting condition. The Hopf controller can achieve a power sharing, and the connection settling time is around 0.11s. It is obvious that during the startup, connection and removal of VSI, the Hopf oscillator achieves the steady-state faster than the other two approaches.

2) **Ratio changes.** Figure 3.28 illustrates the transient response for a sudden direct current ratio changes of the parallel VSIs considering the three different control schemes. In this case the current ratio has changed from 1:1 to 2:1, and the current outputs of the three control systems are almost immediate. Notice that the Hopf oscillator controller's transient response lasts about 0.15s while it lasts 0.21s for the Van der Pol and 0.18s for the droop method. It is noteworthy that the phase error emerges as a result of the $Q - \omega$ characteristics changing in Fig. 3.28(b). Additionally, as illustrated in Fig. 3.28(a), a slight active power overshoot occurs in the waveform of the Van der Pol oscillator.

3) **Load steps.** Figure 3.29 shows how the system reacts to a step changes in the load. The resistive load changes from 100Ω to 200Ω at 0.6s. A resistive load in the three-phase diode bridge rectifier ($200\Omega + 100\mu$F) is switched at 1.2s. The load currents of three oscillator controllers suddenly grow while the load voltage continues meeting specifications. When the nonlinear load is connected, note that there is an overshoot from the oscillator controllers due to a spike in the voltage on the filter capacitor. The power factor remains at the same

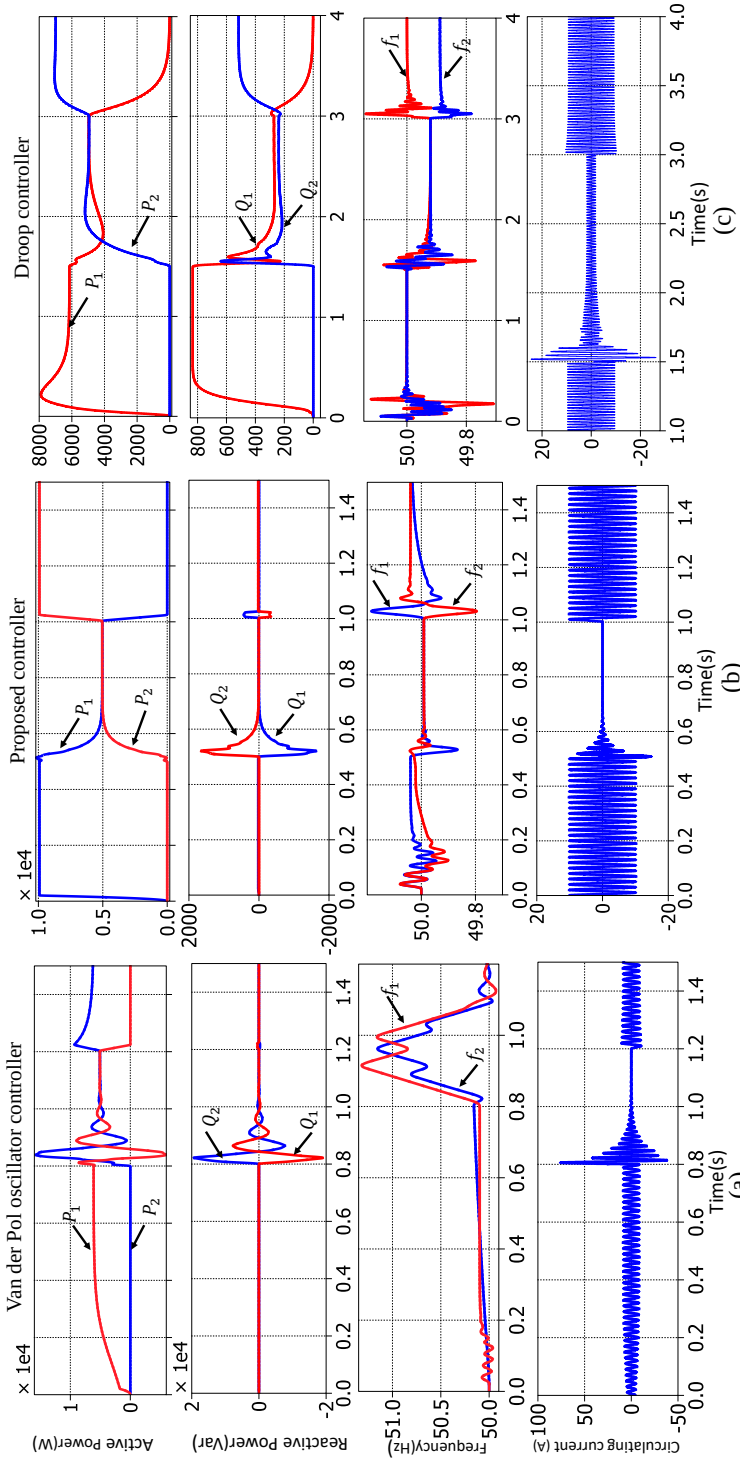

Fig. 3.27. Simulation results of the three methods while adding or removing a three-phase VSI.

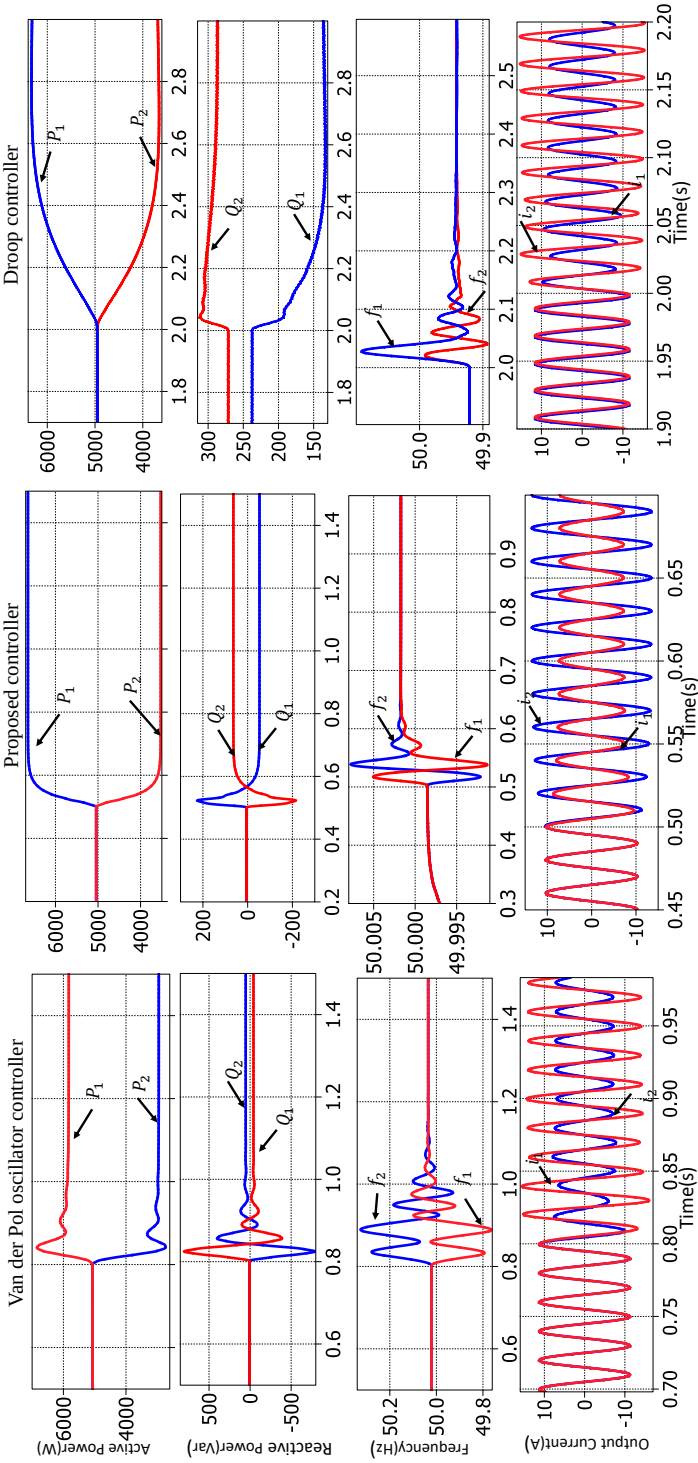

Fig. 3.28. Simulation results of the three methods under a current ratio varying from 1:1 to 2:1.

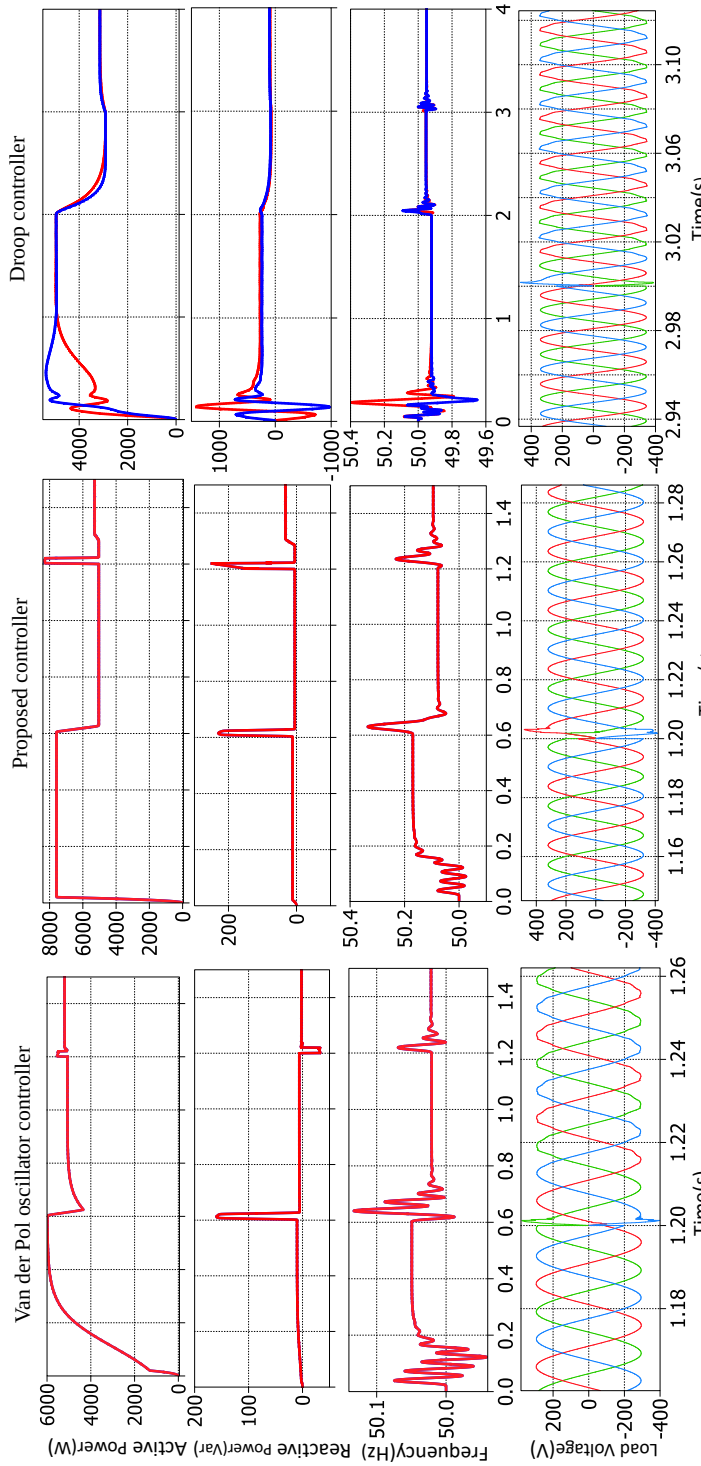

Fig. 3.29. Simulation results of the three methods under linear and nonlinear loads step change.

value after 1.2s. The measured load voltage THD at this time for the Van der Pol, Hopf, and droop each are 2.767%, 2.262% and 3.142%. In the presence of a nonlinear load, the Van der Pol and Hopf approaches are thereby shown to be more reliable than the droop controller and the Hopf method yields a better power quality.

3.4.2.2 Experimental Results

Experimental results of the proposed method has been carried out for two three-phase VSIs with a LCL filter connected in parallel. The setup and controller parameters are also listed in Table 3.2.

1) **VSI connection.** The transient response of the load voltage, output current and instantaneous active and reactive powers with an instant VSI #2 connection is shown in Fig. 3.30(a)-(c). The settling time is substantially shorter than simulation around 0.06s, since the actual switching frequency is larger than the sampling frequency. In addition, the load voltage remains steady while the current transient exhibits the characteristics of an abrupt synchronization as shown in Fig. 3.30(b)(c).

2) **Ratio changes.** Figure 3.31(a)-(c) shows the transient response to variations in k_i from 1:1 to 4:3. The output currents of the VSIs are practically immediately matched to the desired ratio and the load voltage remains regulated.

3) **Load steps.** When the VSIs are used to feed loads with resistive characteristics, the transient response will be given as shown in Fig. 3.32(a)-(c). A 100Ω resistive load is switched on and off in the interval between 4s and 12s, respectively. In Fig. 3.32(b), it can be seen that an instantaneously dynamic behaviour for the output current rise and fall. Note that the load voltage exhibits an evident transient and fast recovery to the references. Next, a high load step change is conducted. And, to check the over-current protection of the inverters, a double load power change is applied. In the experimental configuration, two paralleled VSIs supply a common resistive load with P_1, and then switches to $P_2 = 2P_1$ and after switches back to P_1. Figure 3.33 shows the experimental results with respect to power, load current and voltage. From Fig. 3.33(c), it can be seen that the double increase or decrease of the load power step has a minimum influence on the load voltage. Thus, the experiment results show the effectiveness of the proposed controller for a wide load power variation.

As conclusions, the experimental results show that the proposed three-phase Hopf oscillator controller is capable of realizing a pre-synchronization and proper current sharing in the operation of a decentralized system. Furthermore, there is a rapid dynamic reaction time and stable operation with the load step change.

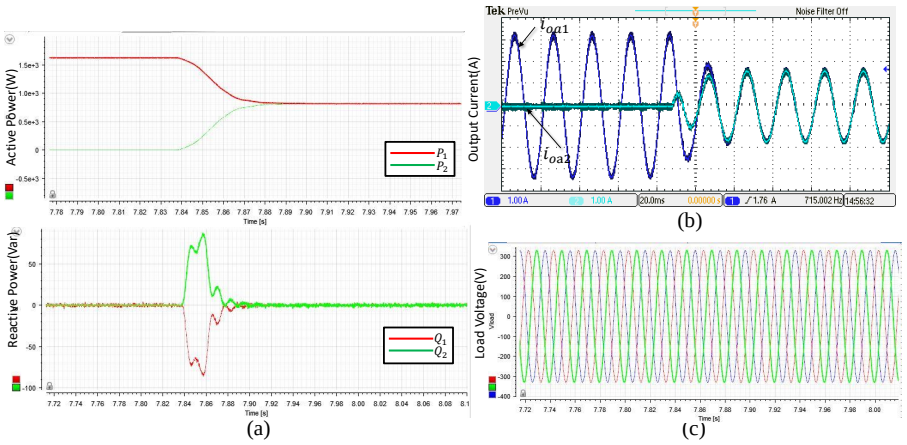

Fig. 3.30. Experimental results of the inverter connection. (a) Active and reactive powers. (b) Output current of VSI #1 and #2. (c) Load voltage.

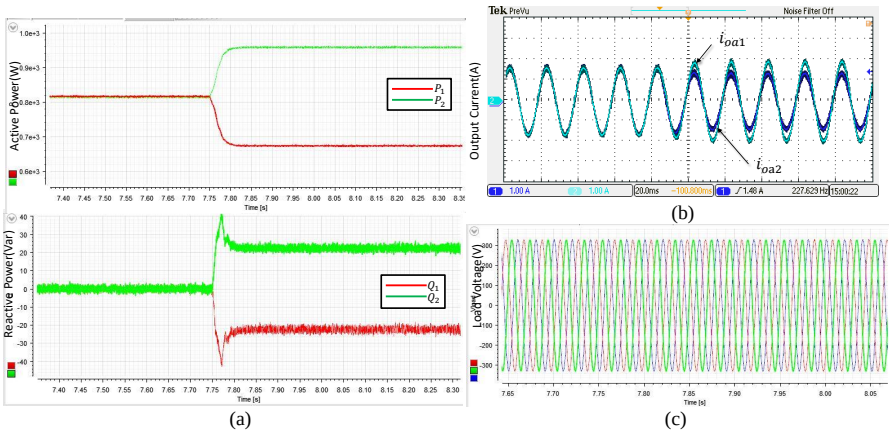

Fig. 3.31. Experimental results of the ratio changes from 1:1 to 4:3. (a) Active and reactive powers. (b) Output current of VSI #1 and #2. (c) Load voltages.

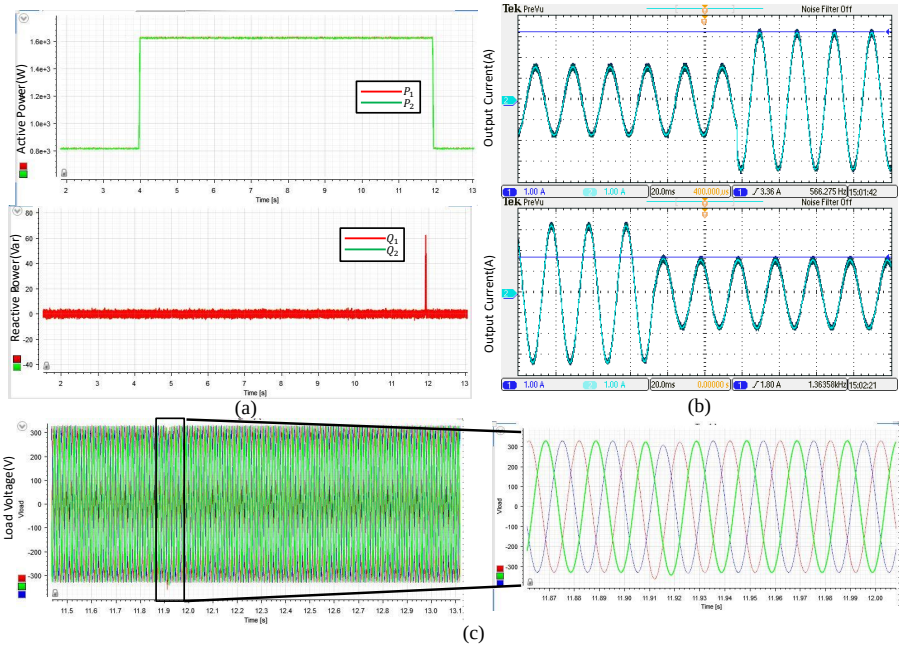

Fig. 3.32. Experimental results for the load step and inverter disconnection. (a) Active and reactive powers. (b) Output current of VSI #1 and #2. (c) Load voltages.

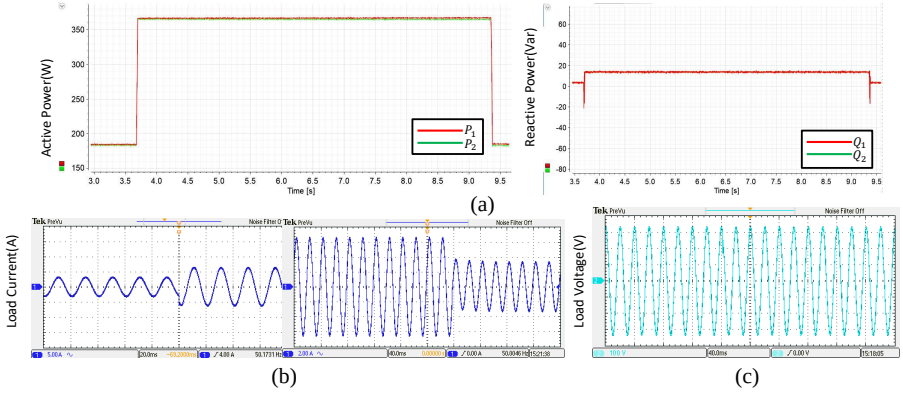

Fig. 3.33. Experimental results under a large load variation. (a) Active and reactive powers. (b)Transient response of load current. (c)Load voltages.

Chapter 4

Hopf Oscillator Controller for Grid-connected Inverters

In this chapter, the power tracking control strategies and grid-synchronization based on Hopf oscillator for grid-connected VSI are presented. In order to complete the microgrid concept, the grid-connected mode controller for three-phase inverters is proposed. The Hopf oscillator provides the grid-synchronization property based on the current feedback. The averaged model of the system will be derived to indicate the $P-\omega$ relationship of the oscillator. The phase-locking region of the forced oscillator will be investigated by the Arnold tongue, and then the stability region is derived by Floquet theory. Due to the Hopf strong nonlinear dynamics regarding amplitude, an extra PI controller is employed for tracking the reactive power using the $Q-V$ droop relationship. Therefore, the Hopf oscillator with current feedback and amplitude regulation can generate the voltage references when synchronized with an input signal. At last, simulation and experimental results verified the effectiveness and validity of the proposed controller compared to the standard droop grid-forming method.

4.1 Grid-connected Inverter Controller and Implementation

As introduced in Chapter 1, a grid-forming inverter should take a role for dispatching active and reactive powers, and also maintain the frequency and voltage to support the grid. Thus, the control objectives can be summarized as dispatching active and reactive powers, grid synchronization and stabilizing the frequency and voltage. The grid-tied three-phase inverter controlled by the proposed method is illustrated in Fig.4.1. The electrical diagram includes a DC source, a three-phase H-bridge inverter, a LCL filter and the grid. The controller block contains two parts: the power tracking loop and the Hopf oscillator. The controller implementation in details is described as follows.

1)**Hopf oscillator**. The oscillator controller acts a role of synchronization with current error and following voltage references generation in $\alpha\beta$ frame. Thus, the amplitude regulation and phasor are integrated into a second order differential equations. In details, as for the phasor, $I^*_{\alpha\beta}$ are regarded as the external periodic input, and the Hopf oscillator controller has the capability to synchronize with the current feedback. As opposed to the islanded mode of self-synchronization, the positive feedback of I^*_α is designed for generating the forced oscillator synchronization characteristics, which is corresponded with the $P-\omega$ of the droop controller. Due to the strong nonlinear performance of the Hopf oscillator, the reactive power tracking should be realized by regulating the voltage reference instead of the phasor, which corresponds to the $Q-V$ of the

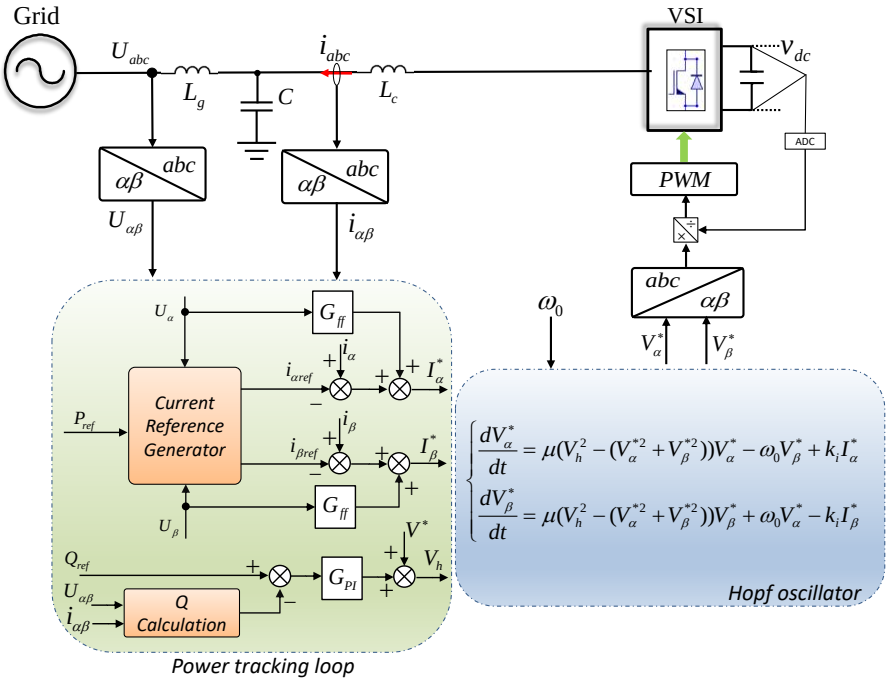

Fig. 4.1. Controller block diagram of the proposed Hopf controller for grid-connected VSI.

droop controller.

2) **Power tracking loop**. In this part, the two-channel controllers corresponding to P and Q power are designed to follow the power reference. The reactive power error is transformed to the amplitude voltage reference error by the PI controller based on droop relationship. The PI coefficients can be optimized using the Ziegler–Nichols method [94].

In order to control the instantaneous active power in grid-tied mode, the current reference [95] in stationary reference frame can be calculated as follows:

$$\begin{aligned} i_{\alpha ref} &= \frac{2}{3}\frac{U_\alpha}{U_\alpha^2+U_\beta^2}P_{ref} + \frac{2}{3}\frac{U_\beta}{U_\alpha^2+U_\beta^2}Q_{ref} \\ i_{\beta ref} &= \frac{2}{3}\frac{U_\beta}{U_\alpha^2+U_\beta^2}P_{ref} - \frac{2}{3}\frac{U_\alpha}{U_\alpha^2+U_\beta^2}Q_{ref} \end{aligned} \tag{4.1}$$

Due to the fact that the reactive power is independently controlled, Q_{ref} can be make it zero in (4.1) to simplify the calculation. Thus, the current error is obtained by the difference between the instantaneous current and the reference. In order to eliminate the undesirable start-up transient, a feed-forward compensator is added to the current loop. The voltage difference between the inverter and the grid is approximately to zero if the current error is zero. The feed-forward block has ability to model the possible small delay in the cancellation of the grid voltage that is a perturbation to the system, and the

transfer function of the compensator is given as:

$$G_{ff} = \frac{1}{k_{PWM}(\tau s+1)} \tag{4.2}$$

where τ is denoted as the time constant, and k_{PWM} is the inverter bridge PWM gain. In the simulations and experiments, $\tau = 8\mu s$ and $k_{PWM} = 1$ are selected. In this way, the active and reactive powers are decoupled and controlled independently. In order to track the small errors in steady state, the bandwidth of the power tracking loop should be wider than the frequency of the system. Next, the amplitude and phase-locking dynamics of the Hopf are analysed in detail for supporting the proposed control.

4.2 Averaged Model and Amplitude Analysis

4.2.1 Averaged Model for Grid-connected Hopf Oscillator

In stationary reference frame, a Hopf type oscillator is able to generate a circular limit cycle, and it generates stable orthogonal periodic signals. It is interesting to analyze the effect of the external periodic force on the self-sustained oscillations. By Defining the external orthogonal periodic force as:

$$I_\alpha = I\sin\omega^* t, I_\beta = I\cos\omega^* t \tag{4.3}$$

where I and ω^* is the current amplitude and the angle frequency of the force signals, respectively.

The dynamics of Hopf oscillator controller with the orthogonal force are expressed as:

$$\begin{cases} \dot{V_\alpha} = \mu(V^{*2} - V_\alpha^2 - V_\beta^2)V_\alpha - \omega_0 V_\beta + kI_\alpha \\ \dot{V_\beta} = \mu(V^{*2} - V_\alpha^2 - V_\beta^2)V_\beta + \omega_0 V_\alpha - kI_\beta \end{cases} \tag{4.4}$$

where $V_{\alpha\beta}$ are the orthogonal states, and ω is the natural frequency of the oscillator.

It is obvious that (4.4) is a nonlinear differential equation in the time scale, whose dynamics are difficult to analize. Thus, the averaged model of (4.4) is derived to achieve the approximate solutions of the amplitude and phase as the system is at the equilibrium point.

Considering the oscillation states $V_\alpha = Vsin(\theta)$, $V_\beta = Vcos(\theta)$ as the equilibrium points, the time derivative of $V_{\alpha\beta}$ are obtained as:

$$\begin{bmatrix} \dot{V_\alpha} \\ \dot{V_\beta} \end{bmatrix} = \begin{bmatrix} \sin\theta & V\cos\theta \\ \cos\theta & -V\sin\theta \end{bmatrix} \begin{bmatrix} \dot{V} \\ \dot{\theta} \end{bmatrix} \tag{4.5}$$

where V and θ is the instantaneous amplitude and phase angle of the oscillating states, respectively.

Substituting (4.5) to (4.4), the amplitude and phase dynamics equations of the forced oscillator are given as follows:

$$\begin{cases} \dot{V} = \mu(V^{*2}V - V^3) - kIsin(\theta - \omega^* t) \\ \dot{\theta} = \omega_0 + \dfrac{kI}{V}cos(\theta - \omega^* t) \end{cases} \tag{4.6}$$

Substituting (3.37) to (4.6), the amplitude and phase averaged dynamics in the corresponding powers can be expressed as:

$$\begin{cases} \dot{\bar{V}} = V^{*2}\mu\bar{V} - \bar{V}^3\mu - \dfrac{2k}{3\bar{V}}\bar{Q} \\ \dot{\bar{\theta}} = \omega_0 + \dfrac{2k}{3\bar{V}^2}\bar{P} \end{cases} \tag{4.7}$$

Considering the power tracking control objectives, the power references P_{ref} and Q_{ref} can be introduced as follows:

$$\begin{cases} \dot{\bar{V}} = \mu(V^{*2}V - V^3) - \dfrac{2k}{3\bar{V}}(\bar{Q} - \bar{Q}_{ref}) \\ \dot{\bar{\theta}} = \omega_0 + \dfrac{2k}{3\bar{V}^2}(\bar{P} - \bar{P}_{ref}) \end{cases} \tag{4.8}$$

The equations shown in (4.8) presents that the dynamics of the voltage amplitude and phase angle change with the difference between the active and reactive powers and their corresponding references, of which characteristics are similar with the $Q-V$ and $P-\omega$ droop curves of the standard droop controller when considering an inductive line impedance. But, it is important to remark that (4.8) is a nonlinear relationship for $Q-V$ and $P-\omega$. For the grid-connected model, the grid-forming inverters should inject the desired power though regulating the voltage amplitude and phase, and synchronize with grid as well. To investigate the control, the amplitude dynamics and phase-locking comprehensive analysis will be discussed as follows.

4.2.2 Amplitude Dynamics Analysis

In order to analyze the amplitude dynamics at the equilibrium point, assume that the oscillator has already being synchronized with the external signals. Then, in this case, it can be assumed that $\sin(\theta - \omega^* t) = 0$ if the steady state frequency synchronizes with the frequency of the external signals. Thus, the amplitude equation can be simplified to:

$$\dot{V} = \mu(V^{*2}V - V^3) \tag{4.9}$$

Due to that (4.9) is a nonlinear first order differential equation, considering the initial condition $V(0) = aV^*$, the solution of (4.9) is:

$$V = \sqrt{-V^{*2}/(\exp(\log(\frac{a^2-1}{a^2}) - 2\mu V^{*2}t) - 1)} \tag{4.10}$$

According to the analysis from 3.2.1, it can be seen that this solution will track the reference signal V^* due to the strong nonlinear error elimination. Firstly, the impact of the initial condition is investigated when V^* and μ are fixed. Figure 4.2(a) shows the relationship between V and the different values of a when $V^* = 1$ and $\mu = 1$. It can be seen that V is able to converge to V^* no matter how the initial conditions varies from 0.1 to 1.5. The dynamic

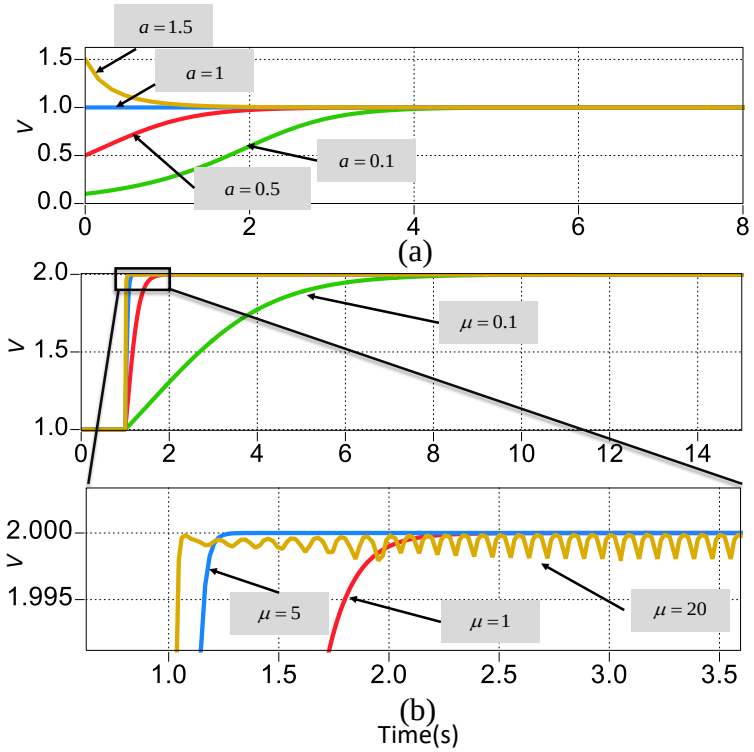

Fig. 4.2. Amplitude tracking performance when: (a) the initial condition varies from 0.1 to 0.5; (b) the damping coefficient varies from 0.1 to 20.

is slower if the difference between V^* and a is larger. In order to achieve the fastest converging dynamics, a is chosen as 1.

Subsequently, μ is the damping coefficient that impacts on the convergence speed and the system's degree of relaxation. In Fig. 4.2(b), the solutions of (4.9) dynamic are presented when μ varies from 0.1 to 20, where the constraints are $V^* = 1 \rightarrow 2$ and $a = 1$. Note that the tracking speed is faster when μ is increasing, which is consistent with the rising time of equation (3.27). However, if μ is large enough extra harmonics components are introduced to the dc component, which means that the oscillator produces the nonessential harmonics due to the larger damping coefficient, e.g. $\mu = 20$. Therefore, regarding the short rising time and signal quality, μ is selected as 5.

In brief, the Hopf oscillator presents a robust and fast amplitude tracking characteristic with the proper initial conditions and damping coefficient, which is helpful to design the voltage regulation loop for the grid-connected controller application.

In equation (4.8), the reactive power tracking item ΔQ cannot regulate the amplitude proportionally due to the strong nonlinear dynamics of the equation term $\mu(V^{*2}V - V^3)$. Therefore, an extra reactive power tracking loop is added to this controller. Note that ΔQ has almost no effect on the amplitude variation when the amplitude reference is chosen as the voltage setting point for the grid-forming inverter.

4.3 Synchronization and Stability Analysis

4.3.1 Phase-locking and Synchronization Region

The limit cycle oscillators can synchronize with a periodic input when the oscillator's intrinsic frequency is close to a frequency component of the input [96–98]. According to this property, this section investigates the phase and frequency synchronization region of the Hopf oscillator.

Consider a periodic input signal $J(t) = J(t+T_J)$, with frequency $\omega^* = 2\pi/T_J$, $J(t)$ and $J(t - T_J/4)$ are orthogonal signals as the input of Hopf oscillator. By introducing the complex variable $z = V_\alpha + iV_\beta$, equation (4.4) can be rewritten as:

$$\dot{z} = (V^{*2} + \omega_0 i)z - z|z|^2 + ki\mathbf{J}, z \in \mathbb{C} \tag{4.11}$$

where $\mathbf{J}$ is the complex function of the periodic inputs $J(t)$ and $J(t-T_J/4)$. Based on the Kuramoto synchronization model[99], the perturbed phase dynamics of 4.6 can be expressed as:

$$\dot{\theta} = \omega_0 + \frac{k}{V} J(\theta - \omega^* t) \tag{4.12}$$

According to (4.12), the phase dynamics with the orthogonal input under different k can be shown in Fig. 4.3. The Hopf oscillator's intrinsic frequency is equal to the input frequency (50Hz), the amplitude reference of the oscillator and input is 10 and 1, respectively. It can be observed that the phase dynamics converge to a fixed point faster when k is increasing, which indicates that the system synchronizes faster for the larger k. Figure 4.4 illustrates a case of synchronization between a oscillator and the periodic input.

By performing the averaged model over fast oscillations(assume V is constant), the dynamics of the phase difference can given in the form:

$$\frac{d\Delta\theta}{dt} = \omega^* - \omega_0 + \frac{kdJ(\Delta\theta)}{Vdt} \tag{4.13}$$

On the other hand, the frequency difference can give us an insight about the phase-locking region. In order to simplify the model, the difference between the phase of the Hopf oscillator and the phase of a periodic input can be defined as:

$$\begin{aligned} \chi &= \theta - \omega^* t \\ \gamma &= \omega^* - \omega_0 \end{aligned} \tag{4.14}$$

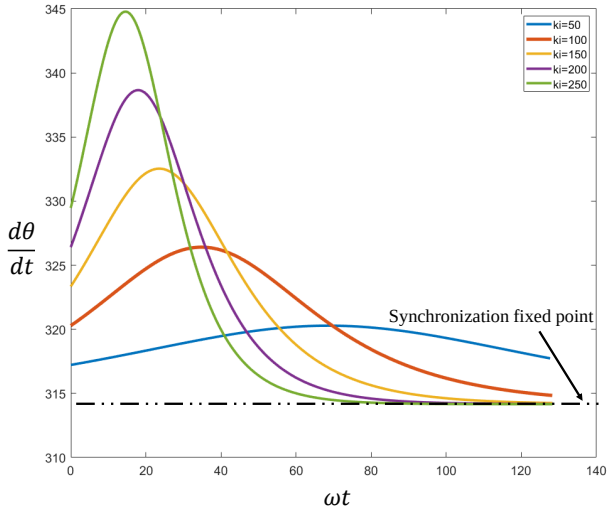

Fig. 4.3. Phase dynamics for different values of k.

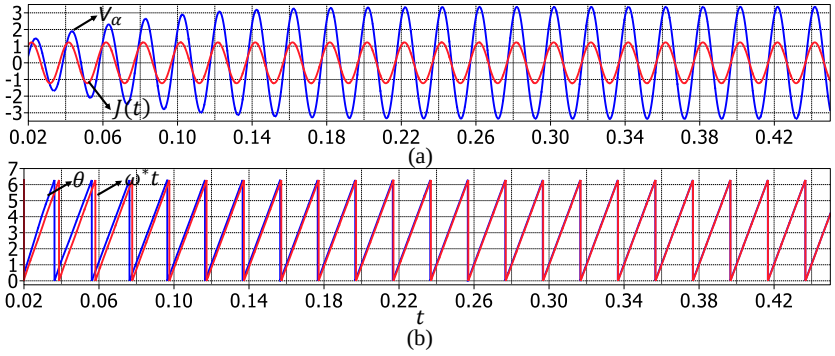

Fig. 4.4. Synchronization relationship between a Hopf oscillator and an external forcing signal for $k = 20$: (a) Signals. (b) Phase.

where χ is a slow phase variable in the rotating frame, and γ is a frequency detuning variable for observing the frequency synchronization. Therefore, equation (4.12) can be rewritten as:

$$\dot{\chi} = -\gamma - \frac{kI}{V}\sin(\chi) \tag{4.15}$$

Equation (4.15) is known as the Adler equation [100, 101]. Therefore, there is a interval for γ in $[0, 2\pi]$ in which: $\frac{k}{V}J_{min} < \gamma < \frac{k}{V}J_{max}$. In this interval, the system remains in the fixed point $\chi = 0$. By Defining the amplitude ratio $\epsilon = \frac{kI}{V}$ and winding number $W = \frac{\omega^*}{\omega_0}$, there exists a synchronization region on the plane of (γ, ϵ) [102, 103].

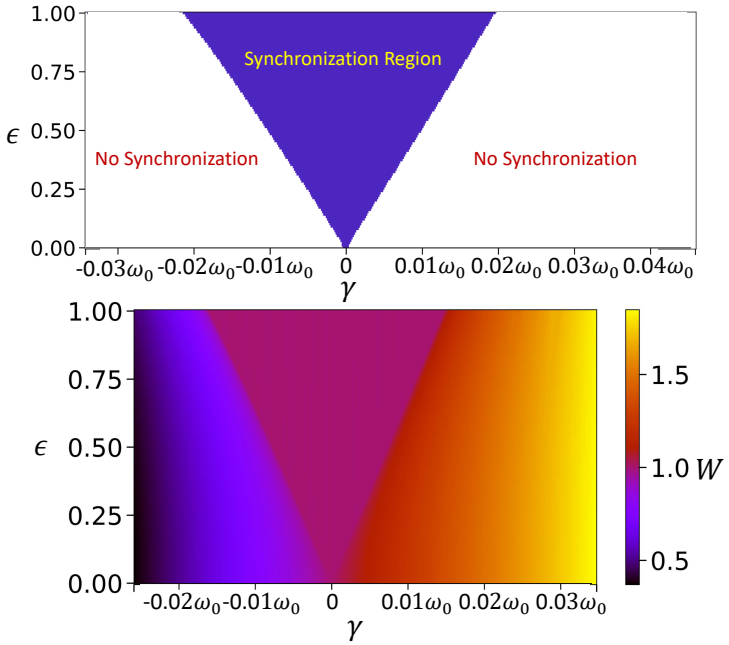

Fig. 4.5. Arnold tongue diagram of the Adler equation (4.13) for $\omega_0 = 100\pi$ and $\epsilon : 0 \to 1$.

In order to find the regions of the phase-locking and frequency synchronization, an effective method called Arnold tongues is employed, which is usually applied in Chaos systems as shown in Fig. 4.5. For a given ϵ, only the values of the amplitude ratio are within the Arnold tongue region where the synchronization occurs. In this tongue, the frequency difference is reduced to zero autonomously and the phases lock naturally between the oscillator and external input. If ϵ is larger, the synchronization region has a wider plateau. Therefore, k can be designed considering the Arnold tongue diagram to achieve the enough wide plateau in the corresponding frequency difference. Beyond this tongue region, the frequency of the oscillator can not synchronize with the external signal's where $W \neq 1$.

In order to find the bifurcation point, the dynamics of no synchronization region should be observed through deriving the beat frequency Ω_χ. Note that Ω_χ indicates the stable and unstable fixed points through the saddle-node bifurcation in a period, which always depends on γ. The beat frequency can be expressed as:

$$\Omega_\chi = 2\pi\left(\int_0^{2\pi} \frac{d\chi}{-\epsilon\sin(\chi) - \gamma}\right)^{-1} \tag{4.16}$$

Therefore, the critical points for Ω_χ can be derived as [60]:

$$\begin{aligned} |\Omega_\chi|_{max} &= \sqrt{\epsilon sin(\chi_{max})(\gamma - \gamma_{max})} \\ |\Omega_\chi|_{min} &= \sqrt{(\gamma - \gamma_{max})} \end{aligned} \tag{4.17}$$

where $\gamma_{max} = \epsilon \sin(\frac{\pi}{2})$, and χ_{max} refers to the maximum value of the phase error. Therefore, the dependence of the beat frequency is obtained which relates to frequency detuning.

4.3.2 Stability Analysis on Periodic Solution

In this part, the stability of the forced oscillator system based on Floquet theory [104, 105] is analyzed. The stability criterion is given by the following theorem:

Theorem II: Consider the fundamental matrix differential equation $\dot{\mathbf{x}} = \mathbf{A}(t)\mathbf{x}$ and the multiplier ρ with characteristic exponent δ so that $\rho = e^{\delta T}$. There exists a periodic solution for $\mathbf{x}(\mathrm{t})=e^{\delta T}\rho(t)$, and the solution is stable if all $|\rho| \leq 1$.

Proof: Define $\mathbf{B}$ as the characteristic multipliers matrix with eigenvalues ρ. Let $\mathbf{x}(\mathrm{t})=\mathbf{X}(\mathrm{t})\mathbf{B}$. There is $\mathbf{x}(t+T) = \rho\mathbf{X}(t)\mathbf{B} = \rho\mathbf{x}(t)$.

Regarding $\rho(t)$ is a periodic multiplier, there is:

$$\rho(t+T) = \mathbf{x}(t+T)e^{-\delta(t+T)} = \frac{\rho}{e^{\delta T}}\mathbf{x}(t)e^{\delta t} = \mathbf{x}(t)e^{\delta t} = \rho(t) \tag{4.18}$$

Therefore, $\rho(t)$ is also a periodic signal with period T. For $\mathbf{x}(t+T) = \rho\mathbf{x}(t)$, each characteristics multipliers can be summarized as:

(1). If $|\rho| < 1$, there is $\mathbf{Re}(\delta) < 0$;

(2). If $|\rho| = 1$, there is $\mathbf{Re} = 0$, and the solution for $\mathbf{x}(t)$ is periodic with period T;

(3). If $|\rho| > 1$, there are $\mathbf{Re}(\delta) > 0$ and $\mathbf{x}(t) \to \infty$. It is can be concluded that the solution of $\mathbf{x}(\mathrm{t})$ is stable if all $|\rho| \leq 1$. Q.E.D.

Subsequently, considering the system of (4.6), its phase dynamics can be expressed as:

$$\begin{cases} \dot{V} = \mu(V^{*2}V - V^3) - k_i I \sin(\chi) \\ \dot{\theta} = \omega + \dfrac{k_i I}{V}\cos(\chi) \end{cases} \tag{4.19}$$

The Jacobian matrix (4.19) is:

$$\mathrm{G}_{Jaco} = \begin{bmatrix} \mu V^{*2} - 3\mu V^2 & -k_i I\cos(\chi) \\ \frac{k_i I}{V^2}\cos(\chi) & -\frac{k_i I}{V}\sin(\chi) \end{bmatrix} \tag{4.20}$$

When calculated around the point $(V, \theta) = (V^*, \omega^* t)$, there is:

$$Tri(\mathrm{G}_{Jaco}) = -2\mu V^{*2} + \frac{kI}{V^*} \tag{4.21}$$

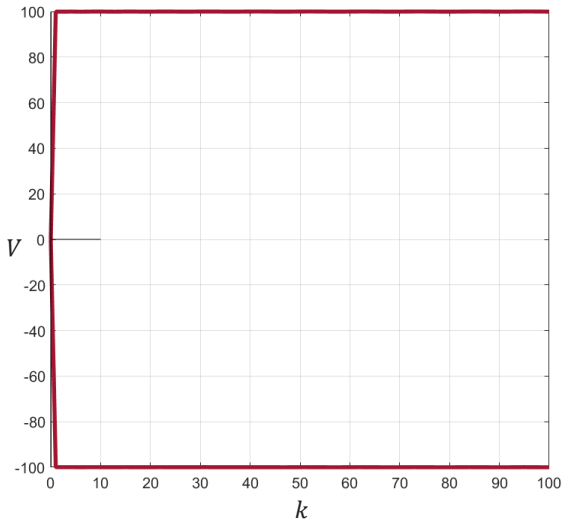

Fig. 4.6. Bifurcations of the systems with varying k. The initial state is (0,0).

Thus, the characteristics multiplier for (4.19) is:

$$\rho = exp(4\pi\mu V^{*2} - \frac{2\pi kI}{V^*}) \tag{4.22}$$

According to *Theorem II*, the entire solutions for (4.19) are stable if it satisfies $|\rho| \leq 1$, so that

$$(-2\mu V^{*2} + \frac{2kI}{V}) \geq 0 \Rightarrow 2\mu V^{*2} \geq kI \tag{4.23}$$

To validate the stable region, $I = 10$, $V^* = 100$, $\mu = 1$ and $\omega^* = 100\pi$ are selected. The bifurcation of the Hopf oscillator with k changing is plotted in Fig. 4.6. Note that the solutions for the amplitude have a constant value $V^* = 100$ when k changes. In an electrical system, it is clear that cubic voltage reference is much larger than the value of k multiplied by the feedback current amplitude, which indicates a large design range for k. As mentioned before, k also affects the dynamic's speed. Therefore, the converging speed and stability constrains are considered in designing parameter k.

4.4 Simulation and Experiment Results

4.4.1 Simulation Results

In this section, the above mentioned controller is validated by the simulation in time-domain using MATLAB/PLECS. In order to highlight the novelty of the proposed method, a standard droop grid-forming controller has been chosen to be compared with. The simulated system consists of the two three-phase

Table 4.1: System parameters used in simulation and experiment

Parameter	Value	Unit
DC-link voltage	450	V
Filter inductance	1.8	mH
Filter capacitance	25	μF
Oscillator initial state	325, 0	V,V
Current gain k	50	A/A
Line resistance	0.12	Ω
Line inductance	4	mH
Line voltage(RMS)	230	V
Grid frequency	50	Hz
Frequency reference	50	Hz
Switching frequency	10	kHz
Voltage amplitude reference	325	V
PI K_p and K_i	0.001, 0.05	

VSIs, LCL filter, local loads and a grid network. The electrical system and controller parameters are listed in Table 4.1. Various simulation tests have been performed, which include: active power tracking performance, reactive power tracking performance, grid synchronization, switching to islanded mode, comparison with droop gird-forming controller under a step change perturbation.

1) **Tracking performance of** P. Considering the individual VSI connected to a stiff grid, Fig. 4.7 exhibits the transient results for tracking an active power reference step from $P_{ref} = 0 \rightarrow 2000 \rightarrow 3000 \rightarrow 2000W$ at time 3.0s, 4.0s and 5.0s, respectively. As shown in Fig. 4.7(a), VSI is able to accurately track the active power setpoint (blue curve) with a fast transient. As the analysis mentioned, the dynamics speed mainly depends on the current gain k and the line inductance L_g. From Fig. 4.7(b), after a small transient (less than 150Var) the reactive power is able to be fixed at zero when $Q_{ref} = 0$. Due to the $P - \omega$ characteristics of the Hopf oscillator, the frequency is regulated by the active power tracking loop, and the transient error is less than 0.1Hz which is in the permissible range $\pm 1\%$ of nominal. Meanwhile, the slight variation occurs for the output voltage RMS due to the active power stepping as illustrated in Fig. 4.7(b)(c). Note that the RMS difference is less than 0.5V which results in stable output voltage for voltage grid support.

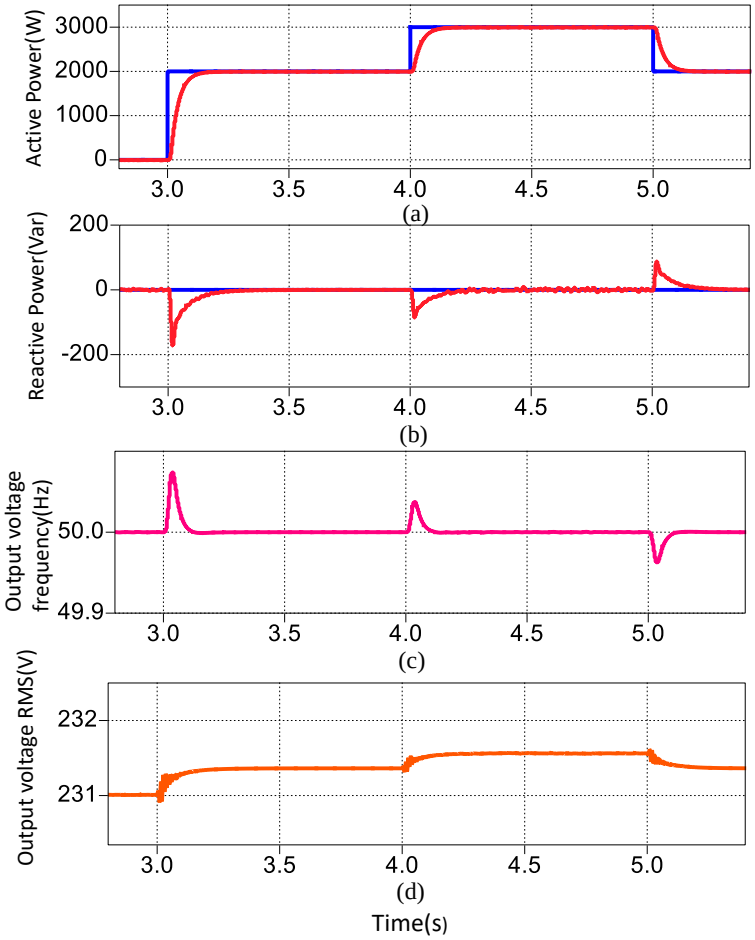

Fig. 4.7. Simulation results for active tracking performance. (a) Active power. (b) Reactive power. (c) Frequency of the output voltage. (d) RMS of the output voltage.

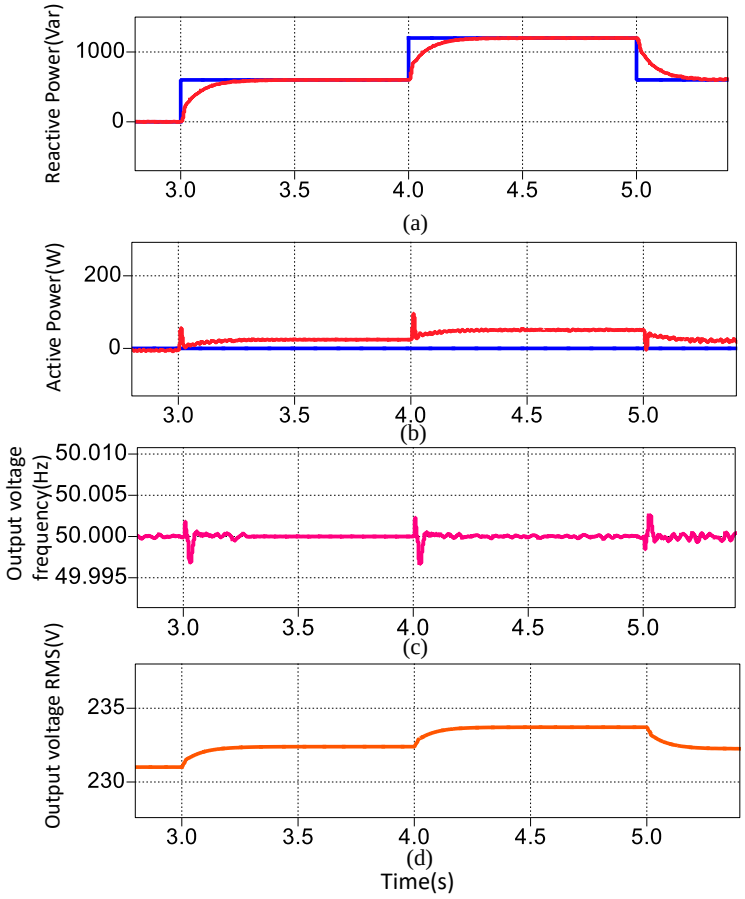

Fig. 4.8. Simulation results for reactive tracking performance. (a) Reactive power. (b) Active power. (c) Frequency of the output voltage. (d) RMS of the output voltage.

2) **The tracking performance of** Q. The dispatching reactive power results are illustrated in Fig. 4.8 with $Q_{ref} = 0 \rightarrow 600 \rightarrow 1200 \rightarrow 600Var$ at time 3.0s, 4.0s and 5.0s, respectively. Note that the reactive power is tracked precisely with a smooth transient. As for the active power in Fig. 4.8(b), the instantaneous value is small instead of zero (less than 50W) owing to the changes on the amplitude regulation. In Fig. 4.8(c), the frequency of the output voltage is stable during the set-point stepping. Note that the reactive power settling time is slower than that occurred for the active power, with measured times of 0.38s and 0.2s, respectively. This effect results from the adding of an additional PI controller that is necessary to regulate the reactive power. However, the forced Hopf oscillator presents an overall faster dynamic response due to the regulation through k.

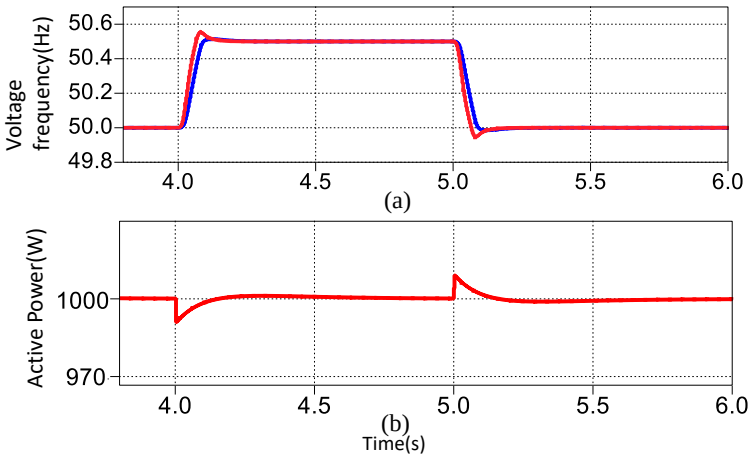

Fig. 4.9. Simulation results for grid frequency tracking performance. (a) Grid and inverter output frequency. (b) Active power.

3) **The tracking performance of grid frequency**. To validate the grid synchronization property, when the grid frequency (blue curve) ramps up from 50Hz to 50.5Hz and ramps down to 50Hz, the frequency tracking performance of the proposed method is demonstrated by the results shown at Fig. 4.9(a). It can be seen that the VSI can synchronize with the grid frequency rapidly, while a small overshoot/undershoot occurs within a error that has been measured as 0.05Hz. Figure 4.9(b) shows the robust performance for the active power where the transient is smoothly converged to its reference value, which means that the active power has no been affected by the grid frequency variation. It should be remarked that the proposed method doesn't rely on using of a PLL and it can achieve a the grid-synchronization with precise and fast tracking performance.

4) **Power sharing performance under off-grid**. Figure 4.10 consists in the average power and frequency when system supplies a local load (3kW) at 2s and then a second VSI is connected at 3s. It can be seen that the Hopf oscillator has no overshoot when switching to off-grid mode. In order to avoid a large phase difference, a pre-synchronization stage is added into the VSI#2 as explained in Section 3.3.2. The active and reactive powers are shared properly with fast transient responses as shown in Fig. 4.10(a)(b). In Fig. 4.10(c), the VSI#1 frequency reduces to 49.87Hz because it is supplying a large load power and the frequency returns to nominal after connecting VSI#2, where now the active power reference is 1500W for VSI#1 and VSI#2.

5) **Comparison with a droop grid-forming controller**. The droop controller is widely used in parallel inverters for both grid-connected and islanded mode. For the inductive line impedance, the $P-\omega$ and $Q-V$ droop characteristics for the grid-forming VSI are employed. In simulation, the droop coefficient of $P-\omega$ is 0.0001 and the reactive power is regulated by means of a PI controller with $k_p = 0.073$ and $k_i = 0.52$.

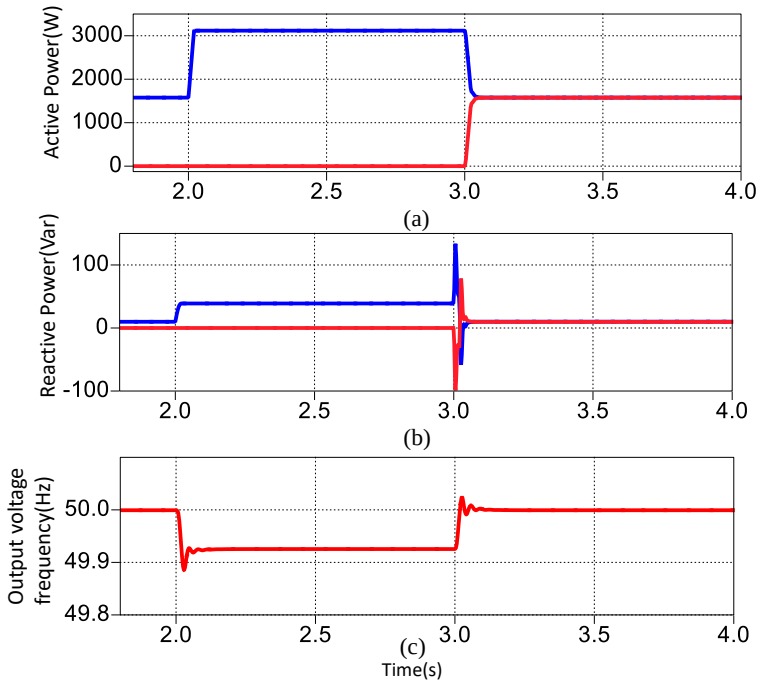

Fig. 4.10. Simulation results for off-grid operation. (a) Active power. (b) Reactive power. (c) Frequency of the output voltage.

Figure 4.11 illustrates the simulation results comparison between for both methods. When the active power reference steps from 0.5 p.u. to 0.6 p.u. as shown in Fig.4.11(a), the transient response of the Hopf oscillator is faster than the standard droop, whose transient time has been measured as 1s and 1.8s, respectively. Note that there is a 2.3% overshoot in the active power transient of the droop controller, while there is no overshoot for the Hopf oscillator. For the both methods, the frequency of the output voltage recovery to the nominal with the frequency error less than 0.02Hz as presented in Fig. 4.11(b). During the active power stepping, the variation of the voltage RMS for the Hopf oscillator is lower than droop's as show in Fig. 4.11(c). Regarding the power quality of the output current, a lower THD with 0.05% is measured in comparison with 0.11% THD achieved for the droop method. Therefore, compared with the standard droop grid-forming controller, the proposed method exhibits a faster and more robust performance under the active power stepping case.

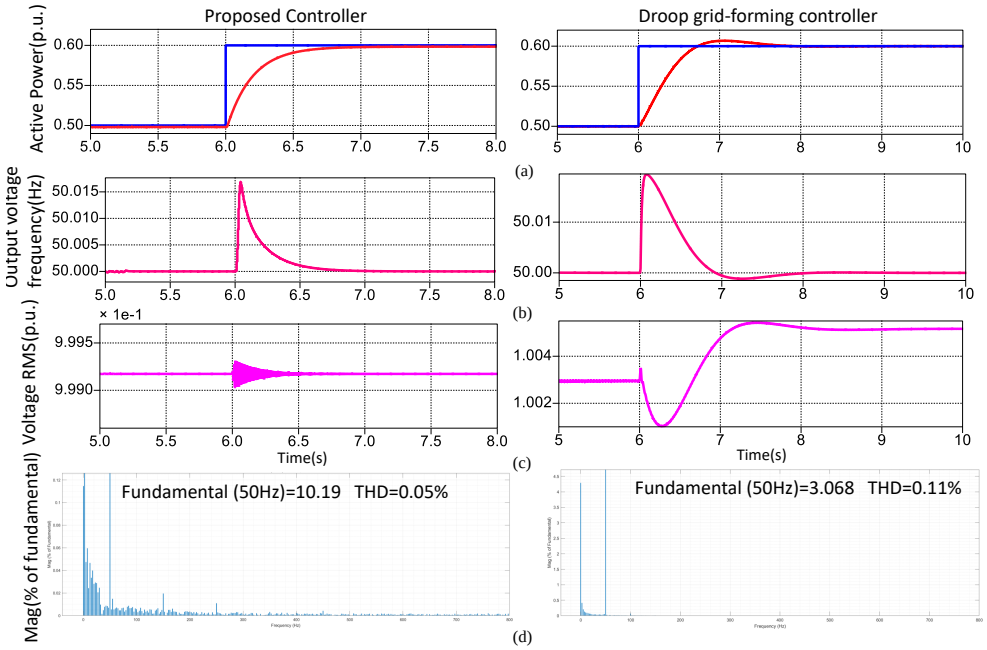

Fig. 4.11. Simulation results comparison for the active power tracking between the proposed controller and droop grid-forming controller. (a) Active power. (b) Frequency of the output voltage. (c) RMS of the output voltage. (d) THD of the output current.

4.4.2 Experiment Results

In this section, the performance and effectiveness of the proposed method will be evaluated considering a three-phase VSI facing an stiff grid network. A programmable AC voltage source Chroma 61704 is employed to emulate the grid and a 2.2-kVA Danfoss inverter connected to the grid with an LCL filter. The experimental and control parameters are also shown in Table 4.1.

Figure 4.12 and Figure 4.13 illustrate the 1kW active and 1kVar reactive power tracking performance for proposed method. Figure 4.12(b) and Figure 4.13(b) show the transient response for the grid voltage and output current of phase A. It can be seen that the output current exhibits a fast tracking ability according to the power references. For this test the power factor was 1 with $P_{ref} = 1$kW and $Q_{ref} = 0$kVar and the power factor is 0 with $P_{ref} = 0$kW and $Q_{ref} = 1$kVar.

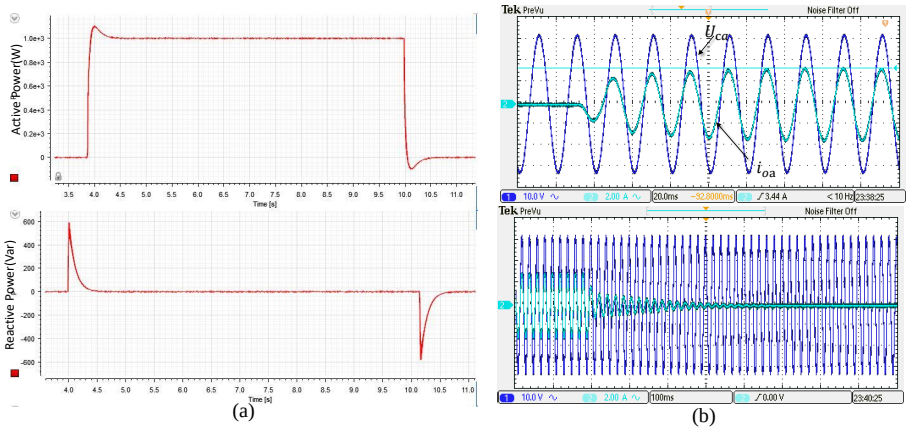

Fig. 4.12. Power tracking performance during an active power step change. (a) Instantaneous active and reactive power. (b) Output current and grid voltage of A phase.

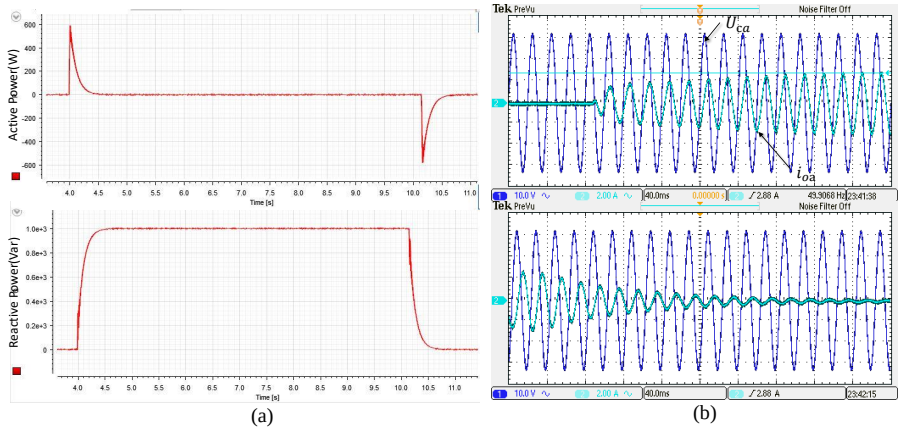

Fig. 4.13. Power tracking performance under a reactive power step change. (a) Instantaneous active and reactive power. (b) Phase A output current and grid voltage.

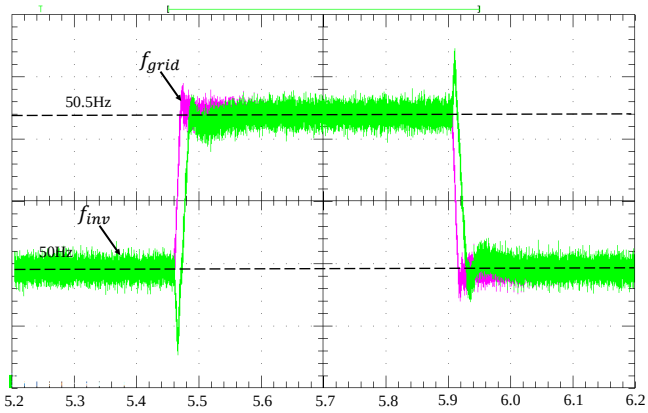

Fig. 4.14. Frequency tracking performance from 50Hz to 50.5Hz.

As shown in Fig. 4.12(a) and Fig. 4.13(a), there are an apparent overshoot or undershoot for the 0kW/kVar power reference, because the oscillation of the oscillator has an amplitude/frequency evolution when amplitude/frequency step change happens. The frequency tracking performance is illustrated in Fig. 4.14. The frequency of the oscillator-controlled inverter has adaptive frequency ability with the grid, when the grid frequency suddenly changes from 50Hz to 50.5Hz. In conclusion, the proposed method satisfies the requirements of the grid-forming operation.

Chapter 5

Conclusion and Future Works

5.1 Concluding Remarks

This thesis has shown a combined SOGI power calculation method for droop-controlled inverters when sharing the nonlinear loads, and Hopf oscillator controller for grid-forming inverters in which the dynamic performance has been assessed. Moreover, the Hopf driven inverters have been designed to operate in islanded and grid-connected mode. The main objectives of this work consist first of the development of a fast power calculation algorithm and second a novel primary control for a microgrid system, in order to achieve fast dynamic response and better synchronization performance. This proposed control strategies have been developed in the stationary reference frame.

Firstly, a fast and precise power calculation technique has been proposed for the parallel operation of three-phase inverters with nonlinear loads, based on a combined SOGI filter approach. It can be seen that the proposed technique showed to work faster than the traditional droop controller thanks to the SOGI filters' accurate synchronization and signal extraction capability. In comparison to the LPF-based droop technique, the root locus and phase step response, using the developed small signal model of the two parallel inverters presented a faster dynamic response. To demonstrate the effectiveness of the proposed control technique, the cut-off frequency has been designed for achieving the same ripple as the LPF method. For achieving that, the damping factor have been tuned for the combined SOGI method. To verify this method, a series of simulations have been performed considering linear and nonlinear loads. In simulation validation, the transient time of combined SOGI method shows to be decreased about 95% maintaining the same power ripple. The results show that the proposed method is efficient and achieves a faster dynamic response under both linear and nonlinear loads.

And then, a Hopf oscillator controller has been proposed with the aiming of achieving a fast synchronization and accurate current sharing that can be applied to single-phase and three-phase inverters. The frequency and amplitude voltage references for the inverter are provided by the Hopf oscillator dynamic equations, which result in a robust nonlinear droop behaviour for the system operation without requiring communications. In comparison to the approach used a Van der Pol oscillator, the Hopf oscillator offers a higher robustness load sharing between inverters, less harmonic distortion, and faster dynamic response with the stable limit cycle. Additionally, the Lyapunov technique demonstrates the system global asymptotic synchronization. In the Hopf oscillator, a re-synchronization item has been introduced into the control equations to overcome the overshoot that the system exhibits at the connection of the inverters. In

islanded mode, the nonlinear droop characteristics of $P-V$ and $Q-\omega$ relationship have been derived by the averaged model. The stability analysis based on the small signal model has been investigated for achieving the connection between the parameters and system performance. To verify the proposed technique, a number of comparative simulations and experiments have been conducted. The observed findings demonstrate effective current sharing and rapid and precise synchronization, particularly fewer voltage and frequency variations during high power load switching.

For the grid-connected mode operation, the $P-\omega$ and $Q-V$ relationship have been derived for an inductive line impedance characteristic by using an averaged model. the synchronization of oscillator with periodic force has been also discussed in theory. To observe the phase dynamics of the proposed controller, the phase-locking region has been measured by the Arnold tongue method. Next, the stability region has been derived through Floquet theory, which presents that the current gain has a large appropriate stability region. Then, a power tracking method using an external synchronization of forced oscillator and PI controller has been introduced. Simulation and experimental findings have been verified that there is a precise tracking of P and Q, fast grid-synchronization and robustness. The measured harmonics distortion for the Hopf method is of 0.05%, which compared by 0.11% achieved by the droop method, which shows a better power quality for the Hopf oscillator.

With the obvious merits of fast dynamics, adaptive synchronization and a simple design, the proposed control strategies could be applied in microgrid system with different operation modes.

5.2 Future Works

As discussed in thesis limitation, the main research fields in future work can be summarized as:

- As for the synchronization of a carrier wave, the network model of the circulating current and the carrier synchronization of coupled Hopf oscillator will be investigated. The band pass filter for voltage references should be designed for filtering out the components apart from switching frequency.

- In view of secondary control layer of droop methods, proof why the coupled oscillator does need a frequency adjustment through deriving the coupled oscillators frequency dynamics.

- Summarize the oscillators-controlled control strategies with different types of oscillators, and derive the common equations of the nonlinear droop. Thus, it can be analyzed in terms of characteristics compared with conventional droop method.

- Improve the oscillator-controlled method adding capability to face some power quality issues such as the unbalanced grid, harmonics and weak grid characteristics. Re-design the controller to provide both synchronization and stability with regarding the use of LCL filters and the line impedance. Analyze the robustness and stability of the improved controller, and design a strong adaptability controller for grid-connected inverters.
- Extend the proposed methods to Microgrid clusters, and establish the inter-area oscillations mathematical model of a cluster system. Investigate the oscillations dampening method to enhance the transient stability in a cluster. Develop voltage angle differences in control of the coupled oscillators in linear time-invariant networks for islanded and grid-connected modes.

Bibliography

[1] T. Ackermann, G. Andersson, and L. Söder. "Distributed generation: a definition". In: *Electric power systems research* 57.3 (2001), pp. 195–204.

[2] R. H. Lasseter et al. "Microgrids and distributed generation". In: *Journal of Energy Engineering* 133.3 (2007), pp. 144–149.

[3] M. H. Bollen and F. Hassan. *Integration of distributed generation in the power system*. Vol. 80. John wiley & sons, 2011.

[4] R. S. Rao et al. "Power loss minimization in distribution system using network reconfiguration in the presence of distributed generation". In: *IEEE transactions on power systems* 28.1 (2012), pp. 317–325.

[5] R. Zamora and A. K. Srivastava. "Controls for microgrids with storage: Review, challenges, and research needs". In: *Renewable and Sustainable Energy Reviews* 14.7 (2010), pp. 2009–2018.

[6] D. E. Olivares et al. "Trends in microgrid control". In: *IEEE Transactions on smart grid* 5.4 (2014), pp. 1905–1919.

[7] W. Su and J. Wang. "Energy management systems in microgrid operations". In: *The Electricity Journal* 25.8 (2012), pp. 45–60.

[8] W. I. Bower et al. *The advanced microgrid. integration and interoperability*. Tech. rep. Sandia National Lab.(SNL-NM), Albuquerque, NM (United States), 2014.

[9] A. Hirsch, Y. Parag, and J. Guerrero. "Microgrids: A review of technologies, key drivers, and outstanding issues". In: *Renewable and sustainable Energy reviews* 90 (2018), pp. 402–411.

[10] B. Li and R. Roche. "Optimal scheduling of multiple multi-energy supply microgrids considering future prediction impacts based on model predictive control". In: *Energy* 197 (2020), p. 117180.

[11] J. M. Guerrero et al. "Hierarchical control of droop-controlled AC and DC microgrids—A general approach toward standardization". In: *IEEE Transactions on industrial electronics* 58.1 (2010), pp. 158–172.

[12] J. M. Guerrero et al. "Advanced control architectures for intelligent microgrids—Part I: Decentralized and hierarchical control". In: *IEEE Transactions on Industrial Electronics* 60.4 (2012), pp. 1254–1262.

[13] J. C. Vasquez et al. "Hierarchical control of intelligent microgrids". In: *IEEE Industrial Electronics Magazine* 4.4 (2010), pp. 23–29.

[14] T. L. Vandoorn et al. "Microgrids: Hierarchical control and an overview of the control and reserve management strategies". In: *IEEE industrial electronics magazine* 7.4 (2013), pp. 42–55.

[15] Y. A.-R. I. Mohamed and A. A. Radwan. “Hierarchical control system for robust microgrid operation and seamless mode transfer in active distribution systems”. In: *IEEE Transactions on Smart Grid* 2.2 (2011), pp. 352–362.

[16] D. A. Torrey and A. M. Al-Zamel. “Single-phase active power filters for multiple nonlinear loads”. In: *IEEE Transactions on Power electronics* 10.3 (1995), pp. 263–272.

[17] A. Chandra et al. “An improved control algorithm of shunt active filter for voltage regulation, harmonic elimination, power-factor correction, and balancing of nonlinear loads”. In: *IEEE transactions on Power electronics* 15.3 (2000), pp. 495–507.

[18] E. A. A. Coelho, P. C. Cortizo, and P. F. D. Garcia. “Small-signal stability for parallel-connected inverters in stand-alone AC supply systems”. In: *IEEE Transactions on Industry Applications* 38.2 (2002), pp. 533–542.

[19] S. Anttila et al. “Grid Forming Inverters: A Review of the State of the Art of Key Elements for Microgrid Operation”. In: *Energies* 15.15 (2022), p. 5517.

[20] A. Tuckey and S. Round. “Grid-Forming Inverters for Grid-Connected Microgrids: Developing “good citizens” to ensure the continued flow of stable, reliable power”. In: *IEEE Electrification Magazine* 10.1 (2022), pp. 39–51.

[21] D. B. Rathnayake et al. “Grid forming inverter modeling, control, and applications”. In: *IEEE Access* (2021).

[22] M. A. Schwemmer and T. J. Lewis. “The theory of weakly coupled oscillators”. In: *Phase response curves in neuroscience*. Springer, 2012, pp. 3–31.

[23] R. E. Mirollo and S. H. Strogatz. “Synchronization of pulse-coupled biological oscillators”. In: *SIAM Journal on Applied Mathematics* 50.6 (1990), pp. 1645–1662.

[24] I. Szatmári and L. O. Chua. “Awakening dynamics via passive coupling and synchronization mechanism in oscillatory cellular neural/nonlinear networks”. In: *International Journal of Circuit Theory and Applications* 36.5-6 (2008), pp. 525–553.

[25] K. Chen and D. Wang. “A dynamically coupled neural oscillator network for image segmentation”. In: *Neural Networks* 15.3 (2002), pp. 423–439.

[26] C. Pinto and M. Golubitsky. “Central pattern generators for bipedal locomotion”. In: *Journal of mathematical biology* 53.3 (2006), pp. 474–489.

[27] K. De Brabandere et al. “A voltage and frequency droop control method for parallel inverters”. In: *IEEE Transactions on power electronics* 22.4 (2007), pp. 1107–1115.

[28] E. Barklund et al. “Energy management in autonomous microgrid using stability-constrained droop control of inverters”. In: *IEEE Transactions on Power Electronics* 23.5 (2008), pp. 2346–2352.

[29] J. Liu, Y. Miura, and T. Ise. “Comparison of dynamic characteristics between virtual synchronous generator and droop control in inverter-based distributed generators”. In: *IEEE Transactions on Power Electronics* 31.5 (2015), pp. 3600–3611.

[30] H. Bevrani and S. Shokoohi. “An intelligent droop control for simultaneous voltage and frequency regulation in islanded microgrids”. In: *IEEE transactions on smart grid* 4.3 (2013), pp. 1505–1513.

[31] Y. Li and Y. W. Li. “Decoupled power control for an inverter based low voltage microgrid in autonomous operation”. In: *2009 IEEE 6th International Power Electronics and Motion Control Conference*. IEEE. 2009, pp. 2490–2496.

[32] T. Wu et al. “A unified virtual power decoupling method for droop-controlled parallel inverters in microgrids”. In: *IEEE Transactions on Power Electronics* 31.8 (2015), pp. 5587–5603.

[33] M. Ashabani et al. “Multivariable droop control of synchronous current converters in weak grids/microgrids with decoupled dq-axes currents”. In: *IEEE Transactions on Smart Grid* 6.4 (2015), pp. 1610–1620.

[34] J. He et al. “An islanding microgrid power sharing approach using enhanced virtual impedance control scheme”. In: *IEEE Transactions on Power Electronics* 28.11 (2013), pp. 5272–5282.

[35] J. Kim et al. “Mode adaptive droop control with virtual output impedances for an inverter-based flexible AC microgrid”. In: *IEEE Transactions on power electronics* 26.3 (2010), pp. 689–701.

[36] A. Micallef et al. “Reactive power sharing and voltage harmonic distortion compensation of droop controlled single phase islanded microgrids”. In: *IEEE Transactions on Smart Grid* 5.3 (2014), pp. 1149–1158.

[37] H. Han et al. “An improved droop control strategy for reactive power sharing in islanded microgrid”. In: *IEEE Transactions on Power Electronics* 30.6 (2014), pp. 3133–3141.

[38] C.-T. Lee, C.-C. Chu, and P.-T. Cheng. “A new droop control method for the autonomous operation of distributed energy resource interface converters”. In: *IEEE Transactions on Power Electronics* 28.4 (2012), pp. 1980–1993.

[39] J. C. Vasquez et al. “Voltage support provided by a droop-controlled multifunctional inverter”. In: *IEEE Transactions on Industrial Electronics* 56.11 (2009), pp. 4510–4519.

[40] W. Wang et al. “Analysis of microgrid inverter droop controller with virtual output impedance under non-linear load condition”. In: *IET Power Electronics* 7.6 (2014), pp. 1547–1556.

[41] R. An et al. “Analysis and design of cutoff frequency for power calculation low-pass filters in droop control”. In: *2017 IEEE 3rd International Future Energy Electronics Conference and ECCE Asia (IFEEC 2017-ECCE Asia)*. IEEE. 2017, pp. 1596–1600.

[42] H. R. Baghaee, M. Mirsalim, and G. B. Gharehpetian. “Power calculation using RBF neural networks to improve power sharing of hierarchical control scheme in multi-DER microgrids”. In: *IEEE Journal of Emerging and Selected Topics in Power Electronics* 4.4 (2016), pp. 1217–1225.

[43] J. Matas et al. “A family of gradient descent grid frequency estimators for the SOGI filter”. In: *IEEE Transactions on Power Electronics* 33.7 (2017), pp. 5796–5810.

[44] J. Matas et al. “A new THD measurement method with small computational burden using a SOGI-FLL grid monitoring system”. In: *IEEE Transactions on Power Electronics* 35.6 (2019), pp. 5797–5811.

[45] J. El Mariachet et al. “HIL-assessed fast and accurate single-phase power calculation algorithm for voltage source inverters supplying to high total demand distortion nonlinear loads”. In: *Electronics* 9.10 (2020), p. 1643.

[46] J. El Mariachet et al. “A power calculation algorithm for single-phase droop-operated-inverters considering linear and nonlinear loads HIL-assessed”. In: *Electronics* 8.11 (2019), p. 1366.

[47] Y. Guan et al. “A new way of controlling parallel-connected inverters by using synchronous-reference-frame virtual impedance loop—Part I: Control principle”. In: *IEEE Transactions on Power Electronics* 31.6 (2015), pp. 4576–4593.

[48] M. Guan et al. “Synchronous generator emulation control strategy for voltage source converter (VSC) stations”. In: *IEEE Transactions on Power Systems* 30.6 (2015), pp. 3093–3101.

[49] J. Liu et al. “Enhanced virtual synchronous generator control for parallel inverters in microgrids”. In: *IEEE Transactions on Smart Grid* 8.5 (2016), pp. 2268–2277.

[50] H. Wu et al. “Small-signal modeling and parameters design for virtual synchronous generators”. In: *IEEE Transactions on Industrial Electronics* 63.7 (2016), pp. 4292–4303.

[51] T. Jouini, C. Arghir, and F. Dörfler. “Grid-friendly matching of synchronous machines by tapping into the DC storage”. In: *IFAC-PapersOnLine* 49.22 (2016), pp. 192–197.

[52] C. Arghir, T. Jouini, and F. Dörfler. “Grid-forming control for power converters based on matching of synchronous machines”. In: *Automatica* 95 (2018), pp. 273–282.

[53] B. B. Johnson et al. “Synchronization of parallel single-phase inverters with virtual oscillator control”. In: *IEEE Transactions on Power Electronics* 29.11 (2013), pp. 6124–6138.

[54] B. B. Johnson et al. “Synchronization of nonlinear oscillators in an LTI electrical power network”. In: *IEEE Transactions on Circuits and Systems I: Regular Papers* 61.3 (2014), pp. 834–844.

[55] B. B. Johnson et al. “Oscillator-based inverter control for islanded three-phase microgrids”. In: *IEEE Journal of Photovoltaics* 4.1 (2013), pp. 387–395.

[56] B. B. Johnson et al. “Synthesizing virtual oscillators to control islanded inverters”. In: *IEEE Transactions on Power Electronics* 31.8 (2015), pp. 6002–6015.

[57] M. Sinha et al. “Nonlinear supersets to droop control”. In: *2015 IEEE 16th Workshop on Control and Modeling for Power Electronics (COMPEL)*. IEEE. 2015, pp. 1–6.

[58] M. Sinha et al. “Uncovering droop control laws embedded within the nonlinear dynamics of van der pol oscillators”. In: *IEEE Transactions on Control of Network Systems* 4.2 (2015), pp. 347–358.

[59] B. Johnson et al. “Comparison of virtual oscillator and droop control”. In: *2017 IEEE 18th Workshop on Control and Modeling for Power Electronics (COMPEL)*. IEEE. 2017, pp. 1–6.

[60] A. Pikovsky, M. Rosenblum, and J. Kurths. *Synchronization: a universal concept in nonlinear science*. 2002.

[61] R. Grimshaw. *Nonlinear Ordinary Differential Equations: Applied Mathematics and Engineering Science Texts*. Routledge, 2017.

[62] D. Panayotounakos, N. Panayotounakou, and A. Vakakis. “On the lack of analytic solutions of the Van der Pol oscillator”. In: *ZAMM-Journal of Applied Mathematics and Mechanics/Zeitschrift für Angewandte Mathematik und Mechanik: Applied Mathematics and Mechanics* 83.9 (2003), pp. 611–615.

[63] H. Liu, W. Jia, and L. Bi. “Hopf oscillator based adaptive locomotion control for a bionic quadruped robot”. In: *2017 IEEE International Conference on Mechatronics and Automation (ICMA)*. IEEE. 2017, pp. 949–954.

[64] E. Oviedo, N. Vazquez, and R. Femat. “Synchronization technique of grid-connected power converters based on a limit cycle oscillator”. In: *IEEE Transactions on Industrial Electronics* 65.1 (2017), pp. 709–717.

[65] M. Lu et al. “A grid-compatible virtual oscillator controller: Analysis and design”. In: *2019 IEEE Energy Conversion Congress and Exposition (ECCE)*. IEEE. 2019, pp. 2643–2649.

[66] M. Lu. “Virtual Oscillator Grid-forming Inverters: State of the Art, Modeling, and Stability”. In: *IEEE Transactions on Power Electronics* (2022).

[67] V. Kaura and V. Blasko. “Operation of a phase locked loop system under distorted utility conditions”. In: *IEEE Transactions on Industry applications* 33.1 (1997), pp. 58–63.

[68] G.-C. Hsieh and J. C. Hung. “Phase-locked loop techniques. A survey”. In: *IEEE Transactions on industrial electronics* 43.6 (1996), pp. 609–615.

[69] J. Lee and B. Kim. “A low-noise fast-lock phase-locked loop with adaptive bandwidth control”. In: *IEEE Journal of solid-state circuits* 35.8 (2000), pp. 1137–1145.

[70] J. C. Vasquez et al. “Adaptive droop control applied to voltage-source inverters operating in grid-connected and islanded modes”. In: *IEEE transactions on industrial electronics* 56.10 (2009), pp. 4088–4096.

[71] S. Vazquez et al. “Predictive optimal switching sequence direct power control for grid-connected power converters”. In: *IEEE Transactions on Industrial Electronics* 62.4 (2014), pp. 2010–2020.

[72] D. Santos-Martin, J. L. Rodriguez-Amenedo, and S. Arnalte. “Direct power control applied to doubly fed induction generator under unbalanced grid voltage conditions”. In: *IEEE Transactions on Power Electronics* 23.5 (2008), pp. 2328–2336.

[73] M. Li et al. “A Fast Power Calculation Algorithm for Three-Phase Droop-Controlled-Inverters Using Combined SOGI Filters and Considering Nonlinear Loads”. In: *Energies* 15.19 (2022), p. 7360.

[74] M. Li et al. “Inverter parallelization for an islanded microgrid using the Hopf oscillator controller approach with self-synchronization capabilities”. In: *IEEE Transactions on Industrial Electronics* 68.11 (2020), pp. 10879–10889.

[75] M. Li et al. “Advanced synchronization control for inverters parallel operation in microgrids using coupled Hopf oscillators”. In: *CPSS Transactions on Power Electronics and Applications* 5.3 (2020), pp. 224–234.

[76] J. Buchli. “Engineering limit cycle systems: Adaptive frequency oscillators and applications to adaptive locomotion control of compliant robots”. PhD thesis. Verlag nicht ermittelbar, 2007.

[77] B. D. Hassard et al. *Theory and applications of Hopf bifurcation*. Vol. 41. CUP Archive, 1981.

[78] J. E. Marsden and M. McCracken. *The Hopf bifurcation and its applications*. Vol. 19. Springer Science & Business Media, 2012.

[79] M. G. Crandall and P. H. Rabinowitz. “The Hopf bifurcation theorem in infinite dimensions”. In: *Archive for Rational Mechanics and Analysis* 67.1 (1977), pp. 53–72.

[80] S. Chen and Y. Cheung. “An Elliptic Lindstedt–Poincaré Method for Certain Strongly Non-Linear Oscillators”. In: *Nonlinear Dynamics* 12.3 (1997), pp. 199–213.

[81] M. Vidyasagar. *Nonlinear systems analysis*. SIAM, 2002.

[82] J. Van Hemmen and W. Wreszinski. "Lyapunov function for the Kuramoto model of nonlinearly coupled oscillators". In: *Journal of Statistical Physics* 72.1 (1993), pp. 145–166.

[83] Z. Liu, Y.-C. Lai, and M. A. Matıas. "Universal scaling of Lyapunov exponents in coupled chaotic oscillators". In: *Physical Review E* 67.4 (2003), p. 045203.

[84] L. G. de la Fraga and E. Tlelo-Cuautle. "Optimizing the maximum Lyapunov exponent and phase space portraits in multi-scroll chaotic oscillators". In: *Nonlinear Dynamics* 76.2 (2014), pp. 1503–1515.

[85] G. Chen, J. Zhou, and S. Celikovsky. "On LaSalle's invariance principle and its application to robust synchronization of general vector Lie/spl acute/nard equations". In: *IEEE transactions on automatic control* 50.6 (2005), pp. 869–874.

[86] J. Drbohlav and F.-F. Jin. "Interdecadal variability in a zonally averaged ocean model: An adjustment oscillator". In: *Journal of physical oceanography* 28.6 (1998), pp. 1252–1270.

[87] N. S. Namachchivaya and J. H. Park. "Stochastic dynamics of impact oscillators". In: (2005).

[88] M. N. Marwali, J.-W. Jung, and A. Keyhani. "Stability analysis of load sharing control for distributed generation systems". In: *IEEE Transactions on Energy Conversion* 22.3 (2007), pp. 737–745.

[89] J. M. Guerrero et al. "Decentralized control for parallel operation of distributed generation inverters using resistive output impedance". In: *IEEE Transactions on industrial electronics* 54.2 (2007), pp. 994–1004.

[90] X. Guo et al. "Dynamic phasors-based modeling and stability analysis of droop-controlled inverters for microgrid applications". In: *IEEE Transactions on Smart Grid* 5.6 (2014), pp. 2980–2987.

[91] H. Liang et al. "Stability enhancement of decentralized inverter control through wireless communications in microgrids". In: *IEEE Transactions on Smart Grid* 4.1 (2013), pp. 321–331.

[92] L. Meng et al. "Distributed voltage unbalance compensation in islanded microgrids by using a dynamic consensus algorithm". In: *IEEE Transactions on Power Electronics* 31.1 (2015), pp. 827–838.

[93] Y. Gui et al. "Passivity-based coordinated control for islanded AC microgrid". In: *Applied energy* 229 (2018), pp. 551–561.

[94] K. J. Åström and T. Hägglund. "Revisiting the Ziegler–Nichols step response method for PID control". In: *Journal of process control* 14.6 (2004), pp. 635–650.

[95] A. Yazdani and R. Iravani. *Voltage-sourced converters in power systems: modeling, control, and applications*. John Wiley & Sons, 2010.

[96] R. Perez and L. Glass. “Bistability, period doubling bifurcations and chaos in a periodically forced oscillator”. In: *Physics Letters A* 90.9 (1982), pp. 441–443.

[97] T. Harada et al. “Optimal waveform for the entrainment of a weakly forced oscillator”. In: *Physical review letters* 105.8 (2010), p. 088301.

[98] T. Nakayama and K. Yakubo. “The forced oscillator method: eigenvalue analysis and computing linear response functions”. In: *Physics reports* 349.3 (2001), pp. 239–299.

[99] J. A. Acebrón et al. “The Kuramoto model: A simple paradigm for synchronization phenomena”. In: *Reviews of modern physics* 77.1 (2005), p. 137.

[100] B. Razavi. “A study of injection locking and pulling in oscillators”. In: *IEEE journal of solid-state circuits* 39.9 (2004), pp. 1415–1424.

[101] P. Bhansali and J. Roychowdhury. “Gen-Adler: The generalized Adler’s equation for injection locking analysis in oscillators”. In: *2009 Asia and South Pacific Design Automation Conference*. IEEE. 2009, pp. 522–527.

[102] S. Nakata et al. “Arnold tongue of electrochemical nonlinear oscillators”. In: *The Journal of Physical Chemistry A* 113.25 (2009), pp. 6876–6879.

[103] T. E. Lee, C.-K. Chan, and S. Wang. “Entanglement tongue and quantum synchronization of disordered oscillators”. In: *Physical Review E* 89.2 (2014), p. 022913.

[104] P. A. Kuchment. *Floquet theory for partial differential equations*. Vol. 60. Springer Science & Business Media, 1993.

[105] F. Casas, J. Oteo, and J. Ros. “Floquet theory: exponential perturbative treatment”. In: *Journal of Physics A: Mathematical and General* 34.16 (2001), p. 3379.